SANDIA REPORT
SAND2009-6241
Unlimited Release
Printed September 2009

Modeling surfaces in the context of pulsed-power: work functions, electron emission and dynamic response

Thomas R. Mattsson, Kyle Cochrane, Sophie Chantrenne, and Sergey Faleev

Prepared by
Sandia National Laboratories
Albuquerque, New Mexico 87185 and Livermore, California 94550

Sandia is a multiprogram laboratory operated by Sandia Corporation,
a Lockheed Martin Company, for the United States Department of Energy's
National Nuclear Security Administration under Contract DE-AC04-94AL85000.

Approved for public release; further dissemination unlimited.

Sandia National Laboratories

Issued by Sandia National Laboratories, operated for the United States Department of Energy by Sandia Corporation.

NOTICE: This report was prepared as an account of work sponsored by an agency of the United States Government. Neither the United States Government, nor any agency thereof, nor any of their employees, nor any of their contractors, subcontractors, or their employees, make any warranty, express or implied, or assume any legal liability or responsibility for the accuracy, completeness, or usefulness of any information, apparatus, product, or process disclosed, or represent that its use would not infringe privately owned rights. Reference herein to any specific commercial product, process, or service by trade name, trademark, manufacturer, or otherwise, does not necessarily constitute or imply its endorsement, recommendation, or favoring by the United States Government, any agency thereof, or any of their contractors or subcontractors. The views and opinions expressed herein do not necessarily state or reflect those of the United States Government, any agency thereof, or any of their contractors.

Printed in the United States of America. This report has been reproduced directly from the best available copy.

Available to DOE and DOE contractors from
U.S. Department of Energy
Office of Scientific and Technical Information
P.O. Box 62
Oak Ridge, TN 37831

Telephone: (865) 576-8401
Facsimile: (865) 576-5728
E-Mail: reports@adonis.osti.gov
Online ordering: http://www.osti.gov/bridge

Available to the public from
U.S. Department of Commerce
National Technical Information Service
5285 Port Royal Rd.
Springfield, VA 22161

Telephone: (800) 553-6847
Facsimile: (703) 605-6900
E-Mail: orders@ntis.fedworld.gov
Online order: http://www.ntis.gov/help/ordermethods.asp?loc=7-4-0#online

SAND2009-6241
Unlimited Release
Printed September 2009

Modeling surfaces in the context of pulsed-power: work functions, electron emission and dynamic response

Thomas R. Mattsson
Pulsed Power Sciences Center
Sandia National Laboratories
P.O. Box 5800, Albuquerque, New Mexico, 87185

Kyle Cochrane
Ktech Corporation, Albuquerque, New Mexico

Sophie Chantrenne
SAIC, Albuquerque, New Mexico

Sergey Faleev
SNAMI inc, Alabama

Abstract

The ability to quickly understand and deal with issues on ZR, or to virtually design a future ZX accelerator, requires a physics-based capability to simulate all key pulsed power components. Highly important for gas switches and transmission lines are surface phenomena: thermionic emission, photoemission, field emission, and ion-surface dynamics. These are complex processes even at normal conditions, when coupled to the dynamic environment in pulsed power components, the current state of the art of understanding is not at the level of science based predictive modeling. Modeling efforts at the macroscopic level (finite element based hydrodynamic simulations) require detailed information of these processes to yield more reliable results. This is the final report of an LDRD project in the science of extreme environments investment area; the project was focused on describing the physics of surfaces of materials of interest in pulsed-power components. We have calculated the temperature dependence of work functions for metals from first principles using density functional theory (DFT) as well as investigated the effect of initial oxidation and alloying. By using the GW method, we have gone beyond DFT to calculate work functions for Al. The GW work required base-lining the GW results for different systems, since GW lacks a description of total energy. Lastly, we investigated the more macroscopic physics of how a surface and bulk material responds to a very high current under a short time, representative for current loads in pulsed-power components, with emphasis on materials modeling. These simulations were made using two hydrodynamic codes, ALEGRA and MACH2, in order to focus on the materials models themselves.

TABLE OF CONTENTS

Modeling surfaces in the context of pulsed-power: work functions, electron emission and dynamic response 3

Table of contents 4

Figures 5

Tables 7

Introduction 9
- **Overview of the project and the report** 9
- **Gas switches and surface emission** 10
- **High current conductors** 10

Methods and results 11
- **Density Functional Theory** 12
  - The AM05 functional 12
- **Kubo-Greenwood response** 13
- **Calculation of work function from first principles** 13
  - DFT calculation of work function for metals and surface oxides 14
  - Work function of Alumina 16
  - Work function of Copper 19
- **Inelastic electron-electron scattering from first principles: Cu.** 20
- **Beyond DFT, applying GW theory to a wide-gap insulator – alumina** 21
  - Introduction and description of method 21
  - Electronic structure of Al_2O_3 22
  - Dielectric function of Al_2O_3 25
- **Work function of Al using self-consistent GW** 28
  - Introduction and description of method 28
  - Work function of Al (001) surface 29
- **Simulations of very high currents in pulsed-power conditions** 31
  - Material models 31
  - Simulation Configuration 31
  - Simulation results and analysis 32
  - Copper coated tungsten electrode 40
- **Conclusions and recommendations** 41
- **Manufacturing of a graded-density conductor** 42

Summary of results 44

Acknowledgments 44

References 45

Appendix A – AM05 for solids, JOURNAL OF CHEMICAL PHYSICS 2008. 47

Appendix B – comment on PBEsol, PHYSICAL REVIEW LETTERS 2008. 48

Appendix C –work functions from QSGW, to be SUBMITTED TO PHYSICAL REVIEW B. 49

FIGURES

Figure 1. Schematic of a gas switch, understanding the emission of electrons from surfaces is important in order to model the break-down dynamics of the switch. 10
Figure 2: Z accelerator and load region, the region exposed to the strongest currents..... 11
Figure 3. Mean absolute errors for lattice constant (left) and bulk modulus (right) for 20 solids with seven exchange-correlation functionals: PBE0 and HSE06 [20] and AM05, LDA, PBE, RPBE, and BLYP [19]. 13
Figure 4. Side view of a 6 layer super cell of W(100), snapshot at 400 K. 14
Figure 5. Electron potential energy across the full periodic super cell, including slab and vacuum regions (points), Fermi-energy (red), and interval over where the vacuum potential was sampled (blue): 0 K (left), and 700 L (right). At 700 K, the potential was averaged over 20 configurations extracted from a long QMD simulation. 14
Figure 6. Left: work function for W(001) as a function of temperature: the present study (blue), experimental data [22] (red line), and DFT results at 0 K [23] (purple). Right: work function at 0 K when substituting surface W atoms with O (red) and Cu (orange), surface alloying affects the work function significantly. The theoretical results were presented at an APS meeting [24]..... 15
Figure 7. Four cells used to investigate the effect of oxidation on the work function of Al. Bare Al (111) (Φ=4.2eV); Al(111) with chemisorbed O (Φ=4.97 eV); Al(111) interfaced with κ-Alumina (Φ=5.06 eV); Al(111) with chemisorbed O interfaced with κ-Alumina (Φ=6.92 eV). The formation of a chemisorbed layer in combination with the oxide significantly enhances the work function. 15
Figure 10. VASP calculated cold curve for *K*-phase Alumina. 17
Figure 11. Over lapping surfaces (energy[*x,y*]) where each surface is a different *z*, the plot simultaneously illustrates minimization in the three lattice parameters of K-alumina..... 18
Figure 12. Simulation space of the slab geometry, with the periodicity of the simulation shown. The second block of atoms is not actually used. These atoms are shown in their perfect *K*-phase alumina position before being equilibrated at a finite temperature. 18
Figure 15 Electron energy loss function ELF(ω) for Cu from QMD (left). Q-dependent electron energy loss function ELF(q,ω) (right) derived by solving for ω in the dispersion relation..... 20
Figure 16. Points of scattering for 20 initial electrons at 12 eV in the region close to the surface. Vacuum is Z<0 and the color coding is with respect to distance to the surface (blue close to surface, red deep in the bulk) (right). Electron emission probability for different photon energies; 500 electron trajectories were initiated and followed for each initial energy. 20
Figure 17. DOS of α-Al2O3: QSGW (green solid line) and LDA (blue dashed line). XPS data of 1976 experiment, Ref. [41] (red dotted line), and data of 1990 experiment, Ref. [34] (black dotted line), are shown normalized to height of LVB and UVB peaks. Zero on the figure is valence band maximum (VBM)..... 22
Figure 18. Band structure of α-Al2O3.: GW (green solid line) and LDA (blue dashed line). Experimental band gap 9.13 eV [34] at zero temperature is shown at Γ point..... 23
Figure 19. Horizontal axis - experimental band gaps, vertical axis – calculated band gaps. Left panel: LDA (red squares) and one-shot GW (circles) gaps; right panel: QSGW gaps. Results for α-Al2O3 are shown by red arrow in both panels. 24

Figure 20. LDA and QSGW dielectric constants in comparison with experiment. Results for α-Al2O3 are shown by read arrow. 24
Figure 21. Imaginary part of dielectric function calculated by LDA approach: this work (blue dashed line), Holm et al. [37] (green solid line). Experimental data [47] is shown by red dotted line..... 26
Figure 22. Imaginary (left panel) and real (right panel) parts of dielectric function of α-Al2O3 calculated by LDA (blue dashed line), and QSGW (green solid line) approaches. Experimental data [47] shown by red line..... 26
Figure 23. Imaginary part of MgO dielectric function. Left panel - result of present calculations: LDA (blue dashed line) and QSGW (green solid line); right panel – result of quasiparticle calculations [48] without (green solid line) and with (blue solid line) inclusion of electron-hole interactions. On both panels red dotted line shows experimental result [49]. 27
Figure 24. Graphical Graphical representation of Table I. LDA (empty circles) and QSGW (filled circles) results for work function of Al (001). All points obtained with nk=6 except green points (nk=8). Experimental WF 4.41 eV [18] is shows by blue line. 29
Figure 25: Simulation setup of a cylindrical conductor..... 32
Figure 26: Typical Current waveform. 33
Figure 27: Density along the radius for different materials and at different times during the risetime (10 MA peak current density). 34
Figure 28: Temperature as a function of radial position for different materials at different times during the current risetime (10 MA peak current density). 35
Figure 29: Current density as a function of radial position for different materials at different times during the current risetime (10 MA peak current density)..... 36
Figure 30: Comparison of the Current density profile calculated with two different EOS models: a) the FT-DFT calculations (ref. 6,7) , b) the standard Sesame model (ref. 15)..... 37
Figure 31. Current in the load and inductance of aluminum and tungsten cylinders. 37
Figure 32: Fraction of current loss at peak current in different materials for different peak current densities. Al has a small loss for low current density, but an increasing loss at higher currents. Tungsten and stainless steel are improvements at higher currents albeit displaying larger loss at low currents..... 38
Figure 33: Temperature along the radius for Cu, for different peak currents and at different times during the current risetime. 39
Figure 35: Copper coated tungsten initial density profile..... 40
Figure 34. Graded density sample, copper to aluminum showing the texture of the graded density region. 40
Figure 36. Illustration of the plasma-spray process: a powder is fed into the plasma torch and accelerated while heated to close or beyond the melting point. By changing the powder make-up, the composition of the surface coating can be tailored precisely, for example be graded. 42
Figure 37. Rotation assembly for cold spray coating of Tantalum bar stock. The rotation rate is adjustable from 0 to 100 RPM. 42
Figure 38: Properties of tungsten and copper coated tungsten for a 5 MA/cm peak current density. 43

TABLES

Table 1. Lattice values at the calculated minimum energy..... 16
Table 2. Work function energy for *K*-phase alumina. 17
Table 3 Reference energy by pseudo-potential for FCC copper at 0 Kelvin..... 19
Table 4. Work function energy for copper for each pseudo-potential at 100 and 700 Kelvin. 19
Table 5. Work function of Al (001), calculated in QSGW and LDA approaches as function of nk, NAl, and NV. Single processor CPU time per one GW iteration is also shown. 29
Table 6. VASP results of LDA-CA and GGA-PBE calculations of Al (001) work function..... 30

Nomenclature

AM05	Armiento-Mattsson 2005 density functional
DFT	Density Functional Theory
DOS	Density of States
GGA	Generalized Gradient Approximation
GW	Many body theory named after its two key propagation operators G and W
KG	Kubo-Greenwood
LDA	Local Density Approximation
LDRD	Laboratory Directed Research and Development program
PBE	Perdew, Burke, Ernzerhof, a type of GGA.
SNL	Sandia National Laboratories

INTRODUCTION

The ability to quickly understand and deal with issues on Z, or to virtually design of a future ZX accelerator requires a physics-based capability to simulate all key pulsed power components. The ability to simulate these components at a physics level is critically dependent on our ability to acquire key material properties, especially surface phenomena, to use in EM codes. The project broadened the scope of our first-principles modeling to include surface phenomena relevant to surface induced electrical breakdown. For example, thermionic emission, photoemission, field emission, and ion-surface dynamics are all highly important for pulsed power applications like gas switches and transmission lines. We have developed a capability to calculate work functions for different materials, including the effect of oxidation and surface alloying. Knowledge of the work function is of direct importance for secondary emission of electrons from multiple sources. We began by studying metals (aluminum, copper, tungsten) and the effect of oxidation and impurities using Density Functional Theory (DFT), followed by work employing a many-body theory approach. During the last year, focus shifted to dynamic material effects of high currents in pulsed-power components.

Overview of the project and the report

A part of the project was devoted to fundamental work in Density Functional Theory (DFT); we benchmarked a new exchange-correlation functional (AM05) for its overall performance for solid state systems (Appendix A) as well as compared it to a more recently developed functional (Appendix B). A brief review of the theory is included in the report.

First-principles simulations of work function was a central part of the project from start to finish, initial results were presented at the 2008 March meeting of the American Physical Society in New Orleans, LA and a manuscript planned for submission to Physical Review B is included as Appendix C.

We utilized the capacity developed to perform first-principles based calculations of the work function of materials and coupled it to modeling of secondary emission. We thus went beyond the present modeling of secondary emission by using a combination of results from QMD: work function, real- and imaginary parts of the dielectric constant, conductivity, and optical transition matrix elements. The approach is briefly described in the report.

During the last half of the project, the refurbishment of the Z accelerator was finalized and new issues arose regarding general questions of how high current conductors behave. In particular, how would even higher currents in future generations of accelerators affect the performance of conductors? We therefore revised the project plan to include rad-MHD simulations of surface dynamic response to high-current conditions as well as design and manufacturing of a graded density conductor.

The report begins with brief background motivating the work, which is followed by an extensive methods section describing the technical approaches used in the project integrated with the results. A brief results section summarizing the main findings follows the methods section.

Gas switches and surface emission

Simulations of HEDP systems are routinely done using complex radiation-hydrodynamics codes like ALEGRA, HYDRA, LASNEX, or MACH. Common to all simulations is an extensive use of material models, the quality of which directly determines the fidelity of the simulations. Developing high-quality models is thus very important in order to perform macroscopic simulations with confidence.

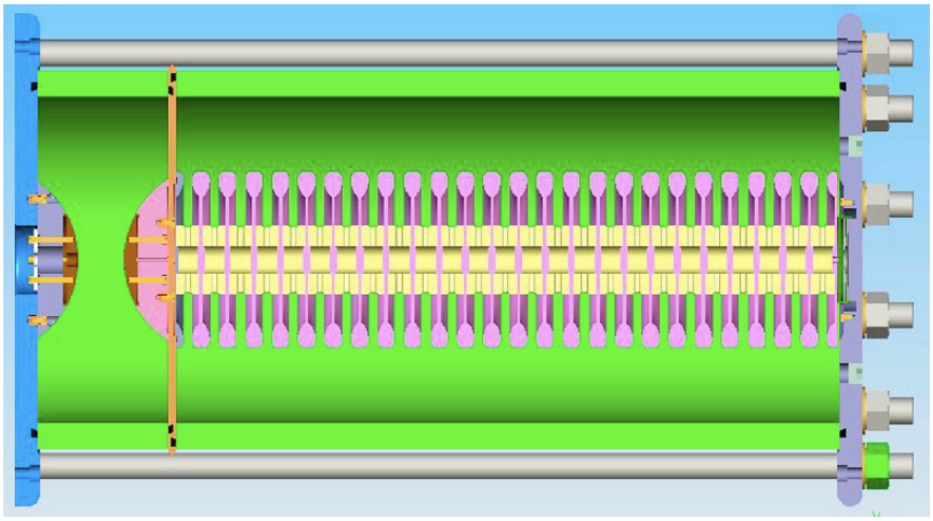

Figure 1. Schematic of a gas switch, understanding the emission of electrons from surfaces is important in order to model the break-down dynamics of the switch.

To improve the materials models we have applied a range of methods: DFT based molecular dynamics (MD) simulations, we calculated work functions using both DFT and the many-body theory GW. Finally, surface emission from a Cu surface was estimated by performing Monte Carlo (MC) transport simulations.

High current conductors

The development of high power pulse technology is the consequence of growing demands for high power sources of energy in various research areas, such as inertial confinement fusion, high pressure shock compression of solids or weapons physics, including electromagnetic launchers, microwave and X-ray generators, nuclear effects simulators. In a pulse power machine, energy is collected from some primary source energy at low power level, low power density, and stored in some temporary storage. Then, the energy is rapidly released from storage and converted into a power of pulsed form. After further compression of the pulsed power, the power is finally delivered to the load at high power level and high power density. As larger pulse power drivers are being built in order to reach higher peak currents, conditions at the load such as temperature and density reach a limit where significant losses occur and material cannot sustain the extreme conditions. Presently, the Z accelerator [1] at Sandia National Laboratories generates currents as high as 26 MA and linear current densities exceeding 5 MA/cm. In these conditions, the energy radiated by a wire load could reach 2.7 MJ.

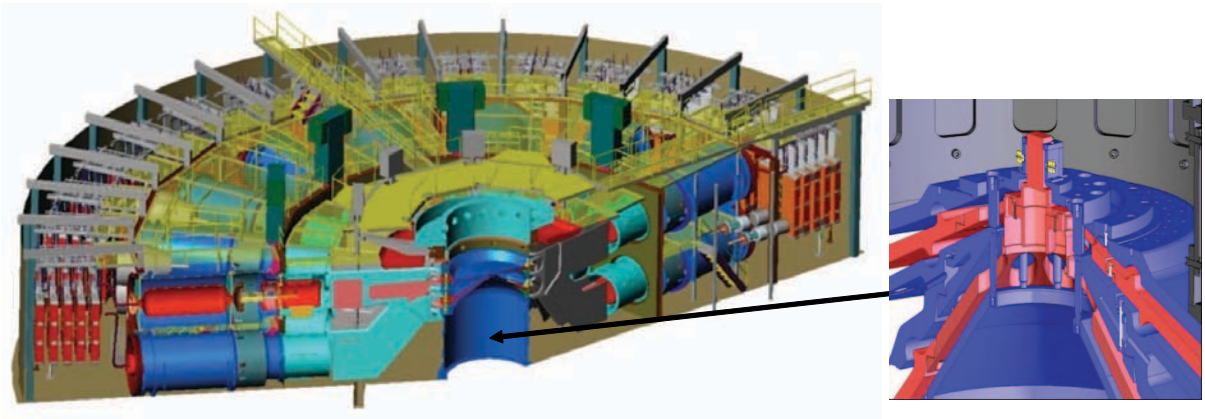

Figure 2: Z accelerator and load region, the region exposed to the strongest currents.

Conductors carrying very high currents show losses of an electromagnetic and shock compression nature [2,3]. The electromagnetic losses are caused by the magnetic flux diffusion in the conductor, as well as by joule heating of the skin layer. Also, the magnetic pressure pushes on the surface of the conductor, generating a shock that propagates into the conductor. The material between the surface and the shock front is compressed, heated and accelerated by the shock, which requires some energy from the system and results in a loss. A detailed description of the loss mechanism can be found in references 2 and 3.

Understanding the properties of materials is essential to improving performance and to reach higher current densities in smaller loads. In the present work, we performed radiative magneto-hydrodynamic (RMHD) simulations to investigate several materials when subjected to high current densities. The present study differs from previous similar work [4] in that new and improved equation of states and conductivity models are employed in this study. During the last year questions arose regarding general behavior of extremely high and rapid currents in conductor. For example, how would even higher currents affect the performance of transmission lines. We revised the project plan to include rad-MHD simulations of surface dynamic response to high-current conditions as well as a prototype construction of a conductor with graded density, build from a Ta core to a pure Cu surface. The design allows for high surface conductivity on a high-density conductor, the heavy core allowing for increased shock impedance, thus delaying increase in electrical impedance due to kinetic motion of the conductors. The design was simulated in hydrodynamics simulations of graded density conductors.

METHODS AND RESULTS

In order for materials simulations to be predictive, we must employ a method that works across materials, is not based on fitting to experiments from first principles. It needs to include dissociation of molecules, bound electrons as well as free electrons. The theory must be a quantum theory while at the same time efficient enough to allow for long-time simulations of the dynamics. Density Functional Theory (DFT) has for a long time been successfully been applied

to problems in condensed matter physics and chemistry, much more recently DFT has been used in the HEDP regime.

Density Functional Theory

DFT is a formally exact reformulation of the Schrödinger equation, the original papers of Hohenberg and Kohn [5] and Kohn and Sham [6] are well worth reading, and so is Kohn's Nobel Lecture [7]. Later reviews are also available, including a recent review by one of the authors [8] on the more practical aspects of performing high-quality calculations. The main approximation of the theory is the choice of the so-called exchange-correlation functional. The first approximation, the local density approximation (LDA) was put forward already in the pioneering work [6]. LDA works excellently for many systems, in particular metals, but rather poorly for molecules. Functionals taking the gradient of the density in to account were developed later by many: Becke, Lee, Yang, and Parr (BLYP) [9], PW91 [10], PBE [11], and revised PBE (RPBE) [12]. Gradient corrected functionals improved significantly upon LDA for molecular systems. However, only PW91 and PBE are widely used for solid-state problems. For along time, PW91 and PBE were considered equivalent, and are often referred as the generalized gradient approximation (GGA). Only recently was it discovered that PW91 and PBE can, and do, yield different results [13].

As computers became faster and codes more efficient, it became possible to apply DFT also to solid-state problems that require several tens of atoms in the super-cell: surfaces, defects, interfaces, and alloys. As this development accelerated, there were only two xc-functionals available: LDA or GGA (PW91/PBE). This changed in 2005.

The AM05 functional

Development of an exchange-correlation functional based on a surface model system was discussed by Kohn and Mattsson [14]. The approach was later formalized and generalized in the subsystem functional scheme [15] and implemented in the AM05 functional [16]. AM05 involves two model systems: the uniform electron gas is used in regions that are locally bulk-like and a surface functional (derived from the Airy gas [14] and jellium surfaces) for regions that are locally surface-like. By including two different exact reference systems, AM05 constitutes a systematic improvement over LDA. In the first paper, it was demonstrated that AM05 gives lattice constants and bulk moduli to high accuracy for Al (simple metal), Pt (transition metal) and Si (semi conductor) [16]. AM05 was implemented in VASP 5.1 during 2007 and the initial benchmarking on solids with the VASP code [17-18] was made as a part of the LDRD project. We compared results for 20 solids (Al, Ag, Pd, Rh, Cu, GaAs, GaP, Na, NaF, NaCl, MgO, SiC, Si, C, GaN, BN, BP, Li, LiF, and LiCl), it was confirmed that AM05 yields lattice constants that on average are significantly better than LDA, PBE, RPBE, and BLYP [19], mean absolute errors are shown in Figure 3.

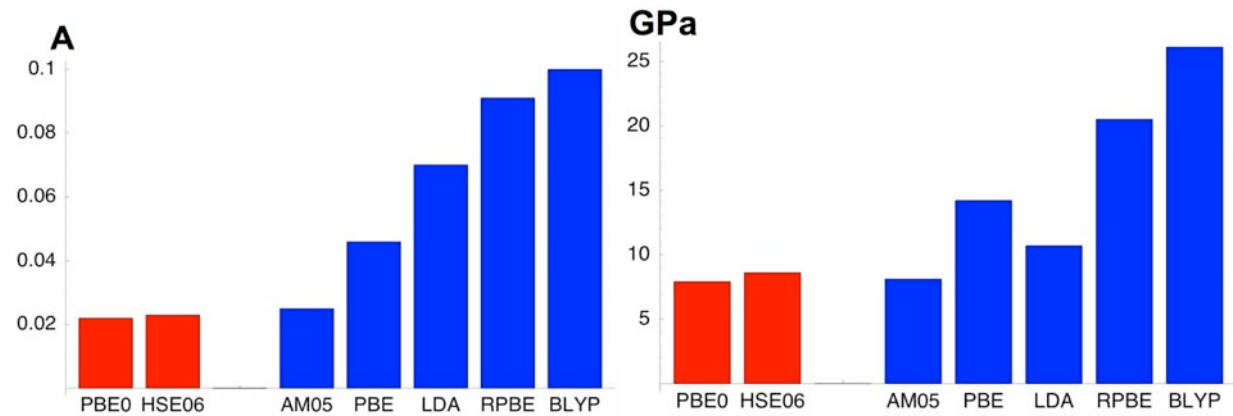

Figure 3. Mean absolute errors for lattice constant (left) and bulk modulus (right) for 20 solids with seven exchange-correlation functionals: PBE0 and HSE06 [20] and AM05, LDA, PBE, RPBE, and BLYP [19].

We conclude that new functional partly employed in this work, AM05, performs on average as well as computationally significantly more expensive hybrids. After successfully benchmarking the functional on a variety of solids followed by specific tests on different material, like polymers and oxides. AM05 is at present the functional that is first employed when facing a new problem in the areas of dynamical materials and high energy-density physics at Sandia.

Kubo-Greenwood response

While DFT readily described bulk properties like lattice constant, bulk modulus, surface relaxation, and other structural phenomena, Michael Desjarlais pioneered the use of linear response in the HEDP regime, with the first application being Al [21]. The conductivity of Al in the warm-dense matter regime was successfully investigated using the Kubo-Greenwood (KG) formula for conductivity [21]. The KG formulation gives the conductivity directly from the wave-functions of the system, without assumptions of, for example, relaxation times or cross-sections.

$$\sigma_{\mathbf{k}}(\omega) = \frac{2\pi e^2 \hbar^2}{3m^2 \omega \Omega} \sum_{\alpha=1}^{3} \sum_{j=1}^{N} \sum_{i=1}^{N} (F(\varepsilon_{i,\mathbf{k}}) - F(\varepsilon_{j,\mathbf{k}})) \left| \left\langle \Psi_{j,\mathbf{k}} \middle| \nabla_\alpha \middle| \Psi_{i,\mathbf{k}} \right\rangle \right|^2 \delta(\varepsilon_{j,\mathbf{k}} - \varepsilon_{i,\mathbf{k}} - \hbar\omega)$$

Eq. 1 Kubo-Greenwood conductivity.

Here, ε_i is the energy of state i, $F(\varepsilon_i)$ is the Fermi occupation, while $\left\langle \Psi_{j,\mathbf{k}} \middle| \nabla_\alpha \middle| \Psi_{i,\mathbf{k}} \right\rangle$ is the matrix element for optical transition between states j and i. We have used this approach for studying the electronic properties of Al, W, Cu, Alumina, and Al/Cu alloys. All materials are of importance to pulsed power components. The frequency dependent optical conductivity is also the foundation for calculation of the **q**-dependent electron loss function employed to calculated electron mean-free paths and scattering probabilities.

Calculation of work function from first principles

The work function is calculated as the difference between the Fermi energy and the vacuum level in a periodic structure, modeling surfaces and vacuum as shown in Figure 5. The work function

enters all modeling on surface emission, it's therefore a key quantity to calculate from first principles.

DFT calculation of work function for metals and surface oxides

We began by studying tungsten for two main reasons: its importance in the Z program and the availability of experimental as well as previous theoretical work. The first step in calculating the work function at finite temperature is a long QMD simulation, establishing equilibrium.

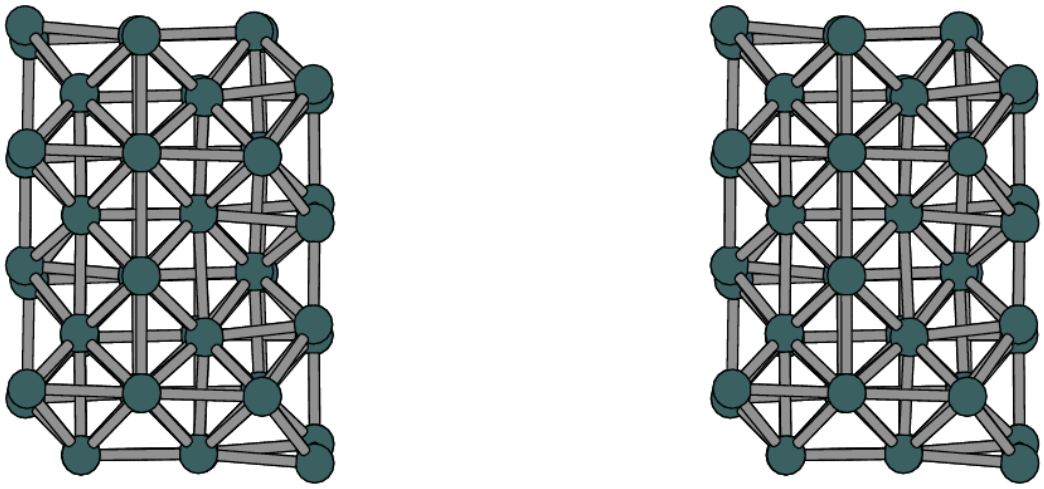

Figure 4. Side view of a 6 layer super cell of W(100), snapshot at 400 K.

Next, the approach is similar to that taken to calculate optical properties: post-processing, high-accuracy calculations of several (about 20) snapshots from the simulation. Figure 2 shows the local potential across the simulation cell (averaged in the two other directions) for two cases, 0 K and 700 K. Note the perfect symmetry of the 0 K calculation in comparison to the thermal disordered at 700 K.

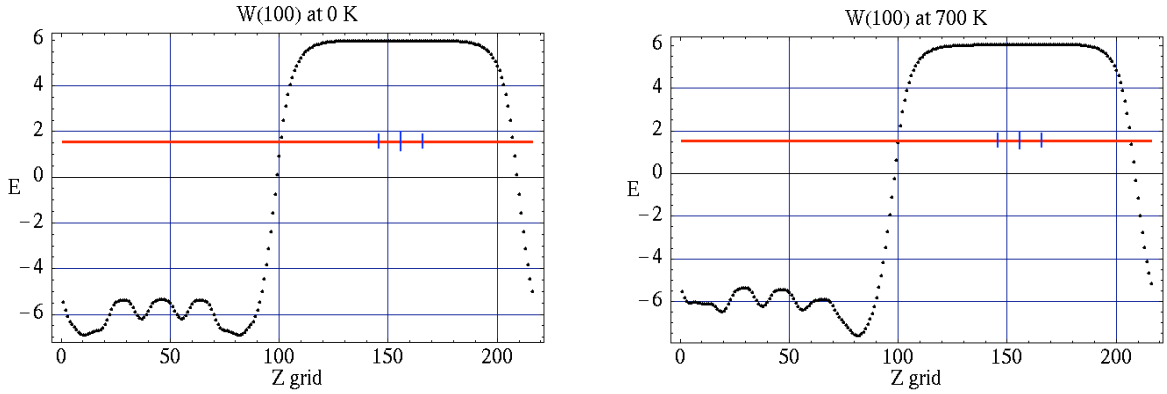

Figure 5. Electron potential energy across the full periodic super cell, including slab and vacuum regions (points), Fermi-energy (red), and interval over where the vacuum potential was sampled (blue): 0 K (left), and 700 L (right). At 700 K, the potential was averaged over 20 configurations extracted from a long QMD simulation.

With the capability developed to calculate work functions, we continued by studying the effects of temperature as well as surface impurities: alloying and initial oxidation. The change in work function with temperature as well as surface impurities is shown in Figure 6.

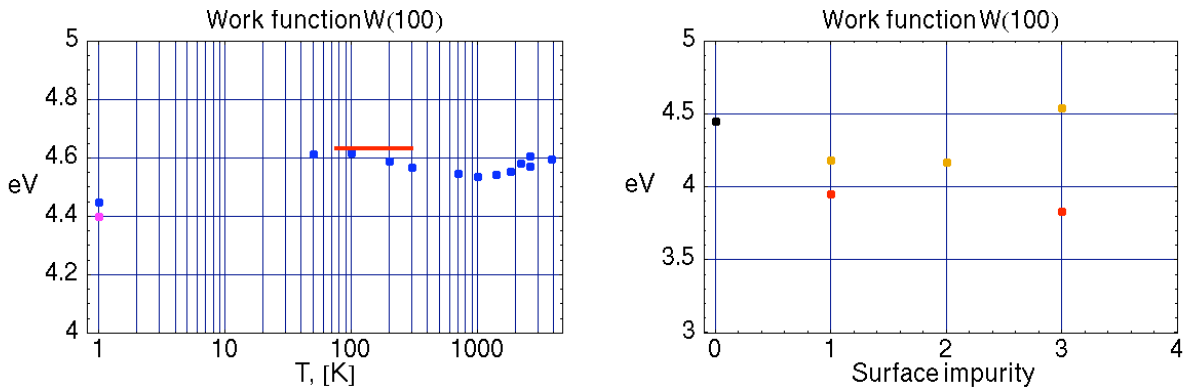

Figure 6. Left: work function for W(001) as a function of temperature: the present study (blue), experimental data [22] (red line), and DFT results at 0 K [23] (purple). Right: work function at 0 K when substituting surface W atoms with O (red) and Cu (orange), surface alloying affects the work function significantly. The theoretical results were presented at an APS meeting [24].

Following tungsten, we studied Cu and Al before turning to surface oxides. How the surface structure and work function changes with oxidation of Al, including interfacing with the intrinsic alumina layer of a natural aluminum surface. Figure 1 shows progressive oxidation of Al. Results were presented at the APS March meeting in New Orleans 2008 [24].

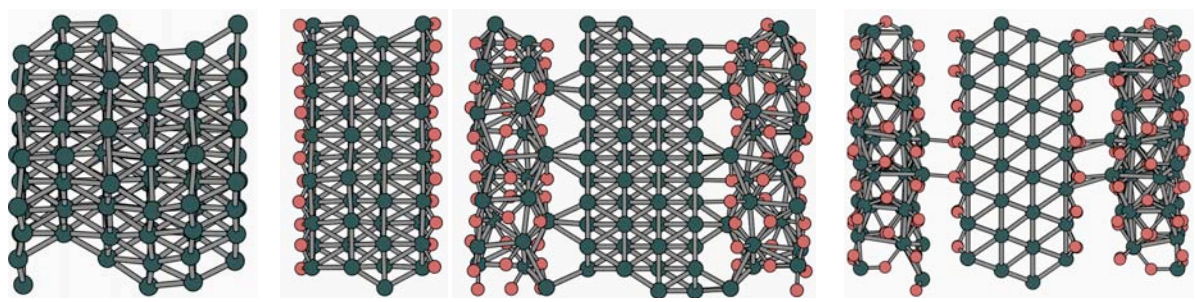

Figure 7. Four cells used to investigate the effect of oxidation on the work function of Al. Bare Al (111) (Φ=4.2eV); Al(111) with chemisorbed O (Φ=4.97 eV); Al(111) interfaced with κ-Alumina (Φ=5.06 eV); Al(111) with chemisorbed O interfaced with κ-Alumina (Φ=6.92 eV). The formation of a chemisorbed layer in combination with the oxide significantly enhances the work function.

Work function of Alumina

Not only metals are of interest, but also oxides. We chose to look at alumina due to its use as a dielectric in high-voltage applications as well as natural occurrence in surfaces of aluminum, see Figure 7.

Our initial lattice used the ***K***-phase of alumina with 24 oxygen atoms and 16 aluminum atoms. The beginning lattice [25] was

$$m = \begin{bmatrix} 4.8041 & 0 & 0 \\ 0 & 8.2543 & 0 \\ 0 & 0 & 8.8785 \end{bmatrix} * s$$

where s was used to vary the density over a narrow range. We used VASP 5.1 with an energy cutoff of 800 eV, the AM05 functional, and a 4x4x4 gamma centered Monkhorst k-point set. A majority of the simulations were run on RedStorm using a massively parallel implementation by Paul Kent [26]. The simulations were run triply periodic at 0 Kelvin to map out a cold curve and estimate where VASP predicted the rest state for the material was (see Figure 8). Using a quadratic fit to the cold curve points, the minimum energy was estimated at s = 1.0080861.

We used this lattice as the starting point and varied the matrix elements to get a better approximation of the VASP calculated rest energy and density.

$$m = \begin{bmatrix} 4.8430 * x & 0 & 0 \\ 0 & 8.3210 * y & 0 \\ 0 & 0 & 8.9503 * z \end{bmatrix}$$

x, y, and z were changed from 0.95 to 1.05 by 0.01 independently so we had a volume in which to find the minimum. We used Mathematica [27] to create a fit function to the 1000 cold curve simulations and used the FindMinimum[] function to calculate what x, y, and z corresponded to the minimum energy. Figure 9 shows the over lapping surfaces (energy[x,y]) where each surface is a different z. We then did the same thing but using the LDA potential. We compared the results of the AM05 potential and LDA potential and found that AM05 was closer to the experimental data adjusted to 0 Kelvin.

Table 1. Lattice values at the calculated minimum energy.

	X	Y	Z	Density
Ref 28	4.831	8.300	8.923	3.7857
Ref 29	4.840	8.321	8.945	3.7598
LDA	4.81368	8.26528	8.88001	3.8346
AM05	4.84558	8.32836	8.95626	3.7475

Once we had the lattice values, we then doubled the number of atoms in all three directions for a total of 320 atoms.

$$m = \begin{bmatrix} 9.6912 & 0 & 0 \\ 0 & 16.6567 & 0 \\ 0 & 0 & 17.9125 \end{bmatrix}$$

We ran this configuration as a molecular dynamics simulation at 300 Kelvin, 1200 Kevin, and 1800 Kelvin until the energy and pressure equilibrated. The MD simulations were done using one complex k-point (0.25,0.25,0.25). Once the simulations had equilibrated, a vacuum was introduced in one direction (*x*) and re-equilibrated. Figure 15 shows the periodic block structure used to calculate the surface potential. In reality, there is no second block and a periodic boundary is assumed. The total simulated volume is expanded by *x**1.6 for a vacuum of 5.815 A between blocks. VASP failed to converge for a vacuum larger than that.

After the vacuum simulations had equilibrated, we calculated the local potential for ten different time slices starting from the last one and taking every 17th one from there. The potential was averaged in *y* and *z* for each *x* (see Figure 16) and the difference between the Fermi energy and the void for each temperature.

Table 2. Work function energy for *K*-phase alumina.

	300 Kelvin	1200 Kelvin	1800 Kelvin
K-Alumina	4.830eV	4.874eV	4.537eV

Also, the 300 Kelvin non-void simulation was a perfect insulator, but when void was introduced, the material because more conductive (many of the bands showed partial occupation), due to surface states not present in the pure bulk oxide.

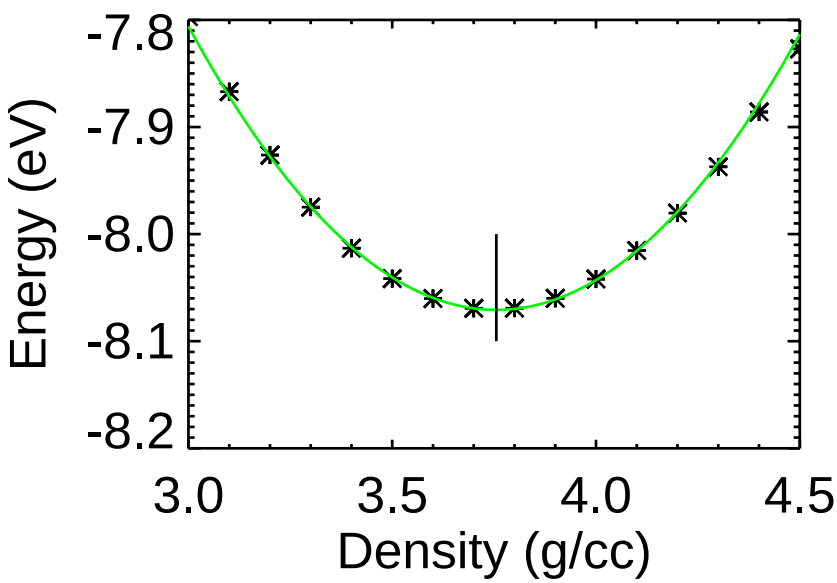

Figure 8. VASP calculated cold curve for *K*-phase Alumina.

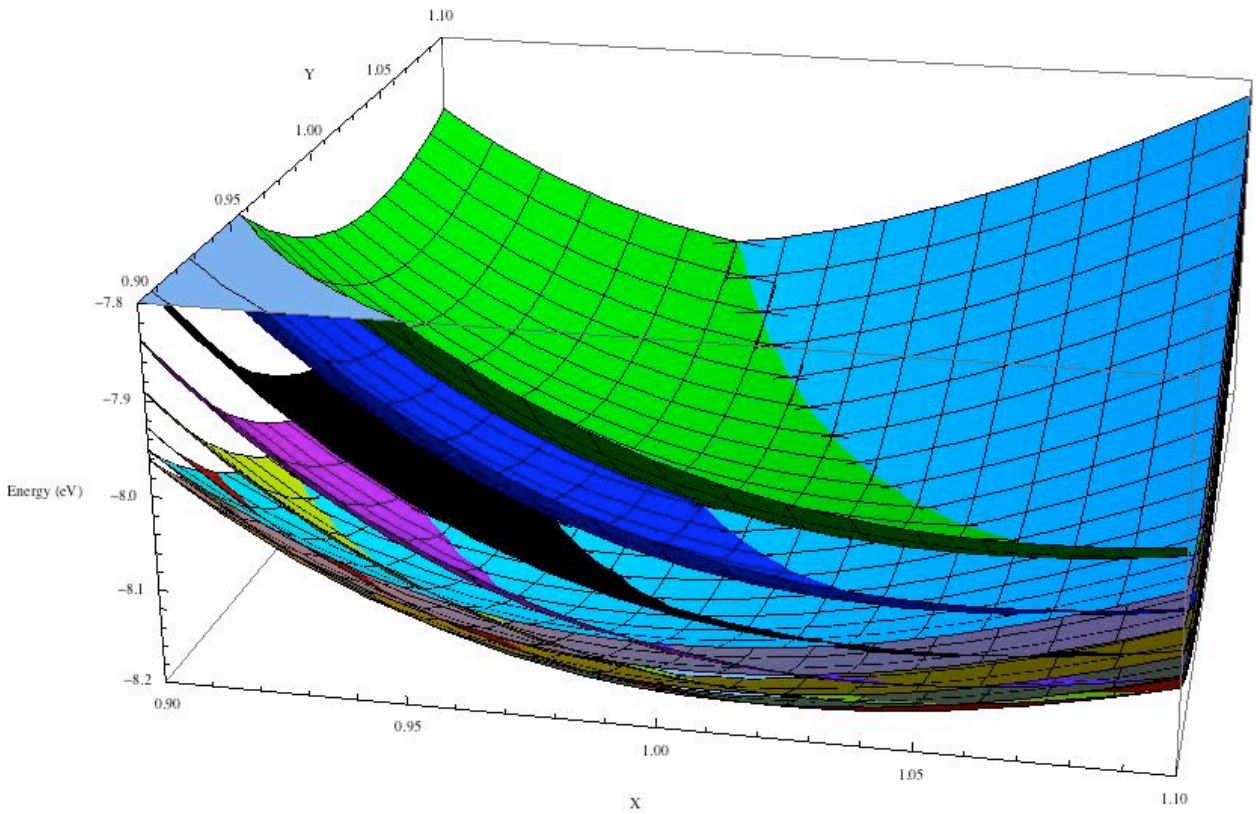

Figure 9. Over lapping surfaces (energy[□□]) where each surface is a different □, the plot simultaneously illustrates minimization in the three lattice parameters of K-alumina.

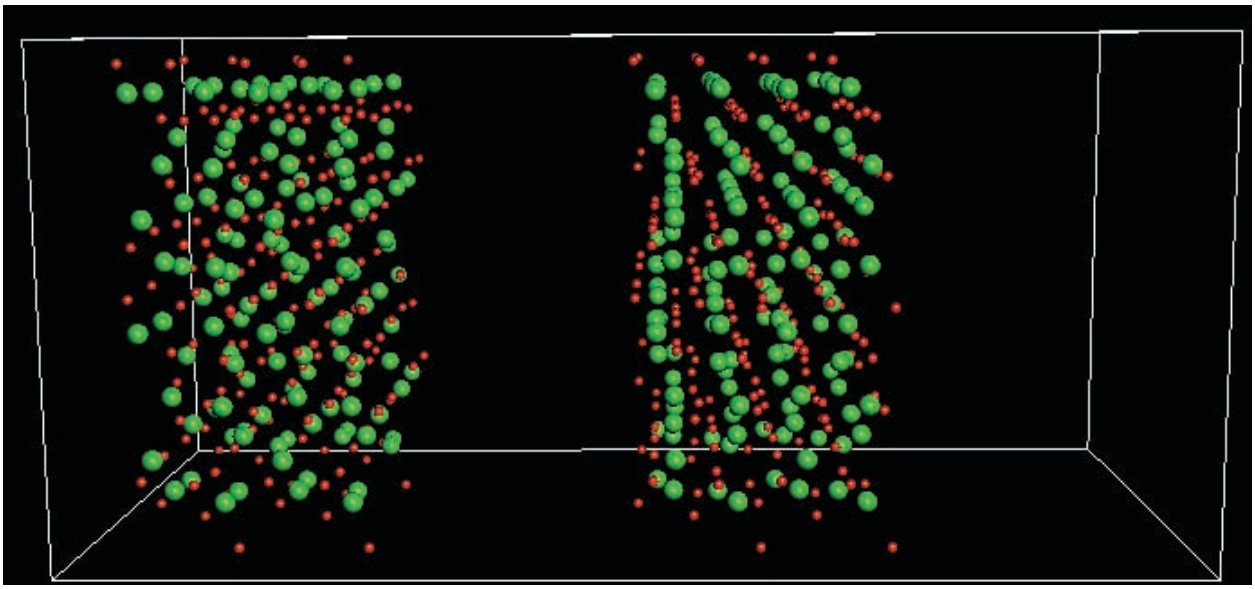

Figure 10. Simulation space of the slab geometry, with the periodicity of the simulation shown. The second block of atoms is not actually used. These atoms are shown in their perfect *K*-phase alumina position before being equilibrated at a finite temperature.

Work function of Copper

Copper is an FCC metal and periodic in all three directions. Therefore we would use just the cold curve to find the minimum energy. The energy cutoff was 800 eV and the k-points were a 24x24x24 gamma-centered Monkhorst k-point set.

Table 3 Reference energy by pseudo-potential for FCC copper at 0 Kelvin.

Pseudo-potential	Reference Density (g/cc)
LDA	9.645
PBE	8.785
AM05	9.300

We ran 28 atom simulations (7 layers with 4 atoms in each layer) to steady state at 100 Kelvin and 700 Kelvin using all three pseudo-potentials at their respective reference densities and an 4x4x1 Monkhorst k-point set. To calculate the work potential, we changed the k-point set to 8x8x1 and used 10 time slices gapped 50 cycles apart. The amount of void was approximately 13 A. Table 4 shows the work function energy results.

Table 4. Work function energy for copper for each pseudo-potential at 100 and 700 Kelvin.

Pseudo-potential	100 Kelvin	700 Kelvin
LDA	4.881 eV	4.887 eV
PBE	4.491 eV	4.469 eV
AM05	4.481 eV	4.484 eV

For copper, we performed one simulation using 108 atoms in the simulation (4 atom basis cell expanded 3 times in each direction) and found our work energy to be approximately 4.2eV, within 0.2 eV from experimental data [30].

Inelastic electron-electron scattering from first principles: Cu.

The work function is needed in order to estimate the emission of electrons from the surface: a high work function leads to fewer emitted electrons. The second step in calculating surface electron emission is to model electron scattering, in particular inelastic processes. To this end, we calculate the optical properties of the material and derive the q-dependent electron-electron interaction [31,32].

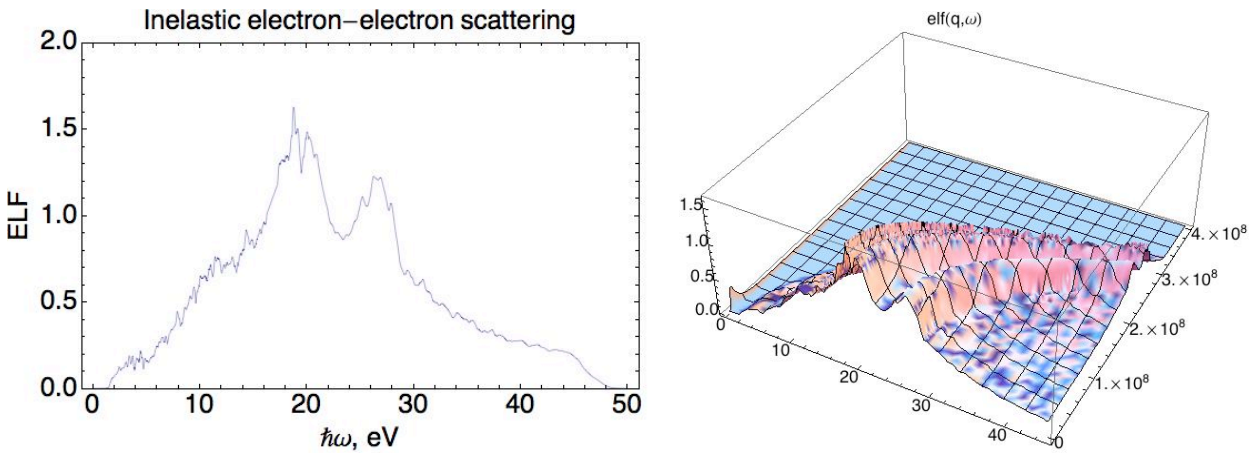

Figure 11 Electron energy loss function ELF(ω) for Cu from QMD (left). Q-dependent electron energy loss function ELF(q,ω) (right) derived by solving for ω in the dispersion relation.

The inelastic scattering is key to modeling secondary electron emission: it determines the probability for electrons to loose energy in the material as secondary electrons are emitted. When combined with a model for elastic scattering, we thus have a description of electron dynamics in a surface region. The processes are suitable for Monte Carlo (MC) type simulations. Our initial attempt to employ an existing electron-electron scattering MC code [33] was unsuccessful due to the code's limited real-space treatment. We instead programmed a Monte Carlo routine in Mathematica. The Mathematica alternative has an advantage in that it has been integrated with the existing Mathematica programs/notebooks for optical properties.

The MC simulation currently includes: energy and momentum (vector) conservation, elastic electron scattering, inelastic (secondary) electron scattering derived from QMD, random initial distribution of electrons depending on frequency, and finally surface emission depending on the work function calculated from QMD. It is straightforward in the code to refine the scattering processes as well as the surface emission probability as a function of energy.

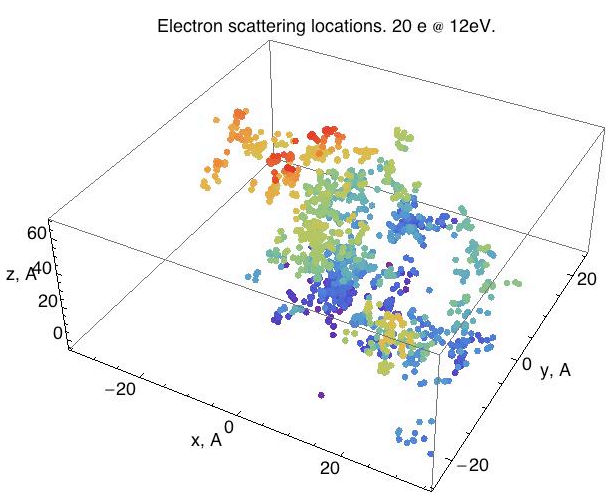

Figure 12. Points of scattering for 20 initial electrons at 12 eV in the region close to the surface. Vacuum is Z<0 and the color coding is with respect to distance to the surface (blue close to surface, red deep in the bulk) (right). Electron emission probability for different photon energies; 500 electron trajectories were initiated and followed for each initial energy.

Beyond DFT, applying GW theory to a wide-gap insulator – alumina

Metals are well described by DFT, also properties like DC conductivity and low-energy optical absorption. However, the same cannot be said about semiconductors and insulators. In this section, we will discuss and describe how a many-body theory can be applied to with high accuracy calculate excited states. We chose to investigate the electronic structure and dielectric function of alumina, Al_2O_3. Alumina is an important insulator, used as high-voltage insulation in general and in pulsed power components in particular.

Introduction and description of method

Alumina, or α-Al_2O_3 is one of the main constituents of minerals, and its electronic structure is of great interest for mineralogists. Technologically, the α-Al_2O_3 is insulator with large band gap and is able to remain transparent even after exposures to high doses of radiation. It is one of most important ceramic materials with exceptional properties such as great hardness, chemical inertness, and high melting temperature. These properties have made alumina a material of frequent use in technological applications such as catalysis, coating, microelectronics, composite materials, advanced material technology and high energy density physics. The study of alumina is also important because Al_2O_3 can be considered as the final stage in the oxidation of Al surfaces.

During the last few decades α-Al_2O_3 has been studied both experimentally and theoretically. A review of its properties was given by French [34]. The first-principle calculations of electronic structure for α-Al_2O_3 were performed in framework of density functional theory (DFT) using LDA of GGA approximations [34-41]. As expected, the DFT approach underestimates the band gap of alumina, giving the band gap in a range 6.2-6.6 eV, depending on method used. The experimental band gap at zero temperature is 9.13 eV [34] (room temperature gap is measured to be 8.8 eV with linear temperature dependence coefficient –1.1 meV/K in range of temperatures from 300K to 900K). Some other features of electronic structure calculated in DFT also do not agree well with experiment. For example, position of lower valence band (LVB) is predicted to be 16-17 eV below the valence band maximum (VBM), while x-ray photoemission spectroscopy (XPS) puts it near 20 eV below VBM [41]. The aim of the first part of present report is to calculate the electronic structure of α-Al_2O_3 by recently developed [42-44] quasiparticle self-consistent GW (QSGW) approach that proved to be very successful in describing electronic structure and other properties of wide classes of materials, and, in particular, improves the agreement of calculated band gaps for semiconductors and insulators with experiment [43].

I start with very brief overview of LDA/DFT and QSGW methods. In LDA/DFT theory the wave functions and energies are obtained from the Kohn-Sham equation

$$\left[-\nabla^2/(2m) + V^{ext} + V^H + V^{xc}\right]\psi_n^q = \varepsilon_n^q \psi_n^q . \qquad (1)$$

Here V^{ext} is external potential, V^H is Hartree potential and V^{xc} is LDA exchange-correlation potential. In GW theory quasiparticle wave functions and energies are obtained from similar equation except energy-dependant and, in general, non-hermitian self-energy term $\Sigma(\varepsilon)$ substitutes the LDA exchange-correlation potential. In QSGW approach [42-44] we transform the self-energy to *energy independent* and *hermitian* matrix

$$\Sigma_{nn'}^q = \mathrm{Re}[\Sigma_{nn'}^q(\varepsilon_n^q) + \Sigma_{nn'}^q(\varepsilon_{n'}^q)]/2 . \qquad (2)$$

Here *n* and *n'* are band indexes of wave-function in modified Kohn-Sham equation

$$\left[-\nabla^2/(2m) + V^{ext} + V^H + \Sigma\right]\psi_n^q = \varepsilon_n^q \psi_n^q . \qquad (3)$$

Self-consistency of self-energy is obtained by iterations. Converged self-energy (obtained from Σ=GW formula) is equal to self-energy in Eq. (3) (within some small tolerance) that was used in calculations of wave functions, quasiparticle energies, and, consequently, Green function G and dynamically screened Coulomb interaction W. We argue [42-44] that self-consistent calculations with self-energy constructed by Eq. (2) are more physically sound compare to one-short GW or conventional self-consistent GW calculations. The QSGW approach is consistent with Landau-Silin quasiparticle theory while conventional self-consistent GW is not. The present QSGW method is considered today as the most accurate method for electronic structure calculations in solids and has been implemented recently by two well-known groups in Europe: VASP and ABINIT groups.

Electronic structure of Al_2O_3

Now I turn to calculation of electronic and optical properties of α-Al_2O_3. The coordinates of four Al and six O atoms in the α-Al2O3 and unit cell translation vectors are taken from web-page http://cst-www.nrl.navy.mil/lattice/struk/d5_1.html [45]. The well converged self-energy calculation was obtained with nk=3 divisions along each axis in k-space (one-shot calculations with nk=4 shows quasiparticle energies difference less the 0.02 eV). Approximately one day of single-processor (AMD Opteron 2222 SE with 3GHz frequency) CPU time takes to complete one GW iteration for nkgw=3. Four GW iterations were enough to reach the self-consistency in

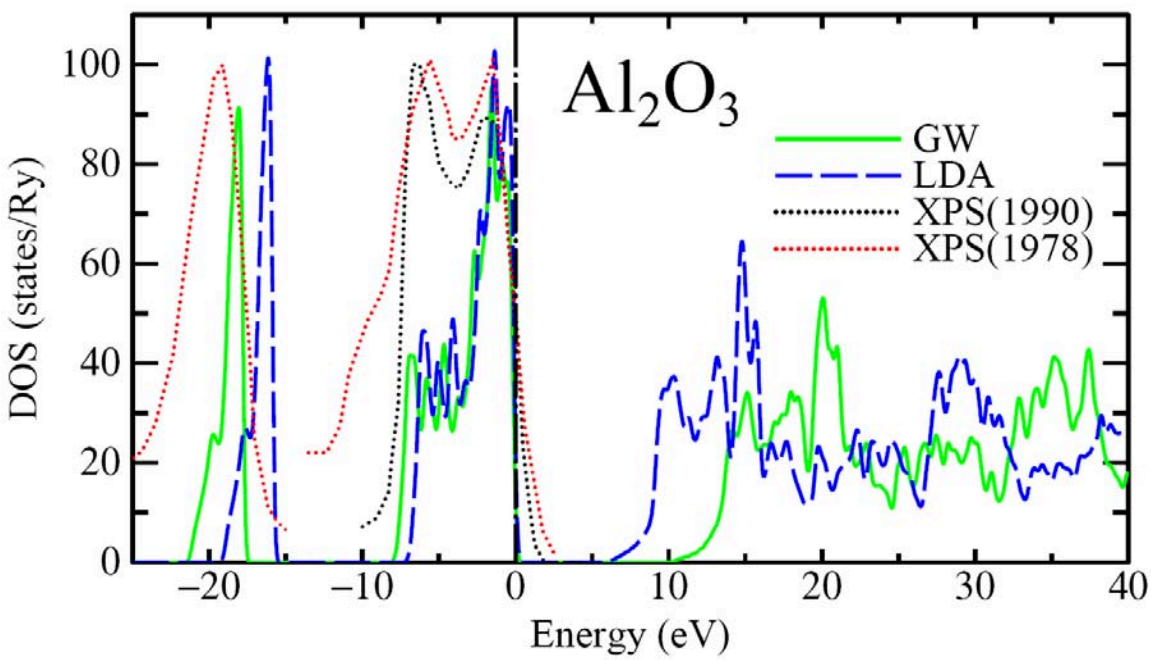

Figure 13. DOS of α-Al2O3: QSGW (green solid line) and LDA (blue dashed line). XPS data of 1976 experiment, Ref. [41] (red dotted line), and data of 1990 experiment, Ref. [34] (black dotted line), are shown normalized to height of LVB and UVB peaks. Zero on the figure is valence band maximum (VBM).

self-energy.

The LDA and QSGW density of states (DOS) of α-Al_2O_3 (calculated here as sum of projections of partial DOS to muffin-tin spheres of all 10 atoms) is shown on Figure 13 in comparison with experimental XPS data. We see that position of LVB calculated in QSGW shifts to lower energies compare to LDA in agreement with position of experimental XPS peak near –20 eV. The width of UVB is increased in QSGW compare to LDA, also in agreement with XPS data (black dotted line on Fig. 1). The shoulder-like structure at -10 eV in earlier 1976 experiment contradicts the theoretical DOS, both LDA and GW. This shoulder is considered to be due to surface contamination [35] in earlier XPS data and is absent in recent XPS data [34] and x-ray-emission spectra [46].

The band structure of α-Al_2O_3 calculated by LDA and QSGW methods is shown in Figure 14. I obtain direct Γ-Γ band gap in both LDA and QSGW approaches (some earlier calculations [35] reported indirect band gap, just slightly smaller then Γ-Γ gap, but newer calculations [37] suggest that the gap is direct). It is seen that GW significantly change the LDA picture: band gap increases from 6.18 eV to 10.18 eV, widths of lower and upper valence bands (LVB and UVB) increase and center of LVB shifts to lower energies. The 1.05 eV error of QSGW band gap is significantly less then the LDA error of 2.95 eV.

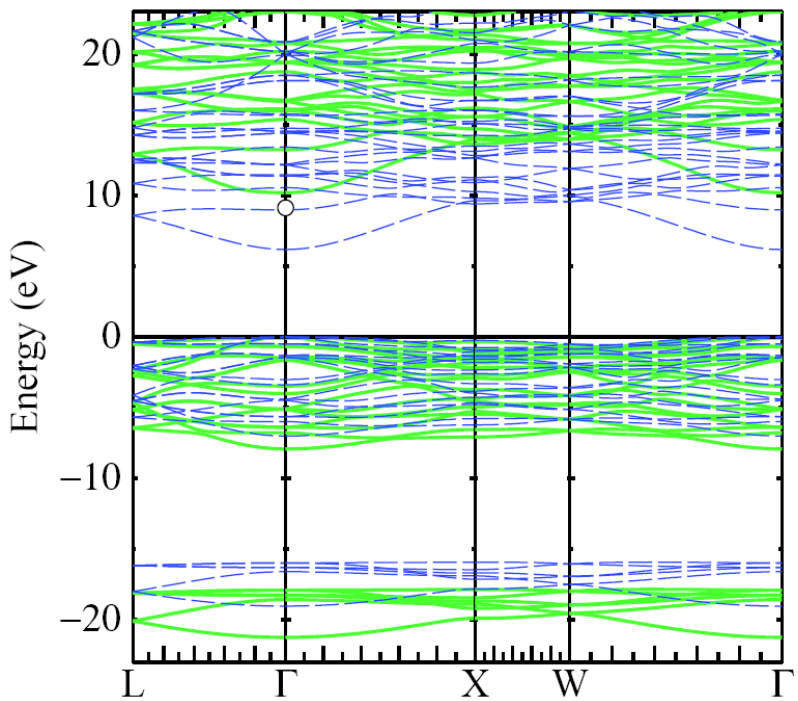

Figure 14. Band structure of α-Al2O3.: GW (green solid line) and LDA (blue dashed line). Experimental band gap 9.13 eV [34] at zero temperature is shown at Γ point.

In order to analyze remaining GW band gap error, the band gaps for over 30 *sp* semiconductors and insulators calculated in LDA, one-shot GW and QSGW [43] are shown in Figure 15. Left panel of Figure 15 shows LDA band gaps and one-shot GW band gaps as function of experimental gaps. We see that LDA significantly underestimate the gaps, with average error of the order of 1-2 eV, (including 2.95 eV underestimation for α-Al_2O_3, shown by read arrow in Figure 15.

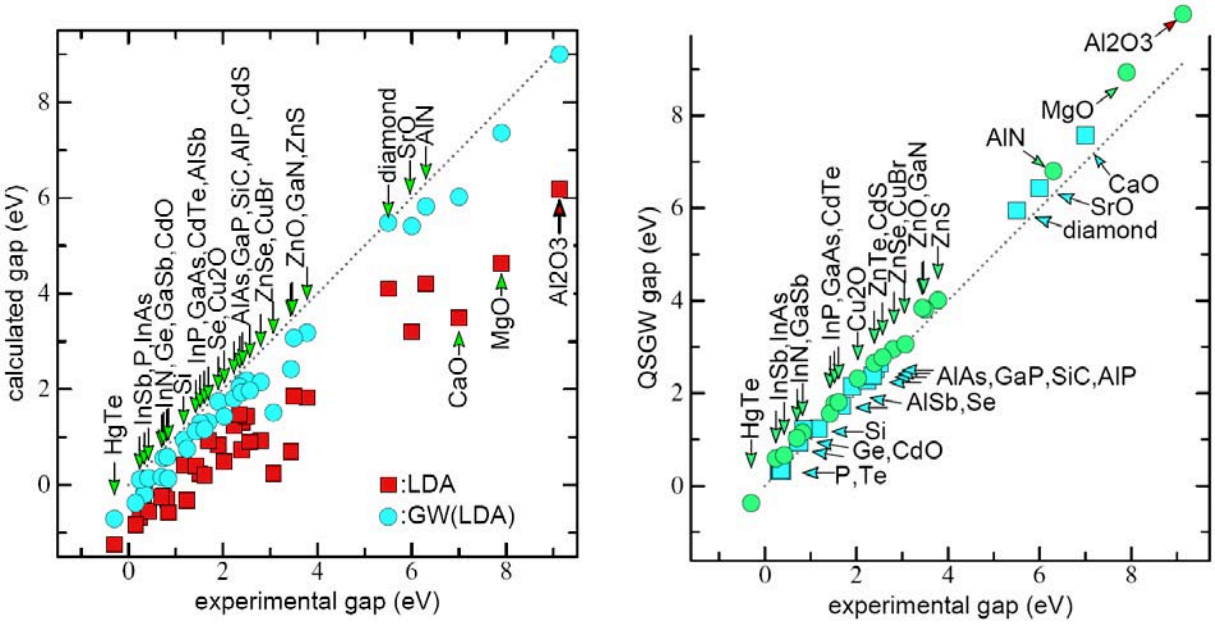

Figure 15. Horizontal axis - experimental band gaps, vertical axis – calculated band gaps. Left panel: LDA (red squares) and one-shot GW (circles) gaps; right panel: QSGW gaps. Results for α-Al2O3 are shown by red arrow in both panels.

One-shot GW produces much better results, but it still underestimates the gaps with an average error of the order of 0.5 eV. The QSGW results shown on right panel of Figure 15 show even better accuracy: average error of the order of 0.1-0.2 eV, errors that tend to be smaller for low-band gap systems. Another point to notice is that, unlike LDA and one-shot GW, the QSGW band gap error is highly systematic. QSGW systematically (slightly) overestimate the band gaps and the error worsens for higher band gap materials; one can drew a straight line through the QSGW band gap results. The largest QSGW error on the right panel of Figure 15 is 1.03 eV for α-Al_2O_3 (which has largest band gap).

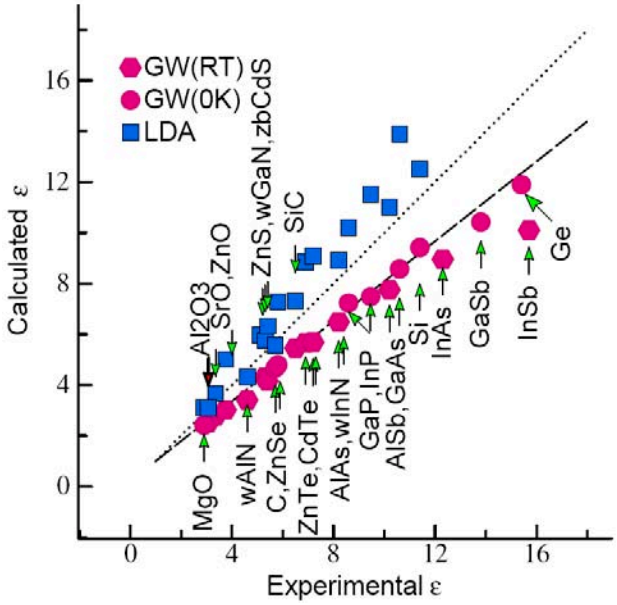

Figure 16. LDA and QSGW dielectric constants in comparison with experiment. Results for α-Al2O3 are shown by read arrow.

In order to explain the systematic overestimation of the band gaps in QSGW in Figure 16 the dielectric constants calculated by LDA and QSGW methods for number of materials (for α-Al_2O_3 it is shown by red arrow). We see that LDA dielectric constants are more or less close to the experiment (although in a non-systematic manner), while the QSGW dielectric constants are systematically underestimated. The line at 20% underestimation of ε is shown on Figure 16 describes the

general QSGW trend. We argue [43] that systematic 20% underestimation of dielectric constant in QSGW is due to neglect of exitonic effects (electron-hole interactions) in calculation of polarization operator.

The LDA dielectric constant seemingly good agreement with experiment is coincidental and is actually due to cancellation of two independent errors: (1) neglect of exitonic interaction (that would reduce electron-hole excitation energy in calculation of polarization function, *P*), and (2) underestimation of the band gaps (that would increase electron-hole excitation energy in evaluation of *P*). The GW results correctly describe band gaps (at least compare to LDA), but still neglect electron-hole interaction. Neglect of electron-hole interaction leads to increase of the electron-hole excitation energy, that decreases calculated polarization operator, underestimates dielectric constant (see Figure 17), that, in turn, underscreen Coulomb interaction W [schematically, $W=V(1-VP)^{-1}$]. Thus, self-energy [schematically, $\Sigma=GW$] and obtained band gaps are overestimated. The small error in dielectric function (or polarization operator) is more pronounced when the dielectric constant itself is small. Because the dielectric constant is small for wide band-gap semiconductors, the band gap overestimation is larger when the band gap is large. Thus, the error should increase roughly proportional to the band gap, as conformed on right panel of Figure 3, reaching from 0.1-0.2 eV for small band gap materials to 1.03 eV error for α-Al_2O_3.

In order to *estimate* the exitonic effect we have been using a simple rule, namely we scale the GW addition to LDA Hamiltonian, Σ-V^{xc}, by factor 0.8 (such renormalization make sense because dielectric constant is too small by a nearly universal factor of 0.8, (see Figure 16). This rule works very well in simple semiconductors, and a number of insulators like MgO and $SrTiO_3$. For example, the gap of MgO is 7.8 eV; QSGW puts it at 8.9 eV. The scaled-sigma result is ~7.9 eV for MgO. Applying this simple "scaled (Σ-V^{xc})" rule to α-Al_2O_3 we obtain band gap 9.39 eV.

Another source of band gap error is zero-point motion (ZPM) effect that renormalizes the band gap due to small quantum oscillation of lattice at zero temperature. The ZPM effect is larger for lighter materials, such as diamond, AlN, MgO, and Al_2O_3. In diamond, this effect leads to reduction of the gap by ~0.5 eV; in MgO by ~0.3 eV, and in AlN by 0.24 eV. In α-Al_2O_3 ZPM effect is presently not calculated, but it should be around 0.3 eV – larger then for AlN because the O/Al ratio (lighter to heavier component) in Al_2O_3 is bigger than the N/Al ratio in AlN. Thus, combining "scaled (Σ-V^{xc})" rule that mimic effect of electron-hole interaction, and ZPM effect, we obtain the *estimation* of α-Al_2O_3 band gap ~9.09 eV that is in prefect agreement with experimental value 9.13 eV.

Dielectric function of Al_2O_3

The dielectric function of α-Al_2O_3 has been calculated by several authors within DFT [35-37] and all obtained similar shape of Im(ε). Also the position (at 12-13 eV) and amplitude (~5.5) of main peak in Im(ε) is similar in these works. The Im(ε) calculated within LDA approach in this work and by Holm et al. [35] is shown on Figure 17 together with experimental data [47]. Our LDA dielectric function is very close to dielectric function obtained by Holm et al. except the second peak in Im(ε), located at 16 eV, is less pronounced and 18% smaller in our calculations. The agreement of the LDA calculations with experiment seems reasonably good. Some disagreement is in position of onset of Im(ε). It is at ~6 eV in LDA, while it is at ~8 eV in the experiment. This is due to mentioned above underestimation of the band gap in LDA. Also the maximum of main experimental peak is located at 13 eV, while in LDA it is at 11 eV.

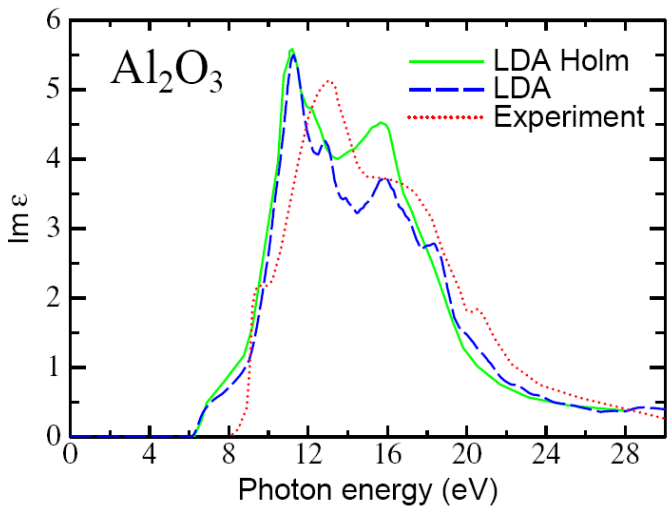

Figure 17. Imaginary part of dielectric function calculated by LDA approach: this work (blue dashed line), Holm et al. [37] (green solid line). Experimental data [47] is shown by red dotted line.

The imaginary and real part of dielectric function of α-Al_2O_3 calculated within LDA and QSGW approaches are shown on Figure 18 together with experimental data [47]. The peak of Im(ε) calculated in GW is shifted by ~5 eV to higher energies and is also reduced in amplitude compare to LDA. The structure of real part of ε also shifts to higher energy. At zero photon energy the dielectric constant ε_∞ is 2.52 in QSGW; 3.12 in LDA; and 3.07 in experiment, thus GW underestimation the dielectric constant by 18%, that agree with general GW trend of 20% underestimation (see Figure 16). Overall, GW seems to make things worse and destroy the agreement of LDA and experiment. Again, the artificial agreement of LDA with experiment is due to cancellations of two independent errors: band gap underestimation and neglect of electron-hole (e-h) interaction. In GW the band gap is more accurate then LDA, but neglect of e-h interaction results in shifting the position of the peak in Im(ε) to higher energies.

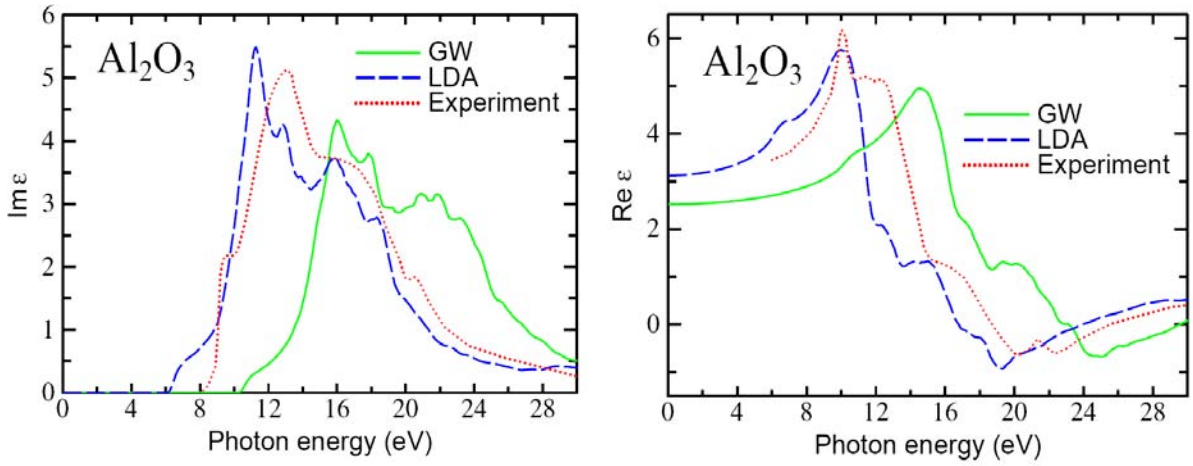

Figure 18. Imaginary (left panel) and real (right panel) parts of dielectric function of α-Al2O3 calculated by LDA (blue dashed line), and QSGW (green solid line) approaches. Experimental data [47] shown by red line.

To further highlight importance of e-h interaction for calculation of ε(ω) I present on Fig. 7 experimental and theoretical dielectric function for MgO. MgO is similar to α-Al_2O_3 compound: Mg and Al are neighbor elements, MgO and Al_2O_3 have similar large band gap and small dielectric constant, and, consequently, *both materials have strong e-h interaction due to weak screening*. Dielectric function for MgO has been recently calculated [48] with inclusion of e-h interaction within Hanke-Sham framework. Analogously to Al_2O_3 case, the overall LDA position of Im(ε) structure for MgO seems in better agreement with experiment as compare to GW. Again, similarly to Al_2O_3, the detailed peak structure of LDA Im(ε) is not in good agreement with experiment, including the ~3 eV underestimation of the onset point and missing peaks at 13 eV and 17 eV.

Benedict et. al [48] calculated Im(ε) of MgO staring with quasiparticle (QP) electronic structure: they stretched the LDA valence and conduction bands by 14%, and 2% to mimic the results of quasiparticle calculations (though they did not change LDA wave functions). Also, they used the MgO band gap 7.8 eV and dielectric constant ε_∞=3.03 as input in their calculations. The Im(ε) obtained in Ref. [48] without inclusion of e-h interaction, denoted as 'QP no e-h' on right panel of Fig. 7, is very similar to our QSGW Im(ε) shown on left panel of Fig. 7. Importantly, theoretical result for Im(ε) obtained by Benedict with included e-h interactions is very close to experimental curve. Thus, we can expect to obtain similarly good result in QSGW if we include the e-h interactions.

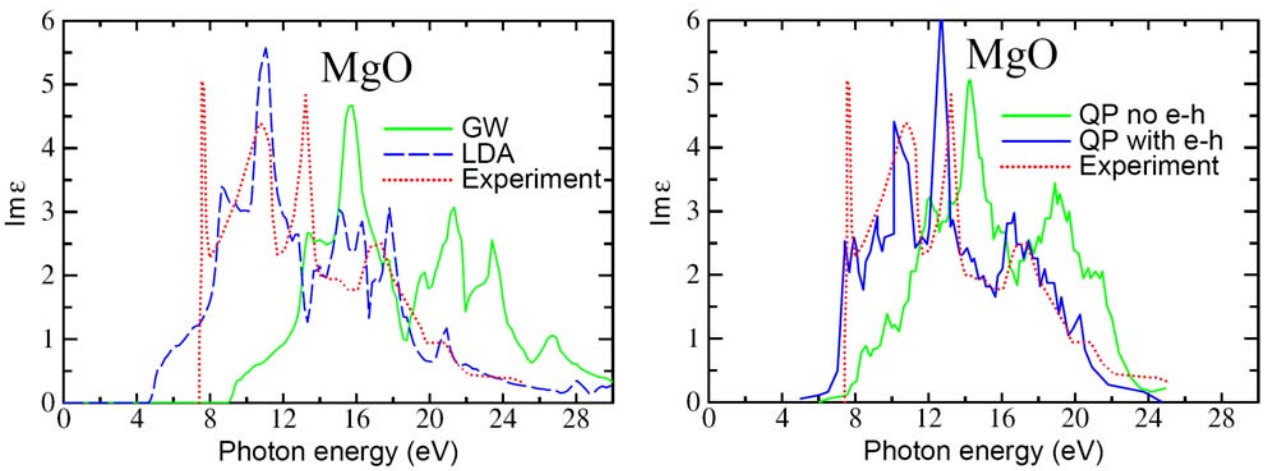

Figure 19. Imaginary part of MgO dielectric function. Left panel - result of present calculations: LDA (blue dashed line) and QSGW (green solid line); right panel – result of quasiparticle calculations [48] without (green solid line) and with (blue solid line) inclusion of electron-hole interactions. On both panels red dotted line shows experimental result [49].

Work function of Al using self-consistent GW

DFT gives a satisfying description of work functions for metals, but the treatment of oxides is more questionable. As described in the last section, GW gives an improved description of optical properties. We therefore investigated if GW can be used for calculations of work functions. We use Al as the first case. Traditional GW lacks a total energy description, prohibiting direct calculation of the work function, however, we were able to formulate a reference potential in the QSGW framework as described in the next section.

Introduction and description of method

The aim of the second part of this project is to determine feasibility of work function (WF) calculation within the QSGW approach. Another aim is to check accuracy of different DFT functionals by comparing the WF obtained in QSGW and DTF methods. The QSGW method is accurate, but it is very computationally demanding. Several years ago the system with 8 atoms in unit cell was maximum QSGW calculation could handle. Nowadays, computers become faster and reliable calculation of the work function that requires ~6-10 layers of metal and 6-10 vacuum layers are feasible.

We employ all-electron full-potential linear muffin-tin orbitals (LMTO) method [44,50] with muffin-tin orbitals as basis functions in metal region and floating orbitals basis in vacuum region. It is convenient to place the floating orbitals at the coordinates where metal atoms would be in bulk. Thus, distance between adjacent vacuum layers is the same as between metal layers. The unit cell of the system consists of N_M metal layers and N_V vacuum layers. There is one metal atom per layer and system is periodic in all three dimensions, so metal and vacuum slabs with total N_M+N_V layers are periodically repeated in z-direction.

The definition of work function is

$$w = V(0) - E_F\,, \qquad (4)$$

where $V(0)$ is the reference potential (potential in vacuum far away from metal surface). In DFT, $V^{DFT}(0) = V^{ext}(0) + V^{H}(0) + V^{xc}(0)$, where $r = 0$ is the middle of vacuum slab. The GW quasiparticle Hamiltonian (3) has the form $H^{QP} = H^{LDA} + (\Sigma - V^{xc})$, where $(\Sigma - V^{xc})$ term is hermitian and energy independent, but non-local. We rotate the $(\Sigma - V^{xc})^{q}_{mm'}$ matrix of Eq. (2) from **q**-space and wave-function representation to real-space and MTO basis representation: $(\Sigma - V^{xc})_{R,l,m;R'+T,l',m'}$, where *R* describe position of atom (or floating orbital) in unit cell, *(l,m)* is angular quantum number and its *z*-projection, and *T* is the real-space translation vector. We define the reference potential in QSGW approach as

$$V^{QP}(0) = V^{ext}(0) + V^{H}(0) + V^{xc}(0) + (\Sigma - V^{xc})_{0,0,0;0,0,0}\,, \qquad (5)$$

where *R=0* is the position of floating orbital in the middle of vacuum slam (or closest to the middle, if N_V is even). We project self-energy to *s*-character basis function (*l=0*) in the middle of vacuum slab because an unbound state with minimal energy, $|\Psi_m\rangle$, has *s*-character in the region far away from metal surface [it is constructed from exponents exp(i**kr**) with **k**≈0]. Thus, the quasiparticle energy of such state is

$$\langle \Psi_m | H^{QP} | \Psi_m \rangle \cong V^{ext}(0) + V^{H}(0) + V^{xc}(0) + (\Sigma - V^{xc})_{0,0,0;0,0,0} = V^{QP}(0)\,, \qquad (6)$$

where we neglect matrix elements $(\Sigma - V^{xc})_{R,l,m;R,l,m}$ between different sites *R*, *R'* in vacuum region (in our calculations we checked that such matrix elements are small compare to diagonal term) and use the fact that kinetic energy is zero.

Work function of Al (001) surface

As for any first principal code, there are several (cutoff) parameters in the QSGW code that should to be checked in order to obtain reliable results. In calculation of the work function three parameters affect the CPU time the most: number of k-point divisions along x and y axis in calculation of the self-energy – nk (we use just one k-point along *z*-direction); number of metal layers (atoms) - N_M; and number of vacuum layers - N_V.

Table I shows results of LDA and QSGW calculations with different nk, N_M (M=Al), and N_V, as well as CPU time required to complete one GW iteration for Al (001) surface (typically, number of GW iterations to reach self-consistency varies from 4 to 8). The WF data is also shown on Figure 8 as function of N_V. We see that set of parameters N_{Al}=6, N_V=8, and nk=6 is enough to reach 0.05eV accuracy of the WF. For such parameters the QSGW work function is 4.44 eV. WF increases by ~0.07 eV for larger nk=8 (as can be concluded from Table I), while increase N_{Al} to 8 will result in decrease of WF by ~0.05. Thus our best estimate of QSGW work function of Al (100) surface is 4.44 eV, which is just 0.03 eV larger then experimental work function of 4.41 eV [51-52]. The LDA result for N_{Al}=6, N_V=8 is 4.46 eV. So far we employed Barth-Hedin (LDA-BH) parameterization of LDA functional. Our QSGW code uses LDA Hamiltonian for first GW iteration. I checked that using the Ceperly-Alder (LDA-CA) or LDA-BH for starting GW iteration does not affect the converged QSGW results, as it should be. The LDA-CA result for WF obtained by our LMTO code is 4.34

N_{Al}	N_V	nk	LDA WF (eV)	GW WF (eV)	CPU time (Days)
4	4	6	4.07	4.10	0.5
4	6	6	4.46	4.43	0.7
4	6	8	4.46	4.52	1.6
4	8	6	4.55	4.49	0.9
4	10	6	4.57	4.54	1.2
6	6	6	4.39	4.38	2
6	6	8	4.39	4.45	5.5
6	8	6	4.46	4.44	2.5
6	10	6	4.47	4.47	3
8	8	6	4.43	4.40	6
8	10	-	4.44	-	-

Table 5. Work function of Al (001), calculated in QSGW and LDA approaches as function of nk, NAl, and NV. Single processor CPU time per one GW iteration is also shown.

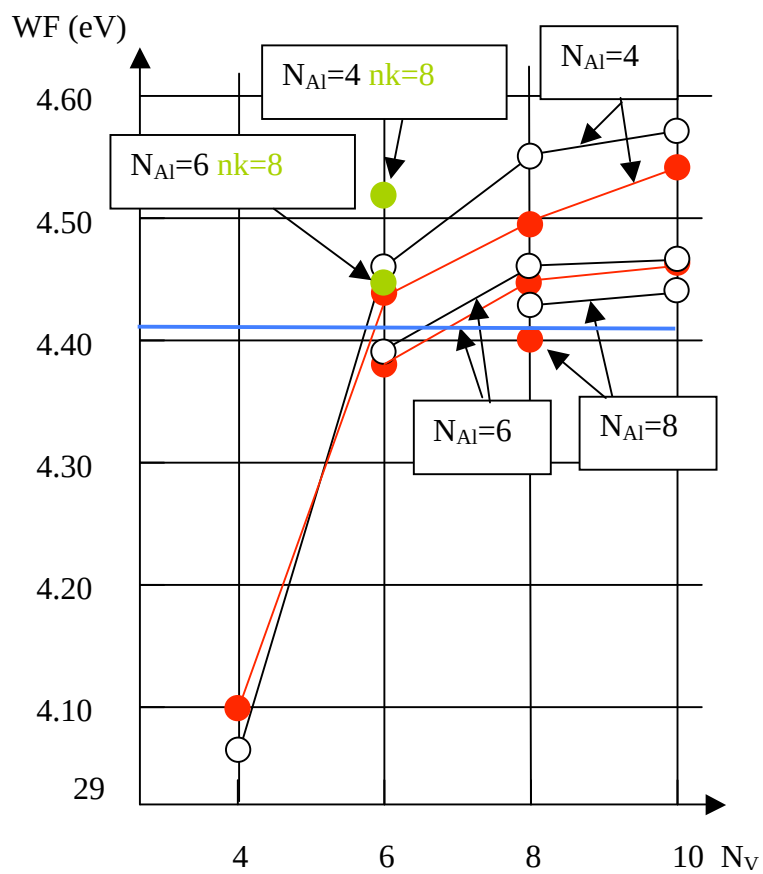

Figure 20. Graphical Graphical representation of Table I. LDA (empty circles) and QSGW (filled circles) results for work function of Al (001). All points obtained with nk=6 except green points (nk=8). Experimental WF

eV (N_{Al}=8, N_V=10) agrees with LDA-CA VASP calculations (see discussion below).

The Al (001) work function in LDA-CA and GGA-PBE by using VASP code [Appendix C]. Two Al layer from each of two surfaces to obtain equilibrium positions of Al atoms. The result of his calculations is shown in Table II.

Relaxed/Bulk	N_{Al}	N_V	WF (eV) LDA-CA	WF (eV) GGA-PBE
Bulk	8	10	4.34	4.18
Relaxed	8	10	4.34	4.25
Bulk	10	10	4.37	4.22
Relaxed	10	10	4.37	4.28

Table 6. VASP results of LDA-CA and GGA-PBE calculations of Al (001) work function**.**

We see that relaxation does not make any difference in LDA-CA, while the relaxed WF is 0.06 eV larger in GGA-PBE (in our GW calculations we use bulk, unrelaxed positions of Al). Converged results of LDA-BH – 4.46 eV, LDA-AC – 4.37 eV, and GGA-PBE – 4.22 eV show DFT uncertainty ~0.2 eV related to choice of functional. The GW result – 4.44 agree well with experiment and suggests that LDA-BH and LDA-CA functional are better for work function calculations as compared to GGW-PBE functional. Complete results are presented in a manuscript that will be submitted to Physical Review B, see appendix C.

Simulations of very high currents in pulsed-power conditions

To further understand and to quantify the behavior of materials exposed to high current densities, 2-D numerical simulations were performed with the ALEGRA code [53]. ALEGRA is an Arbitrary-Lagrangian-Eulerian (ALE) finite-element code that models dynamic mechanical response and shock propagation in a resistive magneto-hydrodynamic environment. The code includes thermal conduction and radiation physics and can be coupled to state of the art material models.

Material models

The success of this type of simulations is highly dependent on the material models employed. The Equation of States (EOS) of tungsten, copper and stainless-steel were the results of quantum molecular dynamics calculations, based on finite temperature density-functional theory (FT-DFT), which provided an accurate modeling of the warm dense matter regime that extend from near solid conditions into the vapor dome and temperatures up to several eV [54-57]. It is a solid-liquid-gas model. The material model for tungsten includes densities from $1.0\text{x}10^{-74}$ to 39.0 g/cc for temperatures extending from $1.16\text{x}10^{-6}$ to $1.18\text{x}10^{8}$ K. The EOS has a small tension region at temperatures below 447K and has solid-vapor and liquid-vapor coexistence at higher temperatures. The material model for copper includes densities from $1.0\text{x}10^{-20}$ to 50.0 g/cc for temperatures extending from $1.0\text{x}10^{-6}$ to $1.38\text{x}10^{8}$ K. Tension is included at temperatures below the triple point and above about 8.2 g/cc densities. The solid-gas equilibrium constructions are included for densities below 2 g/cc, between the triple point temperature and 150 K. The EOS for the tungsten alloy was calculated in a similar way, with a different treatment of tension. More details are included in reference 54 and 55. The EOS for stainless-steel The stainless-steel composition was 70% iron, 19% chromium and 11% nickel. The EOS used for aluminum was originally constructed in 1986 using the PANDA code [58] and agrees well with most experimental data. The material model includes densities from $1.0\text{x}10^{-9}$ to 50.0 g/cc for temperatures extending from 0.0 to $1.08\text{x}10^{5}$ K. It includes melting and vaporization. The EOS has a tension region at temperatures below 1500K and has a vapor-liquid coexistence region at higher temperatures. Behavior of vapor-liquid region above 4000K deviates significantly from usual picture – electronic terms predict existence of insulating liquid phase with density in between that of vapor and that of metallic liquid. The existence of this phase has not been verified experimentally, however.

The Steinberg-Guinan-Lund model was employed as yield model [59]. It predicts the viscoplastic response of various materials (principally metals) based on a consideration of thermally-activated dislocation mechanics. Finally, electrical and thermal conductivities were treated with the Lee-More-Desjarlais model [60,61], which are also the results of QMD calculations. The model includes the effects of magnetic fields and was previously used in accurate 3-D MHD simulations of a strip-line geometry [62].

Simulation Configuration

To better understand the material response to high current densities, simulations were performed where current was applied to a cylindrical electrode made of several materials: tungsten, stainless steel, copper, aluminum as well as a tungsten alloy. The setup is shown in Figure 21. The current conditions were similar to that of the Z machine: the current risetime was about 100 ns. The peak current varied from 25 MA which is the present current condition for Z.to 125 MA. For the simulation configuration, this corresponds to current densities varying from 5 MA/cm to 25

MA/cm. The numerical simulations were conducted using a 2-D cylindrical Eulerian grid with a spatial resolution up to 2 μm. Actually, the simulations were driven with a source voltage and the equivalent circuit of the Z machine so that the load inductance, which increases with time, and the resulting effective current is automatically calculated.

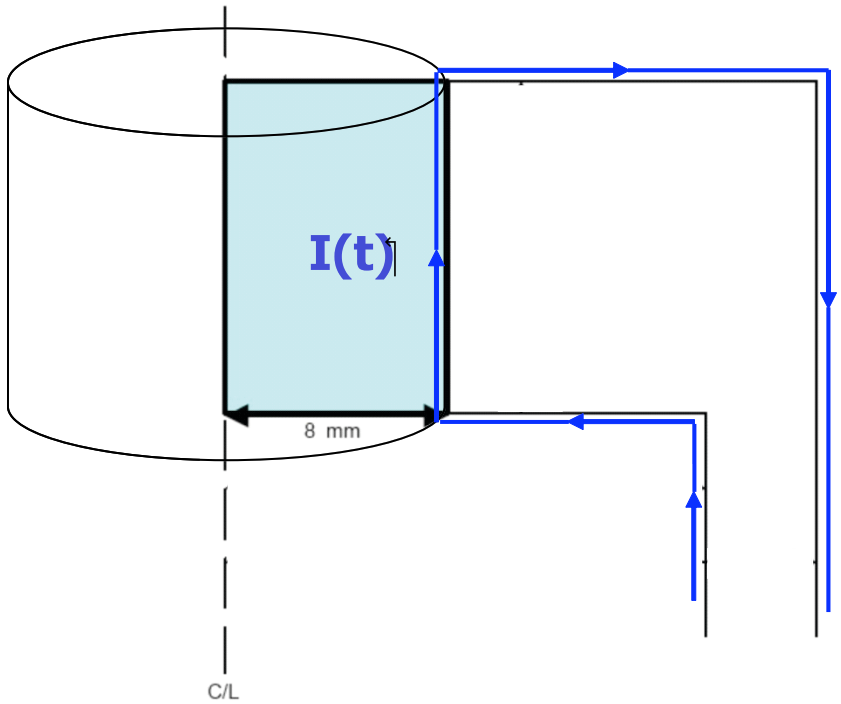

Figure 21: Simulation setup of a cylindrical conductor.

Simulation results and analysis

To evaluate the response of materials when different current are applied to them, a number of parameters such as density, temperature or stress were evaluated along the radius of the cylinder, at different times during the rise time. Figure 22 shows a typical current waveform and the times at which parameters were estimated.

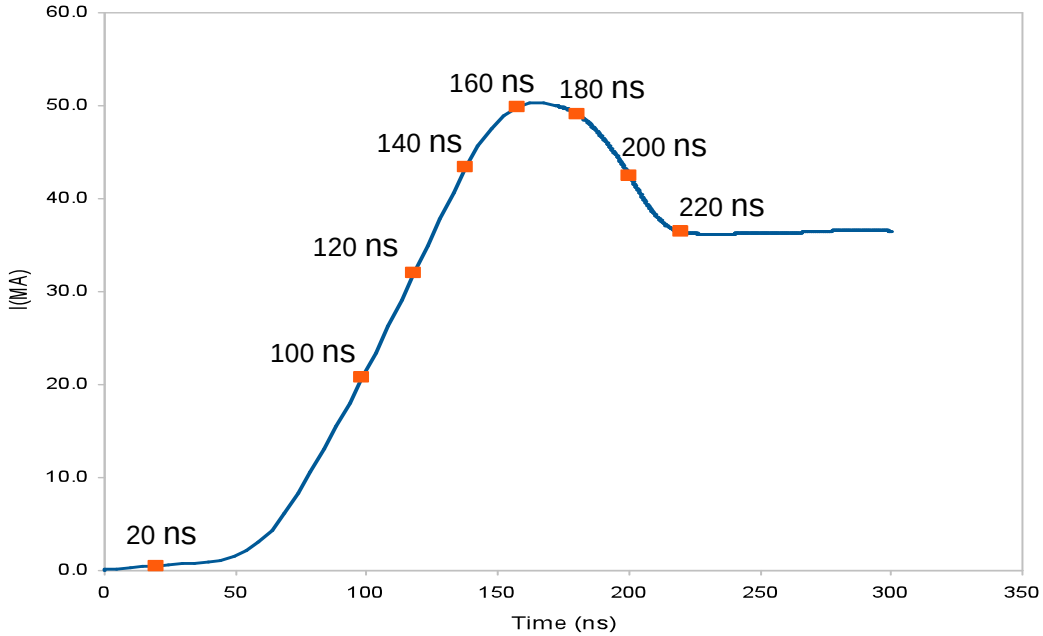

Figure 22: Typical Current waveform.

Figure 23 shows the density along the radius for different materials and at different times during the current pulse. The peak drive current density was 10 MA/cm, or about twice the maximum current available at Z. For tungsten, the heaviest material, the density increased by 80 %, while in the case of aluminum, the maximum density was almost 3 times its initial density. The density profile along the radius for the tungsten alloy is very similar to that of pure tungsten. At 220 ns, the 8mm radius of the aluminum cylinder was reduced to 7 mm; the tungsten cylinder radius was only decreased to 7.6 mm. The smaller diameter of the cylinder has the effect of increasing the inductance of the load, reducing the effective current in the system. Figure 24 shows the temperature along the radius for different materials in the same drive conditions as Figure 22. For all materials, the temperature is very high at the surface of the conductor where most of the current lies, due to Joule heating. However, as it was the case for the density, the temperature effects are much more significant in low z materials: in copper, stainless-steel and aluminum, the temperature profile at 220 ns shows the presence of a shock propagating toward the center axis. The shock is stronger in aluminum than in copper or stainless-steel. At 220 ns into the pulse, the shock front is already at 6 mm from the center in the aluminum cylinder, while it is still at about 6.75 mm in the stainless-steel and copper cylinders. One should note that the aluminum peak temperature at 140 ns and above is “clipped” as the current conditions become too extreme for this material and the temperature has reached the maximum temperature of the EOS table. The current density along the radius for different materials, as a function of time is also interesting to examine. It is presented in Figure 25 and was calculated in the same conditions as in Figure 22. The current density profile shows a peak away from the surface of the cylinder in pure materials and this effect increases with time. For the tungsten alloy and stainless-steel, the current density profile is more evenly distributed, reducing the peak current density reached at the same time in the current pulse and the potential damage that could be caused by very high local current.

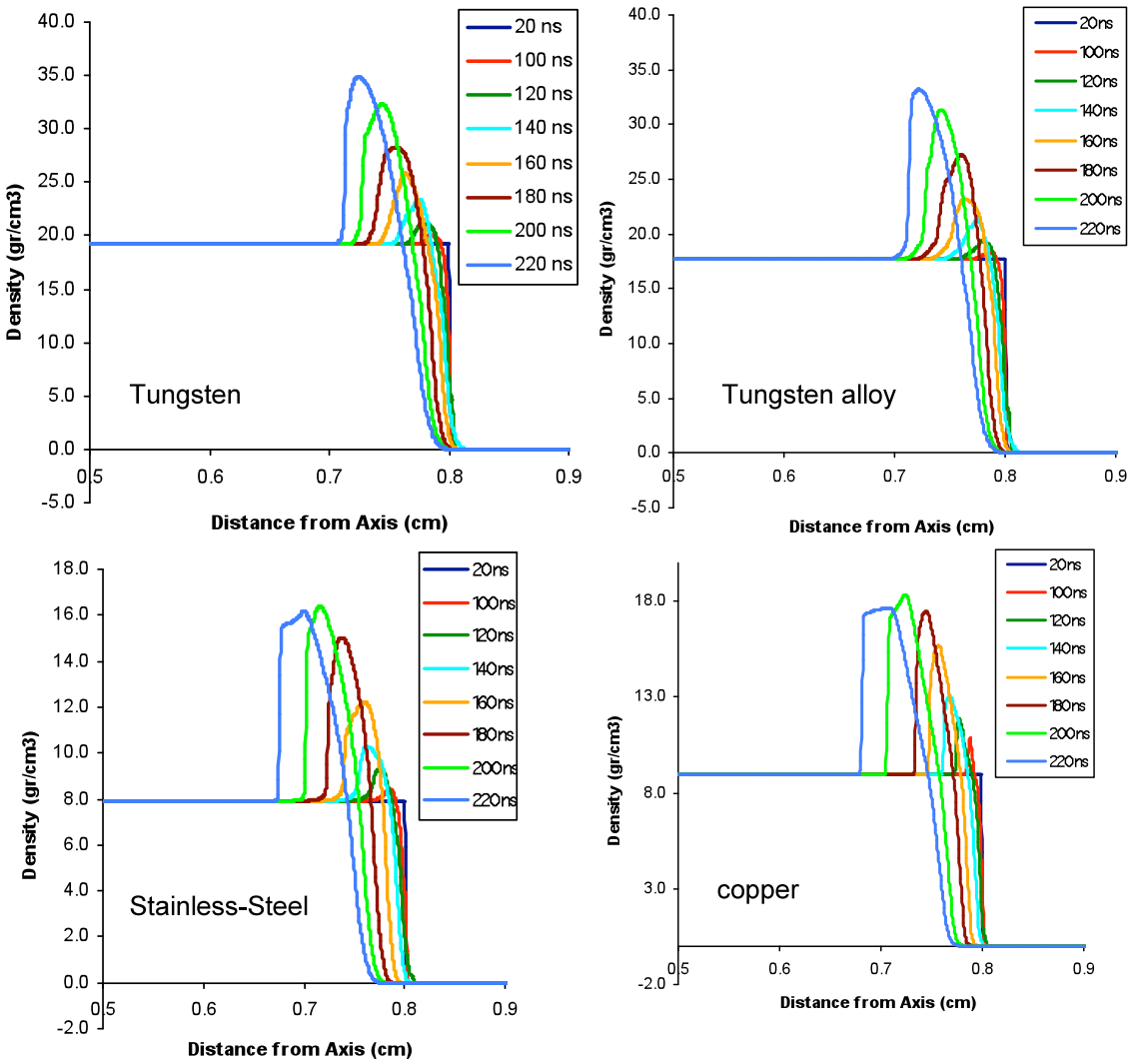

Figure 23: Density along the radius for different materials and at different times during the risetime (10 MA peak current density).

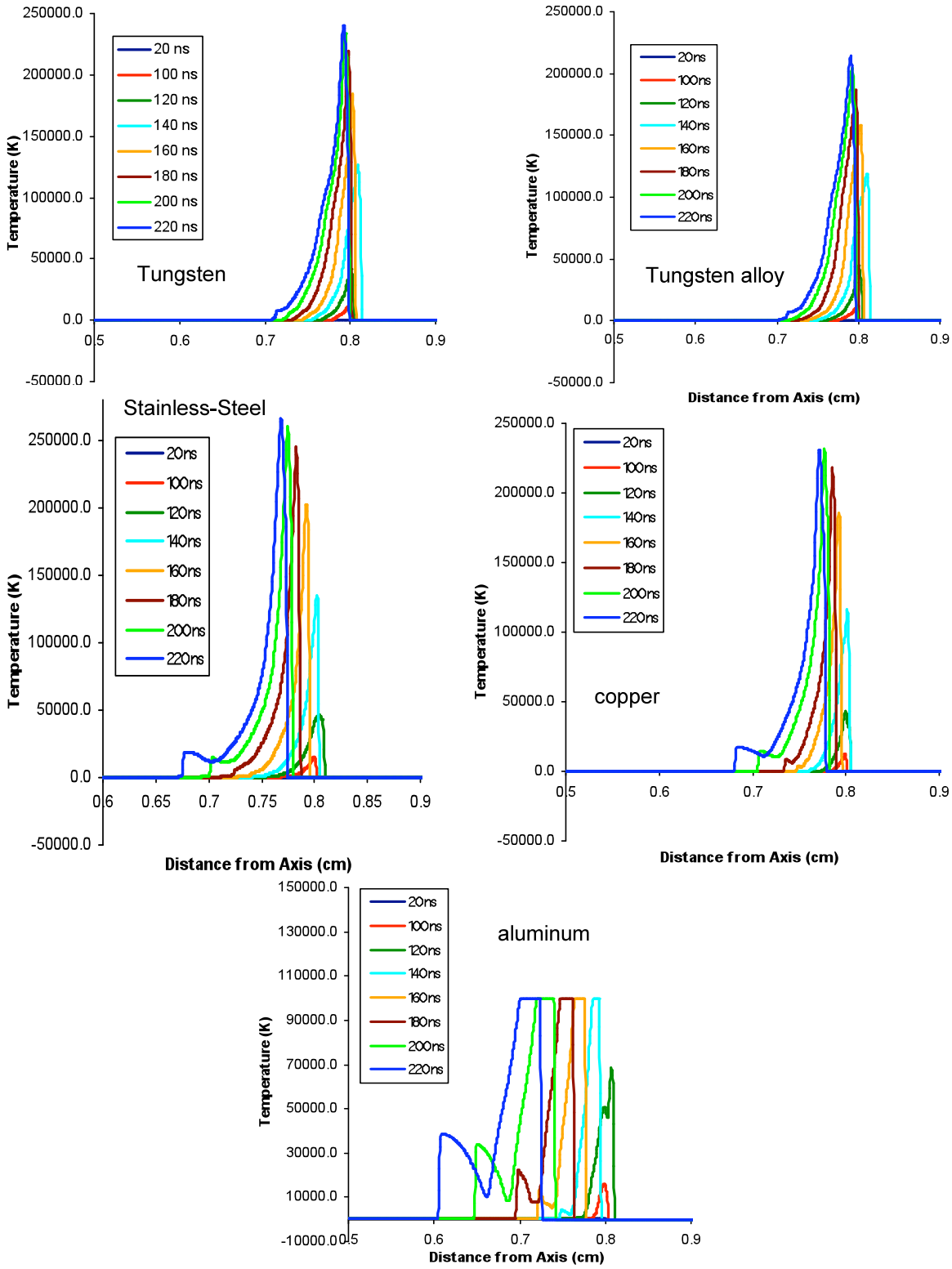

Figure 24: Temperature as a function of radial position for different materials at different times during the current risetime (10 MA peak current density).

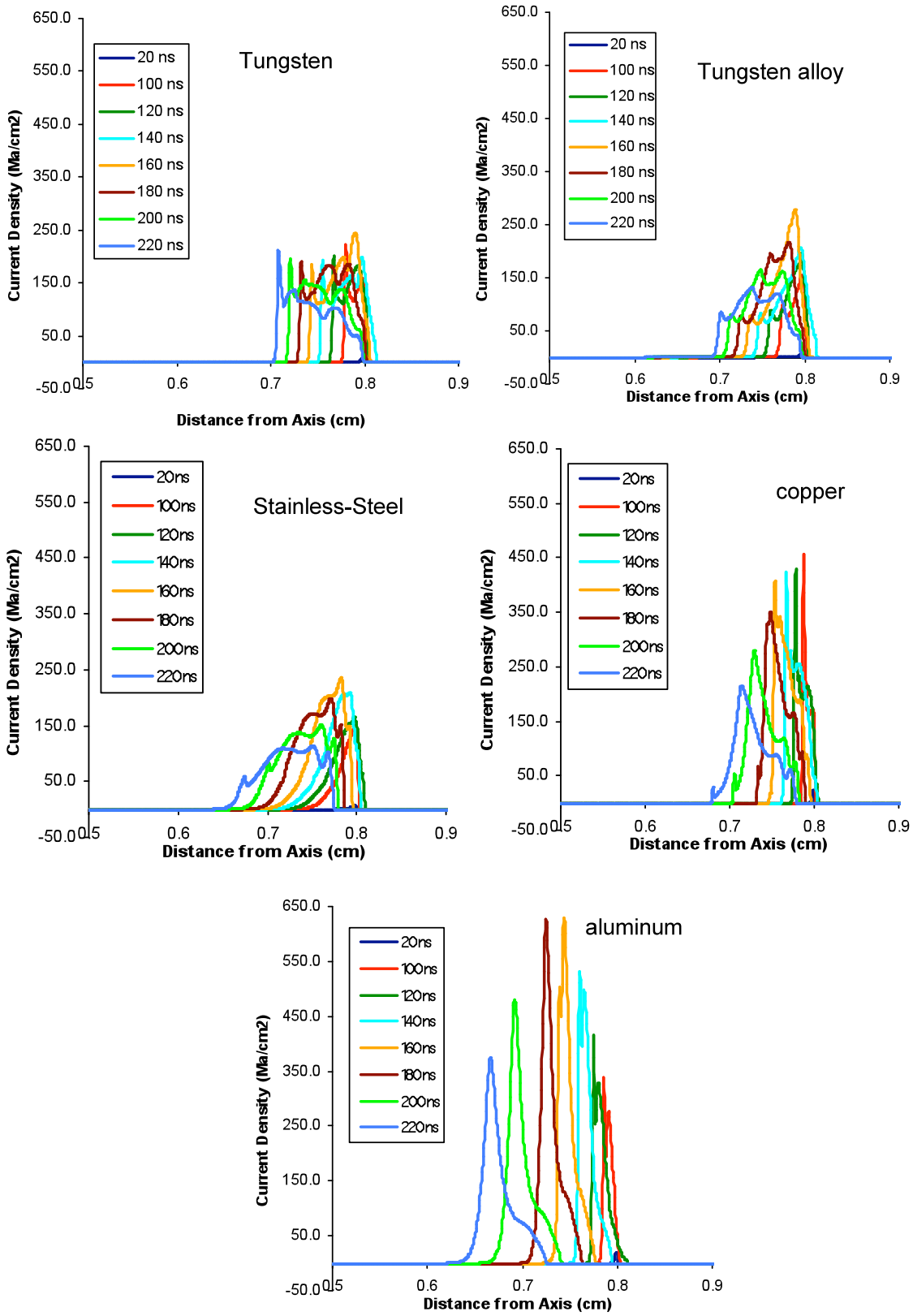

Figure 25: Current density as a function of radial position for different materials at different times during the current risetime (10 MA peak current density).

densities. Figure 25 also shows that the current migrates into the conductor, due to magnetic diffusion. The motion of the current toward the center of the cylinder causes the inductance to increase, which results in a reduced effective current in the load. As an example, Figure 27 shows the inductance of the load as a function of time for tungsten and aluminum electrodes, as well as the corresponding drive current.

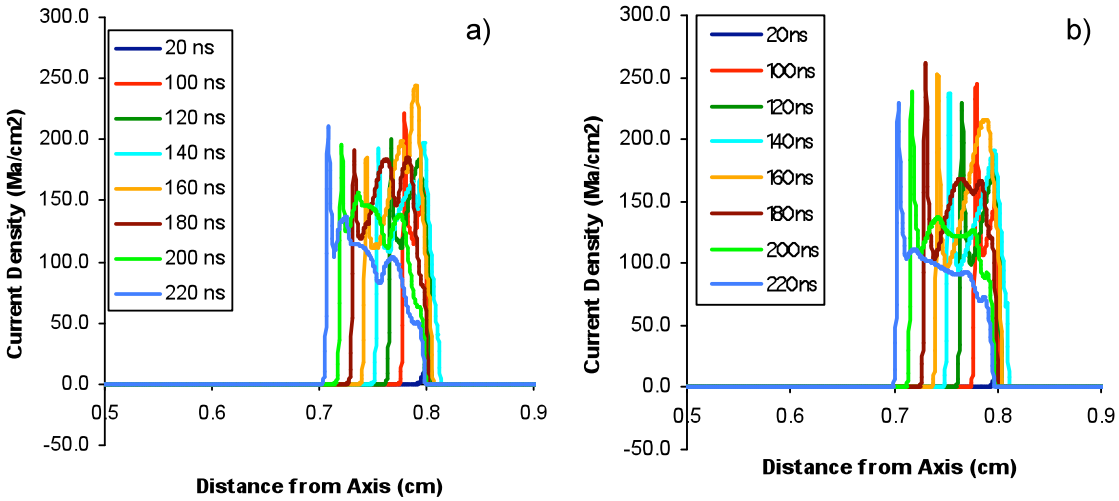

Figure 26: Comparison of the Current density profile calculated with two different EOS models: a) the FT-DFT calculations (ref. 6,7) , b) the standard Sesame model (ref. 15)

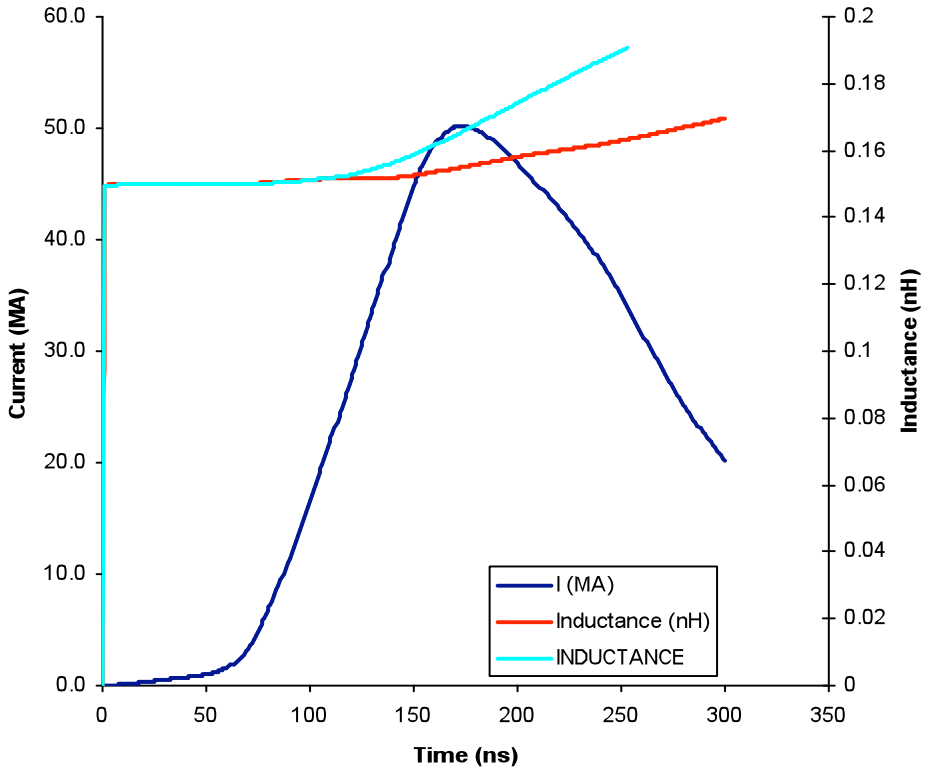

Figure 27. Current in the load and inductance of aluminum and tungsten cylinders.

In addition, Figure 26 illustrates the importance of the material models used in these calculations: on the left side, the current density profile for tungsten was calculated with the new FT-DFT based model described in reference 54 and 55. On the right side, the standard Sesame table was used [63]. The new model results in lower peak densities overall and in slightly lower average density.

To obtain a quantitative evaluation of the effects of high current densities on different materials for different current conditions, the current loss was estimated by calculating the inductance at peak current. The results are shown in Figure 28. The fraction of current loss is recorded as a function of the peak current density: the fraction of current loss increases much faster and almost linearly with the peak current amplitude for low z materials. Alloys (mixed materials) and pure materials show comparable current losses for equivalent z.

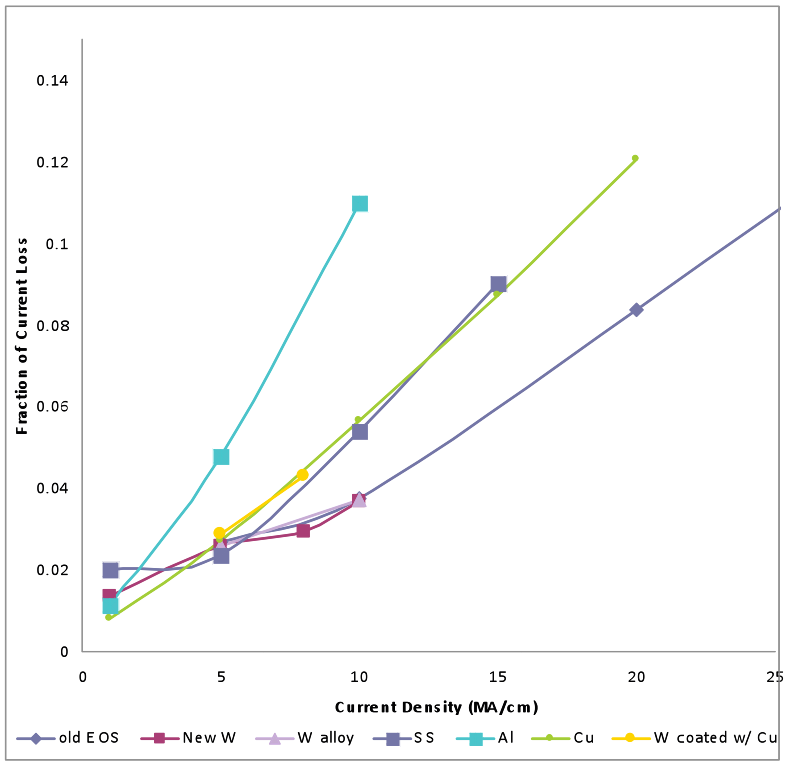

Figure 28: Fraction of current loss at peak current in different materials for different peak current densities. Al has a small loss for low current density, but an increasing loss at higher currents. Tungsten and stainless steel are improvements at higher currents albeit displaying larger loss at low currents.

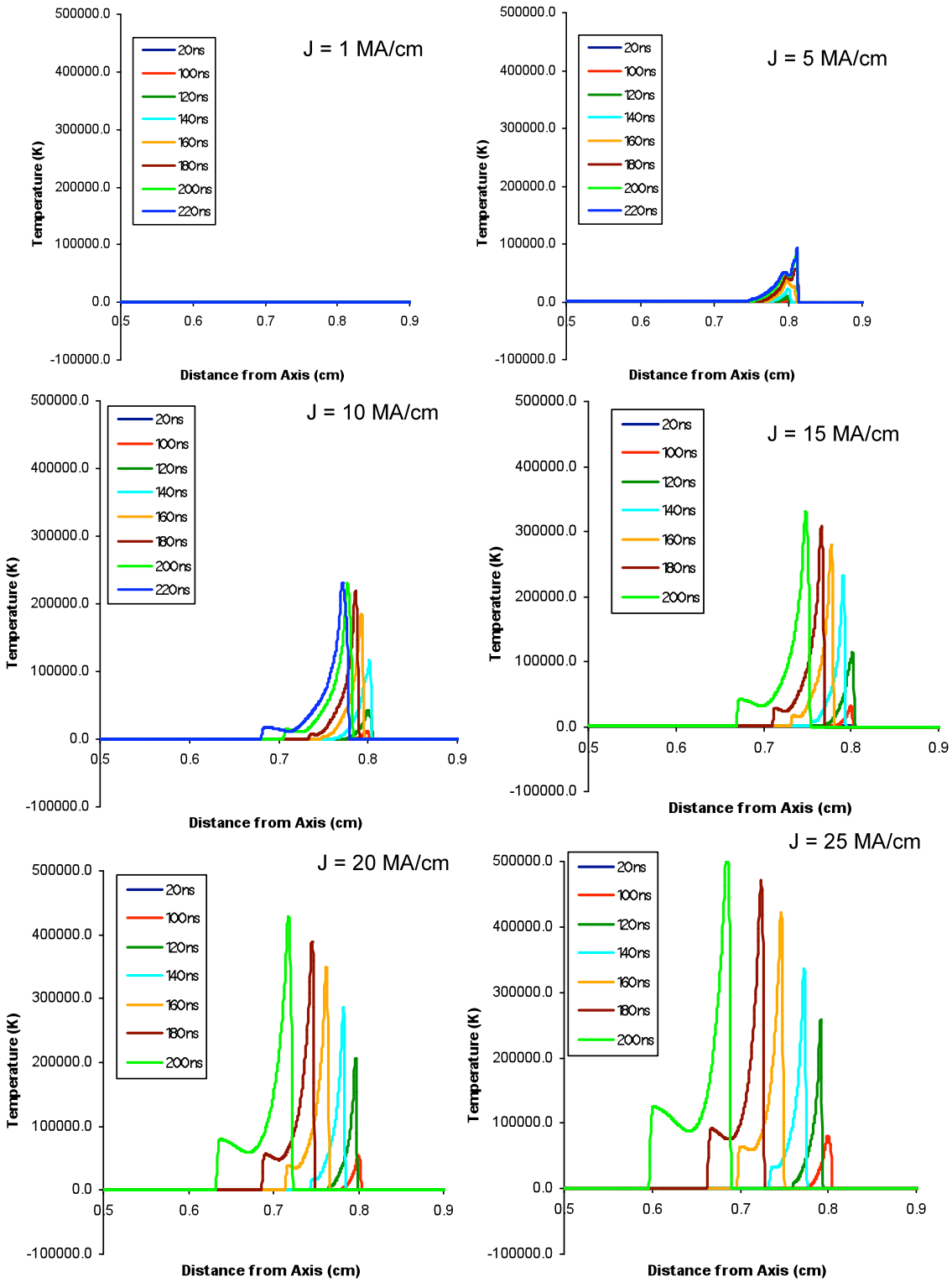

Figure 29: Temperature along the radius for Cu, for different peak currents and at different times during the current risetime.

Figure 29 shows the temperature profiles along the radius, for copper material, for peak current densities varying from 1 MA/cm to 25 MA/cm. At low current, joule heating is the primary

mechanism that will cause the temperature to increase. For high peak currents, the energy loss due to the temperature rise is mainly the result of shock formation and propagation through the material.

Copper coated tungsten electrode

In a number of experiments at z, the stainless steel load was coated with gold. Performance was not increased, although the experimental conditions were generally improved [64]. Multi-material electrodes seem to reduce the maximum local current density without affecting the performance. We by coating the best material (tungsten) with layers containing sequentially more copper, one might be able to slow down the propagation of the shock through the electrode. Such electrodes were prepared at the Thermal Spray Research Laboratory (TSRL) at Sandia National Laboratories and the process is described in the next section. In the simulation, a cylinder with a radius of 6.68 mm is coated with 10 layers of a tungsten-copper mixture, where 10% additional copper is added at each level. Figure 30 for illustration show a similar sample where copper and aluminum was cold-sprayed in a graded fashion.

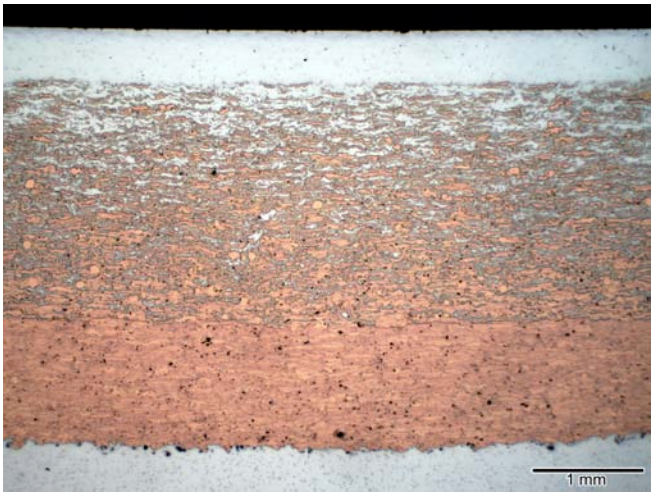

Figure 30. Graded density sample, copper to aluminum showing the texture of the graded density region.

To reproduce the experimental conditions, an initial density profile shown in Figure 31 was created using the image data in Figure 30. The pixel size of data was 2.94 μm. However, the simulation resolution was limited to 10 μm because of the numerical difficulties that occur in calculations involving very high currents and the limited time to accomplish the project.

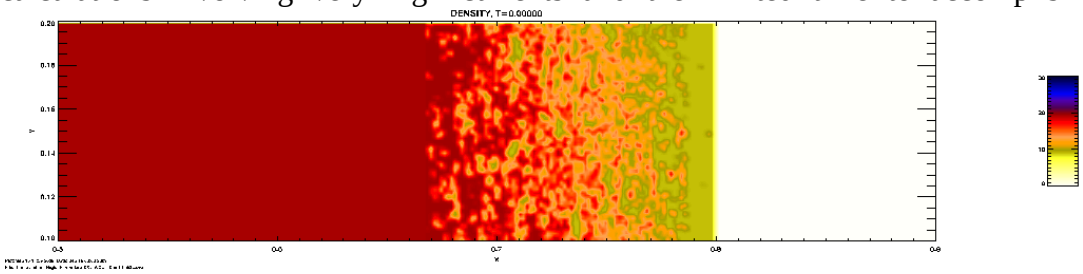

Figure 31: Copper coated tungsten initial density profile.

The results of the simulations for a peak current density drive of 5 MA/cm are compared to those of pure tungsten in Figure 34: the current density in the coated material seems to stay closer to the surface, and the temperature rise is not as significant as in pure tungsten. The same effect was seen in alloys versus pure materials in the previous section. Also, the resulting material at the surface has a lower z than tungsten. However, the loss of current at peak current is similar to that of copper and higher than for tungsten (see Figure 28). The highest current density drive that could be used for these calculations is 8 MA/cm. In that case, the temperature rises to extremely high temperatures at the surface of the cylinder, causing the thermal conductivity solver to fail

just below peak current. Since Alegra results were never compared to experimental data in that regime and limited time was available to analyze the data, these results are not reported here.

Conclusions and recommendations

Among all the materials investigated, mixed materials are the most promising at sustaining high current density conditions. Their properties are similar to that of pure materials at equivalent atomic number. The current density is more uniformly distributed in mixed material, reducing local high current densities. Higher z materials are capable of carrying on higher current densities and tungsten is a good material choice for a linear current density drive of 10 MA/cm or higher. The preliminary results obtained for copper coated tungsten are interesting and suggest performing a more detailed analysis in the future.

Manufacturing of a graded-density conductor

A conclusion from the simulations is that a heavy material, steel or tungsten, is beneficial due to its higher shock impedance. The conductor is less affected by the strong shock at the surface. With that principle, we designed a conductor with a Ta core and a Cu plating, but in order to increase homogeneity of the conductor, and improve thermal expansion properties, it was made as a graded density material. The thermal spray-lab did the design and manufacturing of the part. Plasma Spray devices, used for preparing coatings, are specifically designed to deliver a well controlled flow of 1 – 100 micron diameter feed stock particles into a steady state plasma. The plasma torch heats and accelerates feed stock particles that form a coating upon impact with a substrate. Upon impact, the particle is fused onto the substrate, by changing the composition of the powder mixture it is possible to move continuously between two materials, in our case from heavy Ta to highly conductive Cu.

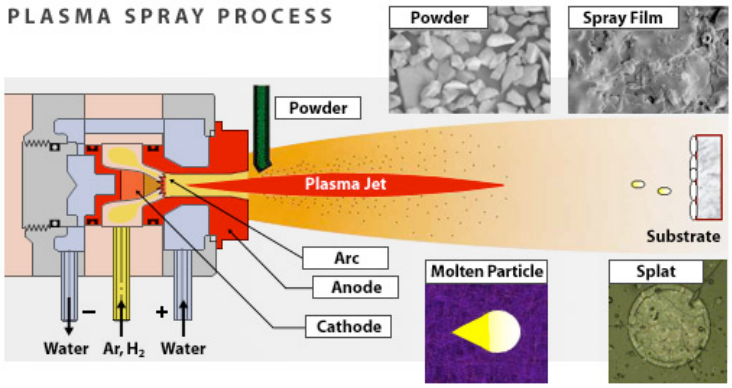

Figure 32. Illustration of the plasma-spray process: a powder is fed into the plasma torch and accelerated while heated to close or beyond the melting point. By changing the powder make-up, the composition of the surface coating can be tailored precisely, for example be graded.

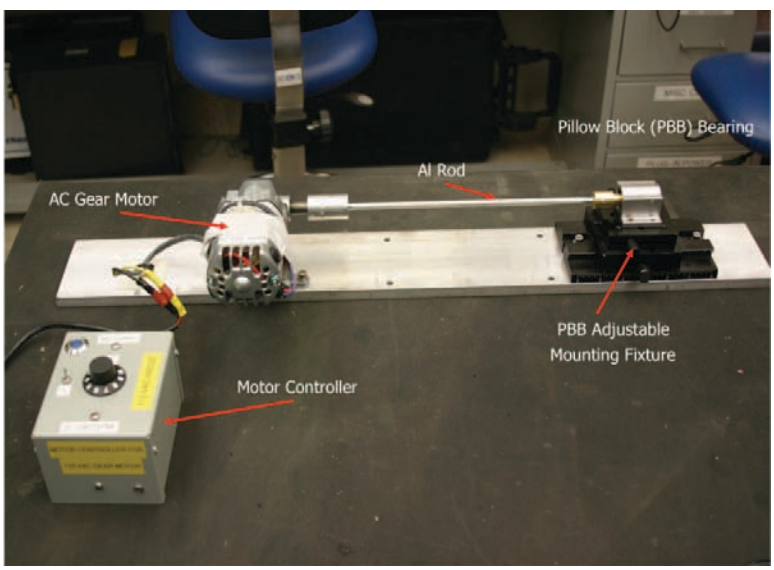

Figure 33. Rotation assembly for cold spray coating of Tantalum bar stock. The rotation rate is adjustable from 0 to 100 RPM.

For the high-current conductor application, we moved from Ta to Cu in 10 composition steps in both a cylindrical and planar geometry. The cylindrical prototype was built using a rotation assembly. A Ta bar was placed in the assembly, followed by cold spray of Ta/TaCu/Cu. The planar samples were made starting from Ta plates that were cold-sprayed Ta/TaCu/Cu. In all, we have one cylindrical sample and a number of plates. The cylindrical sample can be cut into several short conductors, for performing multiple high-current experiments and comparing to the predictions from simulations in the previous section. For high-precision studies of the shocked properties of the graded samples, the plates can be used in combination with high precision VISAR probes to measure the dynamic response of the graded material. The gradual density is likely to delay onset of shocks, a phenomenon that could prove beneficial for high-current conductors.

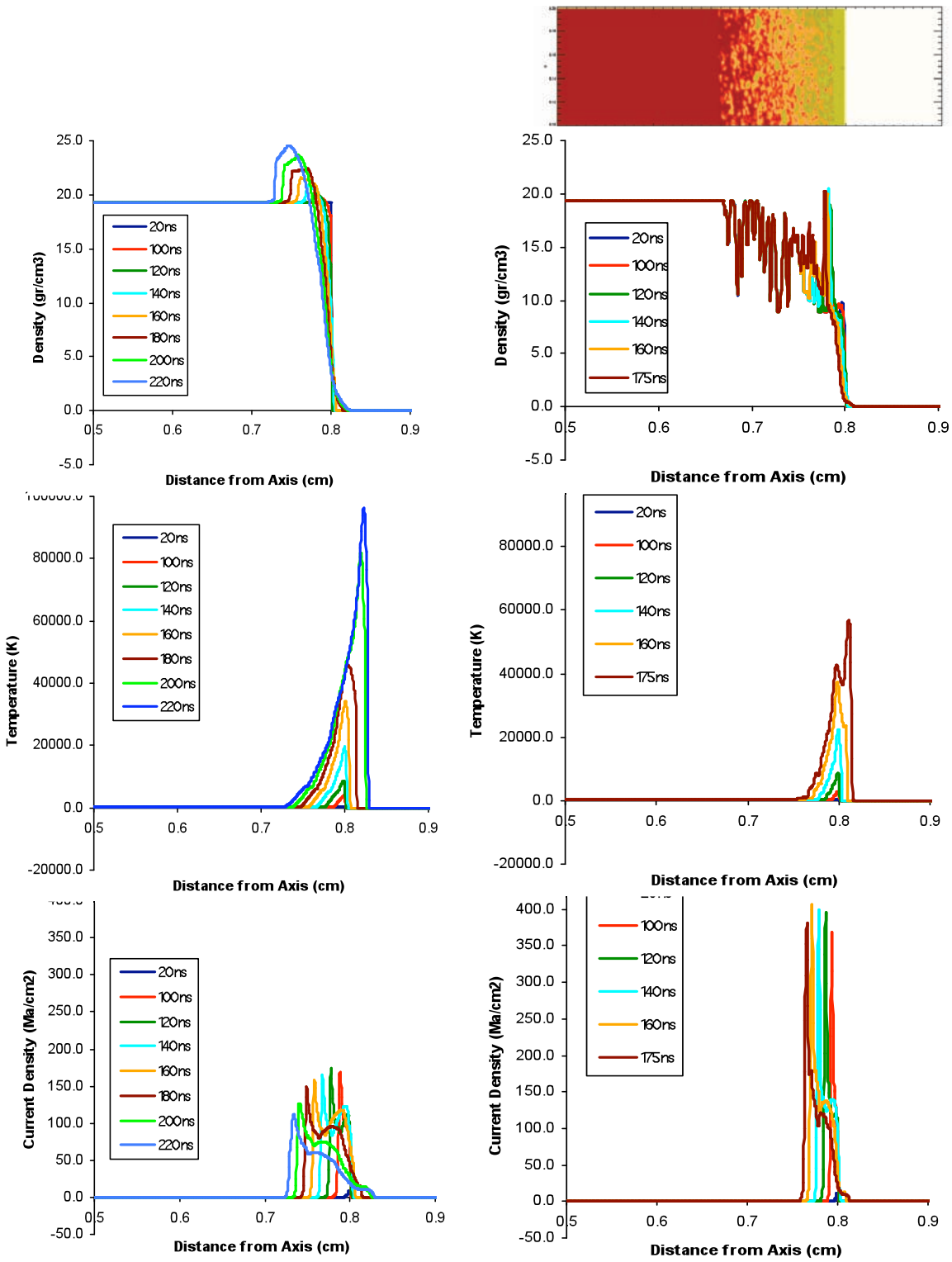

Figure 34: Properties of tungsten and copper coated tungsten for a 5 MA/cm peak current density.

SUMMARY OF RESULTS

The project had three major parts: calculation of work functions with increasing complexity, simulations of surface emission, and finally the surface-and near-bulk effect of high current density, including a pilot manufacturing of a graded density conductor.

The initial work function calculations of metals, different kinds of metal/oxide interfaces, and oxides using DFT followed by work function calculations of metals by developing and applying QSGW.

Electron scattering was calculated fully within DFT, the electron loss function was calculated using dielectric functions from DFT/Kubo-Greenwood. Furthermore, a Monte-Carlo scattering code was written to simulate electron transport in the surface region.

In the high-current effects part of the project, the focus of the third year, we performed simulations of the high-current response of different materials, as well as a graded density conductor. We also made a pilot study of manufacturing a graded density high-current conductor. The conductor is a Ta core, graded to pure Cu within skin depth of a 100 ns pulse.

ACKNOWLEDGMENTS

Tom Mehlhorn is gratefully acknowledged for lasting support of work on fundamental and applied work on advanced materials modeling.

We have benefited greatly from discussions with Michael Desjarlais as well as from using his Kubo-Greenwood code and Mathematica notebooks for post-processing of VASP calculations.

We thank Ann Mattsson for discussions regarding the fundamentals of DFT and Larry Warne for discussions on electrical break down in gas switches.

We also thank Steve Rosenthal for generously sharing unpublished results and for detailed discussions regarding rad-MHD simulations of high-current conductors using ALEGRA and MACH 2.

Paul Kent and Dennis Dinge were instrumental in porting VASP 5.1 on Red Storm and we thank Georg Kresse for the early opportunity to employ VASP 5.1. We thank the SNL high performance computing staff in general and Sophia Corwell in particular for rapid and efficient troubleshooting on the capacity clusters.

The project was made possible by an LDRD in the Science of Extreme Environments Investment Area at Sandia National Laboratories.

REFERENCES

1. E.A. Weinbrecht, D.H. McDaniel, and D.D. Bloomquist, Proc. Of the 14th IEEE International Pulsed Power Conference, Dallas, TX, p.157 (2003).
2. S. Singer & R.O. Hunter, Proc. Of the 3rd IEEE Int. Pulsed Power Conf., Albuquerque, NM, P 351 (1981).
3. H. Knoepfel, "Pulsed High Magnetic Fields," North Holland Publishing Company, 1970.
4. R.B. Spielman, S. Chantrenne, and D.H. McDaniel, Proc. Of the 16th IEEE International Pulsed Power Conference, Albuquerque, New Mexico (2007).
5. P. Hohenberg and W. Kohn, Phys. Rev. **136**, B864 (1964).
6. W. Kohn and L. J. Sham, Phys. Rev. **140**, A1133 (1965).
7. http://nobelprize.org/nobel_prizes/chemistry/laureates/1998/kohn-lecture.html; Nobel Lectures in Chemistry 1996-2000, edited by Ingmar Grethe, World Scientific (2000).
8. A. E. Mattsson et al., Model. Simul. Mater. Sci. Eng. **13**, R 1 (2005).
9. A. D. Becke, Phys. Rev. A **38**, 3098 (1988); C. Lee, W. Yang, and R. G. Parr, Phys. Rev. B **37**, 785 (1988).
10. J. P. Perdew and Y. Wang, Phys. Rev. B **45**, 13244 (1992).
11. J. P. Perdew, K. Burke, and M. Ernzerhof, Phys. Rev. Lett. **77**, 3865 (1996).
12. B. Hammer, L. B. Hansen, and J. K. Nørskov, Phys. Rev. B **59**, 7413 (1999).
13. A. E. Mattsson, R. Armiento, P. A. Schultz, and T. R. Mattsson, Phys. Rev. B **73**, 195123 (2006).
14. W. Kohn and A. E. Mattsson, Phys. Rev. Lett. **81**, 3487 (1998);
15. A. E. Mattsson and W. Kohn, J. Chem. Phys. **115**, 3441 (2001).
16. R. Armiento and A. E. Mattsson, Phys. Rev. B **66**, 165117 (2002).
17. P. E. Blochl, Phys. Rev. B **50**, 17953 (1994); G. Kresse and D. Joubert, Phys. Rev. B **59**, 1758 (1999).
18. G. Kresse and J. Hafner, Phys. Rev. B **47**, R558 (1993); G. Kresse and J. Hafner, Phys. Rev. B **49**, 14251 (1994); G. Kresse and J. Furthmuller, Phys. Rev. B **54**, 11169 (1996).
19. Ann E. Mattsson et al., J. Chem. Phys. **128**, 084714 (2008).
20. Paier et al. J. Chem. Phys. **124**, 154709 (2006); **125**, 249901 (2006).
21. M. P. Desjarlais, J. D. Kress, and L. A. Collins, Phys. Rev. E **66**, 025401(R) (2002).
22. Strayer et. al, Surface Science **34**, 225 (1973).
23. Jennison et. al. Surface Science **549**, 115 (2004).
24. Session J20.08, APS March meeting, New Orleans, LA (2008).
25. C. Ruberto, Y. Yourdshahyan, and B.I. Lundqvist, Phys. Rev. B **67**, 195412 (2003).
26. P. R. C. Kent, J. Phys.: Conf. Ser. **125**, 012058 (2008).
27. http://www.wolfram.com/
28. B. Ollivier, R. Retoux, P. Lacorre, D. Massiot, and G.Ferey, J. Mater. Chem **7**, 1049 (1997).
29. Y. Yourdshahyan C. Ruberto, L. Bengtsson, and B.I. Lundqvist, Phys. Rev. B **56**, 8553 (1997).
30. "Solid state physics", N.W. Ashcroft and N.D. Mermin, HRW international (1988).
31. D.R. Penn, Phys. Rev. B **35**, 482 (1987)
32. Z.J. Ding et al. Applied Physics A **78**, 585 (2004).
33. N. Fitzer, et al, Phys. Rev. B **67**, 201201 (2003).
34. R. H. French, J. Am. Ceram. Soc. **73**, 477 (1990)

35. Y. Xu and W. Y. Ching, Phys. Rev B **43**, 4461 (1991)
36. W. Y. Ching and Yong-Nian Xu, J. Am. Ceram. Soc. **72**, 404 (1994)
37. B. Holm, R. Ahuja, Y. Yourdshahyan, B. Johansson, and B. I. Lundqvist, Phys. Rev. B **59**, 12777 (1999)
38. Shang-Di Mo, W. Y. Ching, Phys. Rev. B **57**, 15219 (1998)
39. I. Barta, J. Phys. C **15**, 1599 (1982)
40. S. Ciraci and I. P. Barta, Phys. Rev. B **28**, 982 (1983)
41. A. Balzarotti and A. Bianconi, Phys. Status Solidi B **76**, 689 (1976)
42. S. V. Faleev, M van Schilfgaarde, and T. Kotani, Phys. Rev. Lett. **93**, 126406 (2004)
43. M van Schilfgaarde, T. Kotani, and S. V. Faleev, Phys. Rev. Lett. **96**, 226402 (2006)
44. T. Kotani, M van Schilfgaarde, and S. V. Faleev, Phys. Rev. B **76**, 165106 (2007)
45. P. Villars and L.D. Calvert, *Pearson's Handbook of Crystallographic Data for Intermetallic Phases*, 2nd Edition (ASM International, Materials Park, Ohio, 1991).
46. G. Drager and J. A. Leiro, Phys. Rev. B **41**, 122919 (1990)
47. E. T. Arakawa and M. W. Williams, J. Phys. Chem. Solids **29**, 735 (1968)
48. L. X. Benedict, E. Shirley, and R. B. Bohn, Phys. Rev. Lett. **80**, 4514 (1998)
49. E. D. Palik, *Handbook of Optical Constants of Solids* (Academic Press, Orlando, 1985); *Handbook of Optical Constants of Solids II* (Academic Press Boston, 1991); D. M. Roessler and W. C. Walker, J. Opt. Soc. Am. **57**, 835 (1967)
50. M. van Schilfgaarde, T. Kotani, and S. V. Faleev, Phys. Rev. B **74**, 245125 (2006)
51. J. K. Grepstad, P. O. Gartland, and B. J. Slagsvold, Surf. Sci. **57**, 348 (1976)
52. J. J. Paggel, C. M. Wei, M. Y. Chou, D.-A. Luh, T. Miller, T.-C. Chiang, Phys. Rev. B **66**, 233403 (2002).
53. S.K. Carroll, R.R. Drake, D.M. Hensinger, C.B. Luchini, S.V. Petney, J. Robbins, A.C. Robinson, R.M. Summers, T.E. Voth, M.K. Wong, T.A. Brunner, C.J. Garasi, T.A. Haill, and T.A. Mehlhorn, Technical report SAND2004-6541, Sandia National Laboratories, Albuquerque, NM, January 2005.
54. M.P. Desjarlais, J.H. Carpenter, A.E. Mattsson, and K.R. Cochrane, "A new wide-range equation of state for tungsten, with higher accuracy for warm dense matter," Sandia report SAND2007-6057, (2007)
55. J.H. Carpenter, "Improvement to the tungsten equation of state described in report SAND2007-6057," Sandia National Laboratories report, SAND2007-6907, (2007)
56. J.H. Carpenter, at al, Sandia report , to be published in 2009
57. T.R. Mattsson and M.P. Desjarlais, SAND2004-5253 (2004).
58. G.I. Kerley, "Theoretical equation of State for Aluminum," Int.J. Impact Eng. 5, 441-449 (1987)
59. P.A. Taylor, the Steinberg-Guinan-Lund viscoplastic model. SAND92-0716, Sandia National Laboratories, Albuquerque, NM, 1992.
60. M.P. Desjarlais, Contrib. Plasma Phys. **41**, 267 (2001).
61. M.P. Desjarlais, J.D. Kress, and L.A. Collins, Phys. Rev. E **66**, 025401(R) (2002).
62. T. Ao, J.R. Asay, S. Chantrenne, M.R. Baer, & C.A. Hall, Rev. Sci. Instrum. **79**, 013903 (2008)
63. EOS mat # 3541, Sesame LANL, 1979. Ref.: K.S. Holian, "T-4 Handbook of material Properties Data Bases," Los Alamos National Laboratory, report LA-10160-MS, 1984
64. M. E. Cuneo et al., IEEE Trans. On Plasma Science, Vol. **25**, No. 2, Appril 1997; M.E. Cuneo, IEEE trans on Dielectrics and Electrical Insulation, Vol. **6** No. 4, August 1999.

APPENDIX A – AM05 FOR SOLIDS, JOURNAL OF CHEMICAL PHYSICS 2008.

The AM05 Density Functional Applied to Solids
A.E. Mattsson, R. Armiento, J.Paier, G. Kresse, J. Wills, and T.R. Mattsson
Journal of Chemical Physics, **128**, 084714 (2008).

The AM05 density functional applied to solids

Ann E. Mattsson,[1,a)] Rickard Armiento,[2,b)] Joachim Paier,[3,c)] Georg Kresse,[3,d)] John M. Wills,[4,e)] and Thomas R. Mattsson[5,f)]
[1]*Multiscale Dynamic Materials Modeling MS 1322, Sandia National Laboratories, Albuquerque, New Mexico 87185-1322, USA*
[2]*Physics Institute, University of Bayreuth, D-95440 Bayreuth, Germany*
[3]*Faculty of Physics and Center for Computational Materials Science, University of Vienna, Sensengasse 8/12, A-1090 Vienna, Austria*
[4]*Los Alamos National Laboratory, Los Alamos, New Mexico 87545, USA*
[5]*High Energy Density Physics Theory, MS 1186, Sandia National Laboratories, Albuquerque, New Mexico 87185-1186, USA*

(Received 19 October 2007; accepted 17 December 2007; published online 29 February 2008)

We show that the AM05 functional [Armiento and Mattsson, Phys. Rev. B **72**, 085108 (2005)] has the same excellent performance for solids as the hybrid density functionals tested in Paier *et al.* [J. Chem. Phys. **124**, 154709 (2006); **125**, 249901 (2006)]. This confirms the original finding that AM05 performs exceptionally well for solids and surfaces. Hartree–Fock hybrid calculations are typically an order of magnitude slower than local or semilocal density functionals such as AM05, which is of a regular semilocal generalized gradient approximation form. The performance of AM05 is on average found to be superior to selecting the best of local density approximation and PBE for each solid. By comparing data from several different electronic-structure codes, we have determined that the numerical errors in this study are equal to or smaller than the corresponding experimental uncertainties. © *2008 American Institute of Physics*. [DOI: 10.1063/1.2835596]

I. INTRODUCTION

Density functional theory[1,2] (DFT) has become the foundation of most large-scale quantum mechanical simulations. The success stems from the theory's good quantitative results for a broad range of systems in combination with its relatively low computational cost. At the core of every Kohn–Sham DFT calculation lies the exchange-correlation (XC) functional. It is, in principle, the only limiting factor for the accuracy of the calculations.[63] The development of new functionals is, therefore, of utmost importance to the progress of computational materials science, -physics, -chemistry, and -biology. Despite the importance, significant improvements of the exchange and correlation treatment have been few. Since DFT is increasingly being employed for large systems (several hundred atoms) and for long (tens of picoseconds) molecular dynamics (MD) simulations, the trade-off between speed and accuracy is arising as an additional major concern in functional development.

In this article, we assess the performance of the Armiento–Mattsson 2005 functional[3] (AM05) for a large set of crystalline solids. We show that AM05 systematically improves upon earlier functionals of the same class [the density and gradient based functionals local density approximation (LDA),[2] PBE,[4] BLYP,[5,6] and RPBE[7]]. The AM05 functional, in fact, performs as well as the hybrid functionals PBE0 (Refs. 8 and 9) and HSE06,[10] see Table I. In addition to two functionals commonly used for solid-state applications, LDA and PBE, we chose to include BLYP and RPBE because of the large and growing interest in water-solid interactions.[14] PBE and BLYP are both used extensively for water[14–19] and RPBE has been suggested to give a water structure in good agreement with experimental results.[15] The performance of AM05 for water will be presented elsewhere,[20] but preliminary results show that the behavior is similar to that of PBE. For water-solid interactions to be modeled correctly, however, it is crucial to model the bulk solid well to begin with. Crystallization of ice on a substrate is one example. Formation of ice depends sensitively on the matching of lattices, hence, the lattice constant of the solid has to be described with high accuracy.

While the XC functional determines the fundamental *accuracy* of the calculation, there is a second source of errors, the numerical *precision* in solving the Kohn–Sham equations. Implementation-related approximations, such as basis sets, pseudopotentials, approximate matrix diagonalization methods, plane-wave cutoff energies, etc. (see, e.g., Ref. 21) can all be successively improved by increasing the computational expense (i.e., by "converging" the calculations). The concept of precision is particularly important in the area of functional development. When the differences between functionals are small,[22,23] the precision of the calculations has to be high enough to resolve them.

In the following, we will give a brief theoretical background that covers the different functionals used in our study. Following this, we present a number of calculations of lattice constants and bulk moduli. Finally, the results are analyzed and discussed.

[a)]Electronic mail: aematts@sandia.gov.
[b)]Electronic mail: rickard.armiento@uni-bayreuth.de.
[c)]Electronic mail: joachim.paier@univie.ac.at.
[d)]Electronic mail: georg.kresse@univie.ac.at.
[e)]Electronic mail: jxw@lanl.gov.
[f)]Electronic mail: trmatts@sandia.gov.

 © 2008 American Institute of Physics

Downloaded 29 Feb 2008 to 134.253.26.4. Redistribution subject to AIP license or copyright; see http://jcp.aip.org/jcp/copyright.jsp

TABLE I. Mean error (ME), mean absolute error (MAE), and root mean square error (RMSE) for lattice constants a_0 (Å) and bulk moduli B_0 (GPa), for the functionals tested in this work [AM05, PBE, LDA, RPBE, BLYP, and the best of LDA or PBE (LoP) with respect to lattice constant or bulk modulus] and in Ref. 10 [PBE0, HSE06, and PBE, here denoted as PBE (∗)]. We have used VASP 5.1 (Refs. 10–13) and used the same PAW core potentials as were employed in Ref. 10. The excellent agreement between the present results and those of and Ref. 10 can be seen by comparing PBE and PBE (∗). Of the nonhybrid functionals, only AM05 performs as well as the hybrids. However, the computational cost using AM05 is only a fraction of that using hybrids.

	a_0 (Å)			B_0 (GPa)		
	ME	MAE	RMSE	ME	MAE	RMSE
AM05	0.001	0.025	0.033	−4.48	8.10	11.2
PBE0	0.007	0.022	0.029	−0.1	7.9	11.3
HSE06	0.010	0.023	0.030	−1.6	8.6	12.8
LoP (a_0)	0.006	0.040	0.048	−6.67	11.6	16.6
LoP (B_0)	−0.003	0.049	0.053	−2.45	7.26	9.79
PBE (∗)	0.039	0.045	0.054	−12.3	12.4	16.4
PBE	0.039	0.046	0.056	−14.1	14.2	18.3
LDA	−0.070	0.070	0.082	7.48	10.7	15.2
RPBE	0.090	0.091	0.113	−17.9	20.5	24.7
BLYP	0.093	0.100	0.114	−26.0	26.1	32.2

II. THEORETICAL BACKGROUND

In the Kohn–Sham DFT computational scheme,[2] the ground state electron energy is obtained via the solution of the Kohn–Sham (KS) equations. These equations resemble the Hartree–Fock (HF) equations. However, whereas the Hartree–Fock equations have a fully nonlocal exchange potential, the KS equations instead have an XC potential $v_{\mathrm{xc}}(\mathbf{r})$ that is diagonal and local in real space. This locality means that the equations are solved with significantly less computational expense. Also, in difference to the Hartree–Fock equations, the transformation of the many-body electron problem into the KS equations introduces no approximations in itself. All correlation effects can *formally* be accounted for within the XC potential $v_{\mathrm{xc}}(\mathbf{r})$. In practice, the crucial question is how good the approximation of this quantity is.

The XC potential $v_{\mathrm{xc}}(\mathbf{r})$ is obtained through functional differentiation of the DFT XC energy $E_{\mathrm{xc}}[n]$ as a functional of the ground state electron density $n(\mathbf{r})$. The XC energy is itself obtained from an integration of the exchange-correlation energy per particle $\epsilon_{\mathrm{xc}}(\mathbf{r};[n])$,

$$E_{\mathrm{xc}}[n] = \int n(\mathbf{r})\epsilon_{\mathrm{xc}}(\mathbf{r};[n])d\mathbf{r}. \tag{1}$$

A DFT XC functional is usually understood to mean an approximation to $\epsilon_{\mathrm{xc}}([n];\mathbf{r})$. This quantity is further split in separate exchange and correlation parts $\epsilon_{\mathrm{xc}}=\epsilon_{\mathrm{x}}+\epsilon_{\mathrm{c}}$. This separation originates from the choice that the exchange part should give the energy obtained from the Hartree–Fock exchange expression when the one-particle orbitals $\phi_i(\mathbf{r})$ obtained from solving the KS equations are inserted (in hartree atomic units, for a spin-unpolarized system, i.e., spin up and down orbitals are always filled equally),

$$\epsilon_{\mathrm{x}}(\mathbf{r};[n]) = -\int \frac{1}{n(\mathbf{r})|\mathbf{r}-\mathbf{r}'|}\left|\sum_i^{\mathrm{occ}} \phi_i(\mathbf{r}')\phi_i^*(\mathbf{r})\right|^2 d\mathbf{r}'. \tag{2}$$

However, any transformation, e.g., by integration by parts, of Eq. (1), gives alternative definitions of the exchange energy per particle[24] that are equally valid.

A. The local density approximation

The LDA XC functional was presented already in the early works on DFT.[2] LDA obtains the exchange energy from that of a uniform electron gas having a density equal to the local density $n(\mathbf{r})$ at each spatial point $\mathbf{r}$. Using this *model system*, the exchange energy can be derived exactly, giving the following exchange energy per particle,

$$\epsilon_{\mathrm{x}}^{\mathrm{LDA}}(n(\mathbf{r})) = -\frac{3}{4\pi}(3\pi^2 n(\mathbf{r}))^{1/3}. \tag{3}$$

The correlation energy per particle $\epsilon_{\mathrm{c}}^{\mathrm{LDA}}$ is obtained as a parametrization of quantum Monte Carlo data[25] for the uniform electron gas at different densities. In this work we use the parameterization of Perdew and Wang[26] for the all-electron full-potential calculations performed with the computer code named RSPT and that of Perdew and Zunger[27] for the VASP calculations, but these and other parameterizations are largely equivalent.

Despite its simple construction, LDA has proven successful for many applications, in particular, for solids. To improve upon the LDA form, more degrees of freedom than only the local value of the electron density $n(\mathbf{r})$ must be introduced in the approximation for the XC energy per particle. The usual way to extend the LDA form is to introduce the electron density gradient $\nabla n(\mathbf{r})$, giving a generalized gradient approximation (GGA) form for the XC energy approximation,

Downloaded 29 Feb 2008 to 134.253.26.4. Redistribution subject to AIP license or copyright; see http://jcp.aip.org/jcp/copyright.jsp

$$E_{xc}[n] = \int n(\mathbf{r})\epsilon_{xc}^{GGA}(n(\mathbf{r}),|\nabla n(\mathbf{r})|)d\mathbf{r}. \tag{4}$$

Historically, attempts were made to use a straightforward expansion of the XC energy in the density to produce a systematic improvement of LDA of this form. However, the outcome was disappointing and generally did not improve upon LDA results. Instead, several other approaches have been pursued. The ones important for this work are briefly discussed in the following sections.

B. Functionals from model systems, the AM05 functional

The method of employing model systems builds upon the strength of LDA: The exchange and correlation energy expressions stem from a single *model system*, the uniform electron gas, for which the exact results are known. This leads to an internal consistency between the exchange and correlation approximations, which makes the combined XC quantity more widely applicable than the individual approximations. We refer to this property as "compatible" exchange and correlation functionals. The compatibility manifests itself as a strong cancellation of errors between the exchange and correlation parts of LDA.

Kohn and Mattsson discussed the creation of a XC functional from a surface-oriented model system and its possible combination with another treatment where this model was unsuitable.[28,29] The approach was formalized and generalized in the subsystem functional scheme by Armiento and Mattsson.[24] The idea is to create separate functionals from different model systems and merge them using a density functional index[30] that locally determines the nature of the system. These ideas were made concrete in the AM05 functional.[3] It involves the following two model systems: For regions that are locally bulklike, the uniform electron gas is used; for regions that are locally surfacelike, a surface functional is derived from the Airy gas[28] in combination with the jellium surfaces.[31]

The AM05 surface exchange functional is a parameterization of the Airy electron gas data.[28] Such a parameterization was made by Vitos *et al.*,[32] but the AM05 exchange functional improves on it by imposing the correct limiting behavior for large scaled density gradients. The local Airy approximation (LAA) parameterization used in AM05 is given by

$$\epsilon_x^{LAA}(n(\mathbf{r}),|\nabla n(\mathbf{r})|) = \epsilon_x^{LDA}(n(\mathbf{r}))F_x^{LAA}(s), \tag{5}$$

where the scaled density gradient $s=|\nabla n(\mathbf{r})|/[2(3\pi^2)^{1/3}n^{4/3}(\mathbf{r})]$, and the refinement function $F_x^{LAA}(s)$ is defined as

$$F_x^{LAA}(s) = (cs^2+1)/(cs^2/F_x^b+1), \tag{6}$$

where $c=0.7168$ is a fitted constant. The form of $F_x^{LAA}(s)$ is chosen to impose a correct uniform limit onto F_x^b, which is constructed as an analytical interpolation between two known limits of the Airy refinement function as discussed below.

An effective scaled z coordinate in the Airy gas model,[3,28] exact in the limit of high values of s, can be defined as

$$\tilde{\zeta}(s) = \left[\frac{3}{2}W\left(\frac{s^{3/2}}{2\sqrt{6}}\right)\right]^{2/3}, \tag{7}$$

where W is the Lambert W function.[33] (This function can be calculated to machine accuracy by a few iteration steps implemented in a short piece of code; a routine is available from the authors.)

The properties of $\tilde{\zeta}(s)$ makes it possible to create an Airy refinement function that simultaneously satisfy both the true high and low s limits,

$$F_x^b = -1/[\epsilon_x^{LDA}(\tilde{n}_0(s))2\tilde{\tilde{\zeta}}(s)], \tag{8}$$

where $\tilde{\tilde{\zeta}}(s)$ is a suitable interpolation between the two limits,

$$\tilde{\tilde{\zeta}}(s) = ([(4/3)^{1/3}2\pi/3]^4\tilde{\zeta}(s)^2 + \tilde{\zeta}(s)^4)^{1/4}, \tag{9}$$

and where $n_0(s)$ is an effective density defined from the effective z coordinate $\tilde{\zeta}(s)$,

$$\tilde{n}_0(s) = \frac{\tilde{\zeta}(s)^{3/2}}{3\pi^2 s^3}. \tag{10}$$

For a fully compatible setup, the ϵ_x^{LAA} exchange functional should be combined with a correlation functional obtained as a parameterization of, e.g., quantum Monte Carlo data for the Airy gas system. However, with no such data available, Armiento and Mattsson derived a semicompatible surface correlation from the XC data available for jellium surface models, based on the idea that both the Airy gas and jellium surface models are related to similar surface physics. The basic idea is to correct for the difference in surface correlation, as compared to bulk correlation, by a simple scaling factor to the LDA expression. The scaling factor was obtained from a fit to the combined exchange and correlation energies for surface jellium data,[34] giving

$$\epsilon_c(\mathbf{r};[n]) = \gamma\epsilon_c^{LDA}(n(\mathbf{r})), \quad \gamma = 0.8098. \tag{11}$$

This fit used the Perdew–Wang parametrization of the LDA correlation,[26] which should thus always be used within AM05.

The surface functional is combined via the subsystem functional scheme with LDA for bulklike regions using a density index,

$$X = 1 - \alpha s^2/(1+\alpha s^2), \tag{12}$$

where $\alpha=2.804$ was obtained simultaneously with γ in the fit to surface jellium energy data [cf. comment to Eq. (11)]. The final composed expression for the AM05 exchange and correlation functionals are

$$\begin{aligned}\epsilon_x^{LAA}(\mathbf{r};[n]) &= \epsilon_x^{LDA}(n(\mathbf{r}))[X+(1-X)F_x^{LAA}(s)],\\ \epsilon_c^{LAA}(\mathbf{r};[n]) &= \epsilon_c^{LDA}(n(\mathbf{r}))[X+(1-X)\gamma].\end{aligned} \tag{13}$$

Downloaded 29 Feb 2008 to 134.253.26.4. Redistribution subject to AIP license or copyright; see http://jcp.aip.org/jcp/copyright.jsp

Note that, although AM05 is of the same form as a GGA, and can be easily implemented[35] in a code using the same input quantities as, e.g., PBE does, it stems from a different theoretical background than functionals originally referred to as GGAs (PW91, BLYP, and PBE).

The AM05 functional is the first functional constructed according to the subsystem functional scheme. It can be seen as a consistent improvement over LDA in the sense that it reproduces the exact XC energy for *two* types of model systems: The uniform electron gas and the jellium surfaces, describing two situations with fundamentally different physics. The subsystem functional approach outlines a series of further improved functionals, achieved by keeping the current exact XC model systems and adding others. In the application of AM05 to the solid-state systems of the current work (see Table I), we see how this formal improvement over LDA also translates into significantly improved numerical results.

C. Constraint-based construction, the PBE functional

When LDA was analyzed to better understand its success for systems dominated by electron densities far from uniform, it was observed that LDA fulfills a number of exact constraints that one can show also the exact XC functional fulfills. Several works, most prominently the ones of Perdew and co-workers, focus on this observation to argue that improved functionals can be constructed by retaining the constraints LDA fulfills and adding new ones.

One of the most prominent examples of a GGA XC functional is the popular and successful one of Perdew, Burke, and Ernzerhof (PBE).[4] For systems such as atoms and molecules, PBE constitutes a significant improvement over LDA. The derivation explicitly focuses on seven constraints that are fulfilled by the construction. Some of these are argued to be the energetically significant constraints of LDA, and others are new ones fulfilled in addition (see, e.g., the discussion in Ref. 36). However, despite PBE being constructed to fulfill the important constraints of LDA, it is not a uniform improvement on LDA for solids. Rather, for combined XC, PBE is, for example, less accurate than LDA for surface jellium,[36] a traditional solid-state model system. Although PBE often gives lattice constants in better agreement with experiments than LDA does, the same is not true for the bulk moduli (see Table I).

Since the publication of AM05 in 2005, other authors have also attempted to create functionals with improved performance for solids. Wu and Cohen's approach[37] results in the exchange term having a weaker dependence on the scaled gradient s than the PBE exchange has; a relatively weak s dependence is a property of both LAG[32] and AM05.[3,32] A very recent functional by Perdew *et al.*[38] also has an exchange term with a weak s dependence. For correlation, they follow closely the construction of AM05, and fit to the combined exchange and correlation energy for surface jellium. The resulting functional gives values close to AM05 over a range of s typically encountered in real solids, and, thus, we predict that this new functional will show a performance similar to that of AM05.

By allowing additional degrees of freedom in the XC energy per particle approximation than the gradient of the density, as used in the GGA form Eq. (4), further constraints can be satisfied. This leads to the concept of meta-GGAs which include, e.g., the kinetic energy density of the KS orbitals. The TPSS[39] meta-GGA functional is reported to give improved results over PBE, but since the testing was done on a slightly different set of solids and with a different code, it is not possible to make direct comparisons in this work (see Sec. IV B).

D. Empirical construction, the BLYP and RPBE functionals

An alternative to the constraint-based functional construction is the more pragmatic approach of empirical functionals. The governing principle is that good exchange and correlation functionals can be obtained from suitable generic expressions fitted to known energies. Traditionally, this approach has been more prevalent for functionals aimed at chemical systems than solid-state systems; perhaps due to the more readily available high-quality total energy data of, e.g., atoms that can be used for such fitting.

One of the most widely used functionals created from this idea is the BLYP XC functional. It is composed by the B88 exchange functional[5] and the LYP correlation.[6] Both these functionals rely on fits of their free parameters to atomic data. The BLYP functional has proven very successful for various applications in chemistry. However, from a theoretical standpoint, the LYP functional has been strongly criticized for a number of shortcomings: (i) It does not reproduce LDA in the limit of slowly varying densities; (ii) it gives zero correlation energy for any fully spin-polarized system; and (iii) its derivation involves theoretical problems related to non-normalized wavefunctions.[40] BLYP was implemented in VASP as a part of a recent study of the properties of B3LYP.[41]

There have also been attempts to turn PBE into a semi-empirical functional. Zhang and Yang created revPBE by giving up one of the PBE constraints, and instead refit one of its parameters to data on atoms ranging from helium to argon.[42] Hammer *et al.* observed that the refit not only gave improved chemisorption energies,[7] but also that this improvement could still be achieved without giving up any of the original PBE constraints by changing the form of the expression for the exchange functional. The result, the RPBE functional,[7] is not explicitly empirical in the sense that it does not directly involve any fits. However, the new exchange functional form was chosen because it reproduces relevant behavior of the exchange of revPBE, which was fitted to atomic data. As opposed to the LAG and AM05 functionals, the dependence on the scaled gradient s is stronger for the RPBE functional than for the PBE functional. Because of this, RPBE is not expected to improve on PBE for solid-state systems. On the contrary, because of the relatively strong s dependence the volume should increase compared to the PBE functional. This is indeed what we find in our tests (see Table I). It is, however, still relevant to include RPBE in the comparisons, since the choice of functional for mixed systems involves a trade-off with the goal of perform-

Downloaded 29 Feb 2008 to 134.253.26.4. Redistribution subject to AIP license or copyright; see http://jcp.aip.org/jcp/copyright.jsp

ing well enough for all parts. For such applications, our results may help assess how large the trade-off is in using RPBE for the solids.

E. Hybrid functionals

Hybrid functionals, which are characterized by the admixture of a certain amount of nonlocal Fock exchange to a part of local or semilocal DFT exchange, are extensively applied in the field of quantum chemistry. Results obtained using hybrid functionals are usually in significantly better agreement with experiments than those obtained using local or semilocal DFT exchange-correlation functionals (see, e.g., Ref. 43).

Becke was the first to successfully formulate a true Hartree–Fock/DFT hybrid scheme, known as "half-and-half functional."[44] In a subsequent publication, the semiempirical three-parameter hybrid functionals were introduced.[45] Although Becke's concept is motivated by the adiabatic connection formula for the exchange-correlation energy,[46–49] the free parameters are determined by a least-squares fit to experimental atomization energies, electron and proton affinities, and ionization potentials of atomic and molecular species in the G2 test set. The B3LYP hybrid functional has become one of the most popular semiempirical hybrid functionals in computational chemistry.

In Ref. 41, the performance of the B3LYP hybrid functional applied to crystalline solids is scrutinized. There, Paier *et al.* show that B3LYP performs significantly worse than even simpler and computationally less expensive gradient corrected functionals (such as PBE) for the prediction of almost any relevant property (lattice constants, bulk moduli, or cohesive energies) of systems containing elements beyond the second row. Moreover, cohesive energies for metals are wrong by up to typically 50%.[41] The bad performance for metals is not surprising since the B3LYP functional does not describe the homogeneous electron gas exactly.

A concept to rationalize the amount of Fock exchange admixed to the standard DFT exchange energy was devised by Perdew and co-workers.[8,50,51] Hybrid functionals motivated by this work are, often termed nonempirical or parameter-free and can be based on GGAs (PBE0, Refs. 9 and 52) or meta-GGAs (TPSSh, Ref. 53). The accuracy of nonempirical hybrid functionals has been shown to be not far from that of semiempirical ones for molecular systems. The way the functionals are derived and the lack of empirical parameters fitted to specific properties make these functionals applicable to both quantum chemistry and condensed matter physics. Comprehensive studies of the performance of PBE0[8,9] and HSE06[55] for crystalline solids were published recently.[10,41,54,55]

A major limitation of hybrid schemes, however, is a steep increase in computational cost for periodic systems. Exact exchange HF calculations are typically an order of magnitude slower than local or semilocal density functional calculations. The actual difference in computational cost depends on program package and the electronic structure of the system (metallic, semiconducting, or insulating). At present, the applicability of hybrids to large systems and/or long MD simulations is substantially limited by computational resources.

III. RESULTS

A. VASP calculations

Our VASP results are summarized in Tables II and III. The pseudopotential, plane-wave calculations were done with VASP 5.1,[10,11,13] using projector augmented wave (PAW) core potentials.[56] We applied the same PAW cores as those used by Paier *et al.* in their assessment of hybrid functionals for solids.[10] The PAW implementation in VASP 5.1 allows use of multiple XC functionals on the same set of core potentials[13] while retaining high precision. Although the core wave functions are frozen in the configuration determined as the PAW core is constructed (say, an LDA atom), the core-valence interaction is consistently recalculated with the selected functional. Transferability errors are hence reduced.[13] By performing the AM05 and BLYP calculations on both the LDA and PBE cores, we conclude that the errors thereby introduced are insignificant. In addition, we did full-potential all-electron calculations for all solids, the results of which confirm that the PAW cores developed for VASP are of very high fidelity.

The *k*-point integration was performed using the tetrahedron method with Blöchl corrections[57] on an $18\times18\times18$ uniform grid[58] centered at the gamma point. All real-space cells are cubic with two atoms for bcc, four atoms for fcc, and eight atoms for the zinc blende and diamond cells. We applied energy cutoffs ranging between 600 and 1000 eV: 600 eV (Al, Ag, Pd, Rh, Cu, GaAs, GaP), 800 eV (Na, NaF, NaCl, MgO, SiC, Si, C, GaN, BN, BP), and 1000 eV (Li, LiF, LiCl) with a convergence criterion of 1.0×10^{-5} eV for the self-consistent loop. The precision in the calculations is thus overall very high. The PBE results can be directly compared to those of Paier *et al.*;[10] the discrepancies are minute and caused by slight differences in the volume range governing the Murnaghan fits. None of the differences affect any conclusions.

B. RSPT calculations

To confirm the validity of using PAW core potentials created with LDA or PBE together with AM05 in VASP 5.1, we have performed all-electron calculations for the same set of solids using the RSPT (Ref. 59) code. To further compare the results given by the two codes, we have also performed LDA and PBE calculations with RSPT. The results are compared in Tables IV and V.

The RSPT code[59] is a full-potential linear muffin tin orbital (LMTO) code. Since it uses an efficient smaller basis set, it is fast compared to other all-electron codes, while the flexible basis, that has been specially built for every single solid, permits very well converged results. Our primary concern has been to construct a basis with small "leakage," that is, to only keep as core orbitals the orbitals that do not significantly contribute to the density outside of the muffin tin spheres. We have thus, in most cases, used a larger number of valence orbitals than is needed for production runs. We

Downloaded 29 Feb 2008 to 134.253.26.4. Redistribution subject to AIP license or copyright; see http://jcp.aip.org/jcp/copyright.jsp

TABLE II. Lattice constants a_0 (Å), ME, MAE, RMSE, and mean absolute relative error (MARE), obtained with the AM05, LDA, PBE, BLYP, and RPBE functionals, using VASP. The experimental (Exp) results are the same as used in Refs. 10 and 61.

Solid	Exp	AM05	LDA	PBE	BLYP	RPBE
Li	3.477	3.455	3.359	3.433	3.421	3.476
Na	4.225	4.212	4.052	4.201	4.210	4.295
Al	4.032	4.004	3.984	4.041	4.116	4.064
BN	3.616	3.605	3.583	3.627	3.647	3.646
BP	4.538	4.516	4.491	4.548	4.592	4.573
C	3.567	3.551	3.534	3.573	3.598	3.590
Si	5.430	5.431	5.403	5.467	5.532	5.499
SiC	4.358	4.350	4.330	4.377	4.411	4.398
β-GaN	4.520	4.492	4.460	4.548	4.611	4.511
GaP	5.451	5.441	5.394	5.509	5.607	5.556
GaAs	5.648	5.672	5.611	5.755	5.871	5.812
LiF	4.010	4.039	3.908	4.065	4.084	4.146
LiCl	5.106	5.119	4.962	5.150	5.232	5.254
NaF	4.609	4.686	4.508	4.708	4.716	4.824
NaCl	5.595	5.686	5.466	5.702	5.763	5.847
MgO	4.207	4.232	4.168	4.259	4.281	4.302
Cu	3.603	3.565	3.523	3.637	3.711	3.682
Rh	3.798	3.773	3.757	3.833	3.905	3.857
Pd	3.881	3.872	3.844	3.946	4.034	3.984
Ag	4.069	4.054	4.002	4.150	4.262	4.215
ME	⋯	0.001	−0.070	0.039	0.093	0.090
MAE	⋯	0.025	0.070	0.046	0.100	0.091
RMSE	⋯	0.033	0.082	0.056	0.114	0.113
MARE	⋯	0.6%	1.6%	1.0%	2.2%	2.0%

TABLE III. Bulk moduli B_0 (GPa), obtained with the AM05, LDA, PBE, BLYP, and RPBE functionals, using VASP. The experimental (Exp) results are the same as used in Refs. 10 and 61. For the materials marked with a star "*," different experimental data are frequently quoted in the III–V literature, see Sec. IV C.

Solid	Exp	AM05	LDA	PBE	BLYP	RPBE
Li	13.0	13.0	15.1	13.7	13.7	13.1
Na	7.5	7.36	9.22	7.62	7.08	6.94
Al	79.4	83.9	81.4	75.2	54.9	73.7
BN	400*	378	394	365	350	353
BP	165	165	171	158	146	152
C	443	442	456	424	399	410
Si	99.2	90.2	93.6	86.4	77.0	83.1
SiC	225	217	224	208	194	201
β-GaN	210*	181	196	166	152	237
GaP	88.7	80.2	87.0	74.3	64.3	69.4
GaAs	75.6	65.1	71.8	59.7	50.6	55.2
LiF	69.8	65.8	85.7	66.7	65.5	59.3
LiCl	35.4	30.3	40.4	31.2	28.9	27.3
NaF	51.4	43.2	60.1	44.5	44.3	38.3
NaCl	26.6	22.0	31.4	23.4	22.0	20.1
MgO	165	152	169	148	145	139
Cu	142	157	180	134	112	120
Rh	269	285	304	249	214	232
Pd	195	194	216	165	137	148
Ag	109	109	132	88.9	71.2	74.4
ME	⋯	−4.48	7.48	−14.1	−26.0	−17.9
MAE	⋯	8.10	10.7	14.2	26.1	20.5
RMSE	⋯	11.2	15.2	18.3	32.2	24.7
MARE	⋯	7.1%	10.8%	10.4%	18.7%	16.0%

Downloaded 29 Feb 2008 to 134.253.26.4. Redistribution subject to AIP license or copyright; see http://jcp.aip.org/jcp/copyright.jsp

TABLE IV. Lattice constants a_0 (Å), obtained with AM05, LDA, and PBE, using VASP and RSPT. The AM05 VASP results are calculated using LDA and PBE PAW core potentials. As shown, the results are nearly identical. The AM05 values given in Tables II and III are the mean of the AM05 values obtained with LDA and PBE PAW core potentials. The two different codes also give similar results, showing that using PBE or LDA PAW core potentials for AM05 calculations in VASP is a valid approach.

	AM05			LDA		PBE	
	VASP		RSPT	VASP	RSPT	VASP	RSPT
Solid	LDA PAW	PBE PAW		LDA PAW		PBE PAW	
Li	3.4539	3.4559	3.456	3.359	3.362	3.433	3.434
Na	4.2124	4.2125	4.222	4.052	4.053	4.201	4.196
Al	4.0003	4.0076	4.008	3.984	3.986	4.041	4.043
BN	3.6026	3.6071	3.604	3.583	3.583	3.627	3.625
BP	4.5118	4.5203	4.520	4.491	4.495	4.548	4.553
C	3.5497	3.5529	3.551	3.534	3.534	3.573	3.573
Si	5.4306	5.4317	5.436	5.403	5.405	5.467	5.474
SiC	4.3491	4.3514	4.361	4.330	4.337	4.377	4.386
β-GaN	4.4914	4.4921	4.506	4.460	4.465	4.548	4.553
GaP	5.4385	5.4435	5.457	5.394	5.405	5.509	5.518
GaAs	5.6689	5.6747	5.686	5.611	5.620	5.755	5.761
LiF	4.0364	4.0420	4.041	3.908	3.912	4.065	4.065
LiCl	5.1163	5.1223	5.114	4.962	4.966	5.150	5.149
NaF	4.6860	4.6866	4.685	4.508	4.507	4.708	4.692
NaCl	5.6844	5.6877	5.693	5.466	5.467	5.702	5.692
MgO	4.2352	4.2291	4.221	4.168	4.164	4.259	4.253
Cu	3.5641	3.5668	3.564	3.523	3.522	3.637	3.633
Rh	3.7729	3.7729	3.786	3.757	3.769	3.833	3.845
Pd	3.8713	3.8727	3.880	3.844	3.852	3.946	3.953
Ag	4.0538	4.0549	4.062	4.002	4.010	4.150	4.155
ME	−0.001	0.002	0.006	−0.070	−0.066	0.039	0.041
MAE	0.026	0.025	0.022	0.070	0.066	0.046	0.048
RMSE	0.033	0.033	0.033	0.082	0.079	0.056	0.056
MARE	0.6%	0.6%	0.5%	1.6%	1.5%	1.0%	1.1%

have used the same basis for a specific solid for all different functionals. For each of the seven volume points considered in the fits to the Murnaghan[60] equation of state, the muffin tin radius was varied so as to give a muffin tin sphere with a specific fraction of the cell volume. The volumes have been centered around the equilibrium volume given by the VASP calculations and spaced between $\pm 3\%$ of the equilibrium lattice constants. The cells used have all been primitive. We used a $24\times 24\times 24$ k-point grid shifted by $(1/2,1/2,1/2)$ for all solids and we used the tetrahedron method for integrating the k space. The Fourier grid was $30\times 30\times 30$.

Tables IV and V show that the differences using LDA or PBE core potentials in the VASP AM05 calculations are minute and that either set of results compares well with the all-electron RSPT calculations. Thus, if it is not possible to do both sets of AM05 calculations and use the mean, as we have done in this work, the choice between using LDA or PBE core potentials together with AM05, could be left as a practical consideration. For example, if LDA will also be used, LDA core potentials could be employed also for AM05.[64]

The comparison between RSPT and VASP LDA and PBE values also confirms that the VASP LDA and PBE core potentials almost always reproduce the all-electron lattice constants to within 0.1%–0.2%.

With RSPt, we have also confirmed that PBE and PW91 indeed give nearly identical results for lattice constants and bulk moduli of solids, something that led users to believe that PBE and PW91 would perform equally on all types of systems. However, this has been shown not to be the case (see Refs. 22 and 23).

In addition to the set of 20 solids, we next turn to a few additional metals: A heavy bcc metal (W), two heavy fcc elements (Pt and Au), and a light hcp metal (Be). Be is an hcp metal with experimental lattice constants $a=2.29$ Å and $c=1.567$ Å. Our results for (a,c) are the following: (2.232,1.58) for LDA, (2.264,1.58) for PBE, and (2.255,1.58) for AM05. The results for W, Pt, and Au are presented in Table VI. The PAW core potentials include scalar relativistic corrections and treat the semicore p states as valence. The number of valence electrons are thus 12 for W, 11 for Au, and 10 for Pt. It is well known that LDA is superior to PBE for these heavy elements (BLYP and RPBE both give results worse than PBE). AM05 yields lattice constants as well as bulk moduli in very good agreement with experimental data. The addition in AM05 of a surface model system to the LDA bulk region thus did not negatively affect the performance for this class of elements.

Downloaded 29 Feb 2008 to 134.253.26.4. Redistribution subject to AIP license or copyright; see http://jcp.aip.org/jcp/copyright.jsp

TABLE V. Bulk moduli B_0 (GPa), obtained with AM05, LDA, and PBE, using VASP and RSPT. The AM05 VASP results are calculated using LDA and PBE PAW core potentials. As shown, the results are nearly identical. The two different codes also give similar results, showing that using PBE or LDA PAW core potentials for AM05 calculations in VASP is a valid approach.

	AM05			LDA		PBE	
	VASP		RSPT	VASP	RSPT	VASP	RSPT
Solid	LDA PAW	PBE PAW		LDA PAW		PBE PAW	
Li	13.01	12.99	13.2	15.1	15.0	13.7	13.9
Na	7.363	7.361	7.65	9.22	9.16	7.62	7.74
Al	84.08	83.63	86.2	81.4	82.5	75.2	77.1
BN	378.5	377.5	384	394	400	365	370
BP	165.1	164.3	168	171	174	158	160
C	442.5	441.4	450	456	465	424	431
Si	90.30	90.11	92.0	93.6	95.4	86.4	87.5
SiC	216.9	216.3	217	224	226	208	208
β-GaN	180.6	180.5	183	196	199	166	170
GaP	80.31	80.13	81.1	87.0	88.2	74.3	75.1
GaAs	65.08	65.07	65.4	71.8	72.4	59.7	59.4
LiF	65.85	65.82	65.8	85.7	86.2	66.7	67.5
LiCl	30.31	30.25	30.7	40.4	41.0	31.2	31.9
NaF	43.27	43.08	42.4	60.1	60.4	44.5	45.6
NaCl	22.04	21.99	21.0	31.4	31.5	23.4	23.7
MgO	151.3	151.9	154	169	171	148	149
Cu	157.4	157.3	165	180	187	134	140
Rh	285.3	285.5	293	304	312	249	253
Pd	194.2	193.9	202	216	224	165	167
Ag	108.6	108.9	114	132	137	88.9	90.2
ME	−4.38	−4.59	−1.80	7.48	10.4	−14.1	−12.1
MAE	8.03	8.19	9.27	10.7	12.3	14.2	12.2
RMSE	11.2	11.3	11.9	15.2	18.4	18.3	16.2
MARE	7.1%	7.2%	8.1%	10.8%	11.8%	10.4%	9.3%

IV. DISCUSSION

A. AM05 is better than the best of LDA and PBE

For most realistic solid-state applications, such as size-converged calculations of defect formation energies and migration energies, the use of a hybrid functional is not practical because of the prohibitive computational cost. This is true, in particular, for investigating mixed systems (alloys or solid/molecular systems) at nonzero temperatures. Such calculations require both DFT based molecular dynamics (DFT-MD) and large supercells. For these demanding applications, a functional based only on quantities that are easily calculated, such as density and density derivatives, is currently paramount.

It could be argued that there is no need for new functionals for solid-state systems since the existing LDA and PBE do yield good results. In particular, by selecting the best of LDA or PBE, for a specific system, the result can be further improved. However, such a choice between LDA and PBE is not possible if reliable experimental data is not available. Resorting to using either LDA or PBE depending on application is, therefore, not an approach with predictive power. The approach is particularly uncertain in mixed systems where LDA would be preferred for one component of the system and PBE for another. However, even when disregarding these shortcomings, Table VII shows that relying only on AM05, in general, is a better alternative than choosing the result of LDA or PBE that is closest to experiment. AM05 is significantly better for lattice constants, and, within the relevant precision of bulk moduli calculations, AM05 matches the results obtained when picking LDA or PBE depending on the system.

TABLE VI. VASP results for the heavy metals W, Pt, and Au: AM05 performs as well, or better, than LDA.

	a_0 (Å)				B_0 (GPa)			
	Exp	AM05	LDA	PBE	Exp	AM05	LDA	PBE
W	3.16	3.153	3.142	3.190	310	333	335	310
Pt	3.92	3.915	3.906	3.977	283	292	307	251
Au	4.065	4.076	4.053	4.161	166–171	164	183	137

Downloaded 29 Feb 2008 to 134.253.26.4. Redistribution subject to AIP license or copyright; see http://jcp.aip.org/jcp/copyright.jsp

TABLE VII. VASP results for lattice constants a_0 (Å) and bulk moduli B_0 (GPa), obtained with the best of LDA or PBE. The experimental (Exp) results are the same as used in Refs. 10 and 61. This choice between LDA and PBE is a common practice but the result is less accurate than using AM05.

	a_0 (Å)			B_0 (GPa)		
Solid	Exp	Best a_0	a_0 for best B_0	Exp	B_0 for best a_0	Best B_0
Li	3.477	3.433	3.433	13.0	13.7	13.7
Na	4.225	4.201	4.201	7.5	7.62	7.62
Al	4.032	4.041	3.984	79.4	75.2	81.4
BN	3.616	3.627	3.583	400	365	394
BP	4.538	4.548	4.491	165	158	171
C	3.567	3.573	3.534	443	424	456
Si	5.430	5.403	5.403	99.2	93.6	93.6
SiC	4.358	4.377	4.330	225	208	224
β-GaN	4.520	4.548	4.460	210	166	196
GaP	5.451	5.394	5.394	88.7	87.0	87.0
GaAs	5.648	5.611	5.611	75.6	71.8	71.8
LiF	4.010	4.065	4.065	69.8	66.7	66.7
LiCl	5.106	5.150	5.150	35.4	31.2	31.2
NaF	4.609	4.708	4.708	51.4	44.5	44.5
NaCl	5.595	5.702	5.702	26.6	23.4	23.4
MgO	4.207	4.168	4.168	165	169	169
Cu	3.603	3.637	3.637	142	134	134
Rh	3.798	3.833	3.833	269	249	249
Pd	3.881	3.844	3.844	195	216	216
Ag	4.069	4.002	4.150	109	132	88.9
ME	⋯	0.006	−0.003	⋯	−6.67	−2.45
MAE	⋯	0.040	0.049	⋯	11.6	7.26
RMSE	⋯	0.048	0.053	⋯	16.6	9.79
MARE	⋯	0.9%	1.1%	⋯	8.0%	6.2%

B. Differences between codes

Solid-state codes solve the KS equations using approximations that lead to less than perfect precision. When dealing with and comparing such small errors as those of AM05 and hybrids (see Table I), it is relevant to ask whether it is possible to determine which one is more accurate, and whether it is at all possible to conclude that another functional performs better or worse than AM05 (and hybrids) for the present solid-state systems.

Table V of Ref. 10 gives PBE lattice constants and bulk moduli for a subset of the 20 solids studied in this work, calculated using VASP, a full-potential LAPW code, and a Gaussian-type-orbital (GTO) code.

Our RSPt values compare extremely well with the PBE APW+lo values and the VASP values in Table V of Ref. 10, although it seems that the error bars of the RSPt calculations are slightly larger. Specifically, the RSPT lattice constants deviate by up to 0.3% from the VASP values and from the APW+lo values, whereas the difference between the VASP and APW+lo lattice constants is not exceeding 0.1%. It is still clear that all three codes are able to give highly converged results, and the results mutually support each other. In particular, for LDA and PBE, the VASP and RSPT statistical errors are practically identical. For the AM05 case, the use of LDA and PBE cores might slightly increase the VASP error bars, as indicated by the comparison of AM05 for RSPT and VASP. However, the error bars are still smaller than approximately 0.005 Å in the lattice constants and 3 GPa in the bulk moduli. The same error bars are likely to apply to the HSE03 case, covered originally in Ref. 10. Hence, the difference in accuracy between the hybrids and AM05 cannot be resolved.

The small numerical error bars for the VASP 5.1 PAW calculations in this work and the work of Paier *et al.*[10] are not common to pseudopotential codes.[22] Comparing the data in Table I to data obtained with different codes and different types of pseudopotentials can thus not be done with the same small error bars, but the error bars should be expected to be significantly larger, if conventional pseudopotentials are applied.

The same conclusion holds for results obtained with all-electron GTO codes. The results in Table 5 of Ref. 10 (collected from Ref. 61) obtained with a GTO code do not compare as well with the LAPW results as the RSPT ones do.

C. Differences to experimental data

The precision of the best codes and accuracy of the best functionals for solid-state calculations are now at a level where further improvement in accuracy likely cannot be distinguished without a better understanding of experimental error bars. Although not conclusive in itself, we note that the three best functionals in this study (AM05, HSE06, and PBE0) give the same accuracy within numerical uncertainties, indicating that the remaining disagreement might be a sign of experimental errors and not a consequence of functional accuracy.

An analysis of the VASP results in Table III reveals that

Downloaded 29 Feb 2008 to 134.253.26.4. Redistribution subject to AIP license or copyright; see http://jcp.aip.org/jcp/copyright.jsp

two solids alone account for a large part of the mean bulk moduli errors between AM05 and experimental data. The solids, with their respective errors in parenthesis, are GaN (−29.5 GPa) and BN (−22.0 GPa). Both errors are surprisingly large, at first suggesting that AM05 has a systematic problem with III-V nitrides. However, theoretical studies more specifically targeting these kinds of system quote other experimental values for the bulk modulus, namely, 190 GPa for GaN and 369 GPa for BN.[62] Using these values instead of the ones provided in Ref. 61 changes the AM05 errors for these two solids to the more expected −9 GPa for GaN and +9 GPa for BN. These two changes in experimental values yield a mean error (ME) of −1.93 GPa, a mean absolute error (MAE) of 6.45 GPa, a root mean square error (RMSE) of 8.19 GPa, and a mean absolute relative error (MARE) of 6.5% for AM05. Adapting this change in experimental values, the PBE0 and HSE06 results for these quantities would be slightly increased. This observation does not imply that AM05 has better accuracy for the bulk moduli than do the hybrids, but it does illustrate the difficulty in distinguishing between the performance of different functionals which have an accuracy at the level of AM05 and the hybrids. Although a comprehensive review of available experimental results is of interest, not only for GaN and BN, but for all solids, such an investigation is outside the scope of the present work.

A similar examination of the two solids with unusually large AM05 errors in lattice constants, NaF and NaCl, does not provide such a simple explanation. We should note that the AM05 lattice constants for these materials compare better to the experimental values than LDA and PBE, and that both hybrids' results, though closer, still have substantial deviations. Since RSPT confirms the VASP values, the PAW core potentials cannot be at fault. Considering these caveats, one can draw only few definite conclusions on the relative performance of the HSE06 and AM05 functionals. Generally, AM05 predicts slightly smaller lattice constants than the two hybrid functionals do. Interestingly, it also predicts smaller bulk moduli than HSE06, although the energy volume curvature is usually expected to increase at smaller volumes. Concomitantly, the average bulk moduli are slightly underestimated by AM05 compared to experiment. The underestimation is modest for the metals and semiconductors, but clearly increases towards more ionic compounds and becomes as large as 20% for the two most ionic compounds, NaF and NaCl. As already mentioned, these are the compounds with the largest errors in the AM05 lattice constants. The hybrid functionals performed very well for these two systems yielding a much larger—albeit still too small—curvature at the equilibrium volume. We note that these systems, as well as other ionic compounds, are largely exchange dominated in the sense of the adiabatic coupling theorem, i.e., the adiabatic coupling theorem and the GW method suggest that one should include a large fraction of the nonlocal exchange to account for the physics in these systems. In summary, ionic compounds are the only bulk systems where hybrid functionals might offer an advantage over the AM05 functional. The opposite applies to the metallic systems, where the AM05 functional seems to give an overall slightly better description than the hybrid functionals, in particular, for the bulk moduli. More reliable error bars on the experimental values are required before further definite statements can be made.

V. CONCLUSIONS

The subsystem functional AM05 is based on two exact reference systems: The uniform electron gas and the surface jellium. AM05 hence constitutes a systematic improvement upon LDA by adding terms depending on the gradient of the density while maintaining the exact exchange-correlation limit of LDA. The systematic improvement is confirmed numerically by our careful solid-state benchmarks (cf. Table I). Not only is AM05 found to be a significant improvement over LDA, but also for the studied quantities over other often-used functionals, e.g., PBE, BLYP, and RPBE. Within the high numerical precision of this study, AM05 is found to be as accurate as the most advanced hybrid functionals proposed to date, PBE0 and HSE06. The only exception are ionic systems, where AM05 clearly improves upon PBE, but still yields much too large volumes and much too small bulk moduli.

In further analysis, we find the performance of AM05, on average, to be even better than what a computational user would reach by choosing between LDA and PBE with guidance from experimental knowledge. Hence, AM05 provides a predictive power neither of these two functionals possess. Our comparison of results from different codes also shows that the level of precision available in modern codes, and the size of experimental errors for solid-state systems, will make it difficult to register a further improved functional for these applications without going far beyond the benchmark systems and properties studied in this work. Note that the AM05 construction was made solely on a theoretical and nonempirical basis. The excellent results thus strongly points to it having a sound theoretical basis. Furthermore, we would like to emphasize that the theoretical foundation of AM05 is fundamentally different from those of other available functionals (cf. Sec. II B). In studies where the calculated value is to be relied upon, in particular, when experimental data are either unavailable or have large uncertainties, more than one functional is often applied as a means to assess the accuracy. It is in such cases beneficial to employ functionals that are based on different fundamental principles.

The high speed and precision of the computer code VASP 5.1 makes it an excellent choice for functional assessment, expanding the possibilities of initial testing from simple properties for few atoms to include also large systems and DFT-MD. For the applications of this work, we found its PAW core potentials to be general enough to be interchangeable between different functionals, which saves the otherwise tedious work of generating pseudopotentials. Note, however, that this is a property pertaining to the PAW scheme and the implementation used by this code. Pseudopotentials generated according to other schemes are generally *not interchangeable* and doing so may severely affect the computational results.

Downloaded 29 Feb 2008 to 134.253.26.4. Redistribution subject to AIP license or copyright; see http://jcp.aip.org/jcp/copyright.jsp

ACKNOWLEDGMENTS

We thank Peter Feibelman for useful conversations. We have had valuable discussions regarding bulk moduli and equations of state with Michael Desjarlais and John Carpenter. Per Andersson provided advice in how to work with the RSPT code. R.A. gratefully acknowledges support from the Alexander von Humboldt Foundation. A.E.M. and T.R.M. acknowledge support from the LDRD office at Sandia. Sandia is a multiprogram laboratory operated by Sandia Corporation, a Lockheed Martin Company, for the United States Department of Energy's National Nuclear Security Administration under Contract No. DE-AC04-94AL85000. Los Alamos National Laboratory is operated by Los Alamos National Security, LLC, for the National Nuclear Security Administration of the U.S. Department of Energy under Contract No. DE-AC52-06NA25396. Support by the Austrian Science Fund (FWF) is gratefully acknowledged.

[1] P. Hohenberg and W. Kohn, Phys. Rev. **136**, B864 (1964).
[2] W. Kohn and L. J. Sham, Phys. Rev. **140**, A1133 (1964).
[3] R. Armiento and A. E. Mattsson, Phys. Rev. B **72**, 085108 (2005).
[4] J. P. Perdew, K. Burke, and M. Ernzerhof, Phys. Rev. Lett. **77**, 3865 (1996).
[5] A. D. Becke, Phys. Rev. A **38**, 3098 (1988).
[6] C. Lee, W. Yang, and R. G. Parr, Phys. Rev. B **37**, 785 (1988).
[7] B. Hammer, L. B. Hansen, and J. K. Nørskov, Phys. Rev. B **59**, 7413 (1999).
[8] J. P. Perdew, M. Ernzerhof, and K. Burke, J. Chem. Phys. **105**, 9982 (1996).
[9] C. Adamo and V. Barone, J. Chem. Phys. **110**, 6158 (1999).
[10] J. Paier, M. Marsman, K. Hummer, G. Kresse, I. C. Gerber, and J. G. Ángyán, J. Chem. Phys. **124**, 154709 (2006); **125**, 249901 (2006).
[11] G. Kresse and J. Hafner, Phys. Rev. B **47**, R558 (1993); **49**, 14251 (1994); G. Kresse and J. Furthmüller, *ibid.* **54**, 11169 (1996).
[12] The calculations were made using version 5.1.38 of the VASP code.
[13] J. Paier, R. Hirschl, M. Marsman, and G. Kresse, J. Chem. Phys. **122**, 234102 (2005).
[14] P. J. Feibelman, Science **295**, 5552 (2002).
[15] D. Asthagiri, L. R. Pratt, and J. D. Kress, Phys. Rev. E **68**, 041505 (2003).
[16] E. Schwegler, J. C. Grossman, F. Gygi, and G. Galli, J. Chem. Phys. **121**, 5400 (2004).
[17] J. VandeVondele, F. Mohamed, M. Krack, J. Hutter, and M. Parrinello, J. Chem. Phys. **122**, 014515 (2005).
[18] H.-L. Sit and N. Marzari, J. Chem. Phys. **122**, 204510 (2005).
[19] H. S. Lee and M. Tuckerman, J. Chem. Phys. **125**, 154507 (2006).
[20] A. E. Mattsson and T. R. Mattsson (unpublished).
[21] A. E. Mattsson, P. A. Schultz, M. P. Desjarlais, T. R. Mattsson, and K. Leung, Modell. Simul. Mater. Sci. Eng. **13**, R1 (2005).
[22] A. E. Mattsson, R. Armiento, P. A. Schultz, and T. R. Mattsson, Phys. Rev. B **73**, 195123 (2006).
[23] B. Santra, A. Michaelides, and M. Scheffler, J. Chem. Phys. **127**, 184104 (2007).
[24] R. Armiento and A. E. Mattsson, Phys. Rev. B **66**, 165117 (2002).
[25] D. M. Ceperley and B. J. Alder, Phys. Rev. Lett. **45**, 566 (1980).
[26] J. P. Perdew and Y. Wang, Phys. Rev. B **45**, 13244 (1992).
[27] J. P. Perdew and A. Zunger, Phys. Rev. B **23**, 5048 (1981).
[28] W. Kohn and A. E. Mattsson, Phys. Rev. Lett. **81**, 3487 (1998).
[29] A. E. Mattsson and W. Kohn, J. Chem. Phys. **115**, 3441 (2001).
[30] J. P. Perdew, J. Tao, and R. Armiento, Acta Phys. Chim. Debrecina **36**, 25 (2003).
[31] N. D. Lang and W. Kohn, Phys. Rev. B **1**, 4555 (1970).
[32] L. Vitos, B. Johansson, J. Kollár, and H. L. Skriver, Phys. Rev. B **62**, 10046 (2000).
[33] G. H. Gonnet, D. E. G. Hare, D. J. Jeffrey, and D. E. Knuth, Adv. Comput. Math. **5**, 329 (1996).
[34] Z. Yan, J. P. Perdew, and S. Kurth, Phys. Rev. B **61**, 16430 (2000).
[35] Subroutines for AM05 are available from two of the authors (A.E.M. and R.A.).
[36] S. Kurth, J. P. Perdew, and P. Blaha, Int. J. Quantum Chem. **75**, 889 (1999).
[37] Z. Wu and R. E. Cohen, Phys. Rev. B **73**, 235116 (2006); F. Tran, R. Laskowski, P. Blaha, and K. Schwarz, *ibid.* **75**, 115131 (2007).
[38] J. P. Perdew, A. Ruzsinszky, G. I. Csonka, O. A. Vydrov, G. E. Scuseria, L. A. Constantin, X. Zhou, and K. Burke (unpublished).
[39] J. Tao, J. P. Perdew, V. N. Staroverov, and G. E. Scuseria, Phys. Rev. Lett. **91**, 146401 (2003); V. N. Staroverov, G. E. Scuseria, J. T. Tao, and J. P. Perdew, Phys. Rev. B **69**, 075102 (2004).
[40] X.-Y. Pan, V. Sahni, and L. Massa, Int. J. Quantum Chem. **107**, 816 (2006).
[41] J. Paier, M. Marsman, and G. Kresse, J. Chem. Phys. **127**, 024103 (2007).
[42] Y. Zhang and W. Yang, Phys. Rev. Lett. **80**, 890 (1998).
[43] L. A. Curtiss, K. Raghavachari, P. C. Redfern, and J. A. Pople, J. Chem. Phys. **106**, 1063 (1997).
[44] A. D. Becke, J. Chem. Phys. **98**, 1372 (1993).
[45] A. D. Becke, J. Chem. Phys. **98**, 5648 (1993).
[46] J. Harris and R. O. Jones, J. Phys. F: Met. Phys. **4**, 1170 (1974).
[47] O. Gunnarsson and B. I. Lundqvist, Phys. Rev. B **13**, 4274 (1976).
[48] D. C. Langreth and J. P. Perdew, J. Phys. F: Met. Phys. **15**, 2884 (1977).
[49] J. Harris, Phys. Rev. A **29**, 1648 (1984).
[50] M. Ernzerhof, Chem. Phys. Lett. **263**, 499 (1996).
[51] M. Ernzerhof, J. P. Perdew, and K. Burke, Int. J. Quantum Chem. **64**, 285 (1996).
[52] M. Ernzerhof and G. E. Scuseria, J. Chem. Phys. **110**, 5029 (1999).
[53] V. N. Staroverov, G. E. Scuseria, J. Tao, and J. P. Perdew, J. Chem. Phys. **119**, 12129 (2003).
[54] J. Heyd, J. E. Peralta, G. E. Scuseria, and R. L. Martin, J. Chem. Phys. **123**, 174101 (2005).
[55] A. V. Krukau and O. A. Vydrov, A. F. Izmaylov, and G. E. Scuseria, J. Chem. Phys. **125**, 224106 (2006).
[56] P. E. Blöchl, Phys. Rev. B **50**, 17953 (1994); G. Kresse and D. Joubert, *ibid.* **59**, 1758 (1999).
[57] P. E. Blöchl, O. Jepsen, and O. K. Andersen, Phys. Rev. B **49**, 16223 (1994).
[58] H. J. Monkhorst and J. D. Pack, Phys. Rev. B **13**, 5188 (1976).
[59] J. M. Wills, O. Eriksson, M. Alouani, and D. L. Price, Lect. Notes Phys. **535**, 148 (2000); AM05 is implemented in the version available at http://www.rspt.net
[60] F. D. Murnaghan, Proc. Natl. Acad. Sci. U.S.A. **30**, 244 (1944).
[61] J. Heyd and G. E. Scuseria, J. Chem. Phys. **121**, 1187 (2004).
[62] H. M. Tütüncü, S. Bağci, G. P. Srivastava, A. T. Albudak, and G. Uğur, Phys. Rev. B **71**, 195309 (2005).
[63] In practice, basis sets, k points, pseudopotentials, and other numerical approximations come into play. There is, however, a fundamental difference between the two sources of errors: Shortcomings in the XC functional cannot be mitigated by improvements in the numerical precision.
[64] AM05 is implemented in the main version of VASP 5.1 and its use is invoked by setting GGA=AM in the INCAR file.

Downloaded 29 Feb 2008 to 134.253.26.4. Redistribution subject to AIP license or copyright; see http://jcp.aip.org/jcp/copyright.jsp

APPENDIX B – COMMENT ON PBESOL, PHYSICAL REVIEW LETTERS 2008.

Comment on "Restoring the density-gradient expansion for exchange in solids and surfaces"
A.E. Mattsson, T.R. Mattsson, and R. Armiento, Physical Review Letters **101**, 239701 (2008).

Comment on "Restoring the Density-Gradient Expansion for Exchange in Solids and Surfaces"

A recent Letter by Perdew *et al.* [1] presents a new functional, PBEsol, intended for solid state and surface systems. It is based on a gradient expansion of the exchange energy and a final fit of the exchange-correlation (xc) energy to that of surface jellium. The former component "restoring the gradient expansion" is analyzed extensively and put forward as an explanation for the excellent results, while the latter, which is a major component of the AM05 [2,3] density functional, receives little attention. A brief comparison between AM05 and PBEsol is given in the supplementary material. The focus is on partial differences, e.g., how the AM05 exchange functional is far from reproducing the behavior of the gradient expansion, and not on the integrated behavior of these two functionals. If results for AM05 and PBEsol were decidedly different, the indirect comparison would support the importance of an exchange functional with the features suggested by Perdew *et al.* However, the most striking conclusion from a direct comparison of the two functionals is not how different they are but, instead, that AM05 and PBEsol yield identical results for a wide range of solids. Hence, there is a problem in how the Letter uses the excellent results for lattice constants of solids as a main motivation for its central thesis, since these results are not unique to PBEsol.

Ropo, Kokko, and Vitos [4] found that surface energies from PBEsol and AM05 are very similar (Fig. 2 of Ref. [4]) and that the two functionals give identical lattice constant and bulk modulus for all 19 tested magnetic and nonmagnetic 3*d*, 4*d*, and 5*d* metals. We find that identical results are not limited to transition metals but extend to all tested oxides and semiconductors (see Table I for a partial list). The level of agreement is unprecedented for two "different" density functionals, and a well-grounded explanation of this behavior is important for the future development of density functional theory. PBEsol adopting the approach of AM05 in fitting the total xc energy to jellium surface energies appear as a possible explanation, in particular, since it is this total xc sum, rather than the separate parts, that matters for applications [5]. However, Table SIV of the supplemental material presents a test for three solids that suggests that PBEsol obtains AM05-like results even before the fit is made. Should that hold generally true, an alternative explanation is that the exchange functional of PBEsol shares some fundamental similarity with that of AM05 despite the differences. The functionals may be more similar in practice than indicated by the supplemental material of Ref. [1] since they approximate different choices for the exchange energy density [6]. AM05 and PBEsol yield identical results for oxides, semiconductors, and transition metals. Until the relationship between AM05 and PBEsol is fully understood, the necessity of an exchange functional for solids that "restores the gradient expansion" remains an open question.

TABLE I. Equilibrium lattice constants a_0 (Å) and bulk moduli B_0 (GPa), obtained with AM05 [2] and PBEsol [1]. We run VASP5 identically for both functionals, using the same pseudopotentials and settings as in Ref. [3], except for a tighter interval for the points used in the Murnaghan fit. Differences between codes can result in larger differences than those between PBEsol and AM05 [3]. The accuracy of VASP5 has been shown to be comparable to that of a full potential, all electron, LAPW code.

	a_0 (Å)		B_0 (GPa)	
Solid	AM05	PBEsol	AM05	PBEsol
BN	3.61	3.61	383	384
C	3.55	3.56	449	447
Si	5.43	5.43	92.3	93.3
GaAs	5.67	5.67	66.5	68.6
LiCl	5.12	5.06	30.7	35.0
MgO	4.23	4.22	154	157
α-Al2O3	5.14	5.14	241	244
Na	4.21	4.17	7.45	7.86
Mo	3.13	3.14	284	283
Al	4.01	4.02	85.7	81.7
Cu	3.57	3.57	162	163
Pd	3.87	3.88	200	202

Sandia is a multiprogram laboratory operated by Sandia Corporation, a Lockheed Martin Company, for the United States Department of Energy National Nuclear Security Administration under Contract No. DE-AC04-94AL85000.

Ann E. Mattsson,[1] Rickard Armiento,[2] and Thomas R. Mattsson[3]
[1] Multiscale Dynamic Materials Modeling MS 1322
Sandia National Laboratories
Albuquerque, New Mexico 87185-1322, USA
[2]Physics Institute
University of Bayreuth
D -95440 Bayreuth, Germany
[3]High Energy Density Physics Theory MS 1189
Sandia National Laboratories
Albuquerque, New Mexico 87185-1189, USA

Received 7 July 2008; published 5 December 2008
DOI: 10.1103/PhysRevLett.101.239701
PACS numbers: 71.15.Mb, 31.15.E−, 71.45.Gm

[1] J. P. Perdew, A. Ruzsinszky, G. I. Csonka, O. A. Vydrov, G. E. Scuseria, L. A. Constantin, X. Zhou, and K. Burke, Phys. Rev. Lett. **100**, 136406 (2008).
[2] R. Armiento and A. E. Mattsson, Phys. Rev. B **72**, 085108 (2005); the AM05 web site: http://dft.sandia.gov/functionals/AM05.html.
[3] A. E. Mattsson, R. Armiento, J. Paier, G. Kresse, J. M. Wills, and T. R. Mattsson, J. Chem. Phys. **128**, 084714 (2008).
[4] M. Ropo, K. Kokko, and L. Vitos, Phys. Rev. B **77**, 195445 (2008).
[5] R. Armiento and A. E. Mattsson, Phys. Rev. B **68**, 245120 (2003).
[6] R. Armiento and A. E. Mattsson, Phys. Rev. B **66**, 165117 (2002).

 © 2008 The American Physical Society

APPENDIX C –WORK FUNCTIONS FROM QSGW, TO BE SUBMITTED TO PHYSICAL REVIEW B.

QSGW calculation of the work functions of Al(111) and Al(100) surfaces

Sergey V. Faleev, Oleg N. Mryasov, and Thomas R. Mattsson

To be submitted for publication in Physical Review B (2009).

QSGW calculation of the work functions of Al(111) and Al(100) surfaces

Sergey V. Faleev,[1,2,*] Oleg N. Mryasov,[1,2] and Thomas R. Mattsson[3]

[1]*MINT Center, University of Alabama,*

P.O. Box 870209, Tuscaloosa, AL 35487, USA

[2]*Physics and Astronomy, University of Alabama, Tuscaloosa, AL, 35487, USA*

[3]*HEDP Theory, MS 1189, Sandia National Laboratories, Albuquerque, NM 87185, USA*

(Dated: September 16, 2009)

Abstract

The work functions of Al(111) and Al(100) surfaces have been calculated by using the quasiparticle self-consistent GW (QSGW) approach. We found that modifications of the original QSGW method are required in order to describe systems that have extended regions with small electronic density, e.g. the metal/vacuum interface systems. Such modifications have been suggested and their accuracy has been investigated for the Al surfaces. Obtained results for work functions are not dependent on the DFT functional parameterization used to calculate starting Hamiltonian and are in excellent agreement with experiment.

PACS numbers:

*Electronic address: sfaleev@mint.ua.edu

I. INTRODUCTION

The work function is one of the most important quantities in the characterization of surfaces. An accurate theoretical prediction of the work function is important for understanding the wide range of surface phenomena such as growth rate, the form of crystallites, sintering, catalytic behavior, adsorption, chemical reactions, surface segregation, formation of grain boundaries, etc. In addition, the work function largely determines rates of electron surface emission and is therefore of applied interest for optimizing thermionic emitters [1], where a low work function is sought, and pulsed-power components, for example transmission lines, where a high work function is required.

Presently, most common way to calculate the work function is by using the local density approximation (LDA) or the generalized gradient approximation (GGA) of the density functional theory (DFT) [2, 3]. Unfortunately, the accuracy of the DFT-based methods in calculation of the work function is not always satisfactory. For example, the DFT results for work function of Al(111) surface range from 3.70 eV to 4.73 eV [4–14] while the experimental photoelectric measurement carried out in ultrahigh vacuum conditions gives the value of 4.24 eV [15]. Similarly, different DFT functionals give work function for Al(100) surface in a broad range from 3.36eV to 4.82 eV [4, 5, 13, 16–19] while the experimental value is 4.41 eV [15]. The strong dependence of the calculated value of the work function of Al (as well as other metals) on the DFT functional used suggests that beyond DFT methods are required in order to achieve accuracy of the order of 0.1 eV or better. Heinrichsmeier et al. [20] proposed a new non-local parameterization of the exchange-correlation functional based on the non-self-consistent GW calculations, the V_{xc}(GW) method. Using this method they obtained the values of the work function 4.82 eV for Al(111) and 4.59 eV for Al(100), that are 0.58 eV and 0.18 eV larger then experimental results, correspondingly. Such large error, particularly for the Al(111), could be attributed to the fact that these GW calculations were non-self-consistent; consequently, results are dependent on the initial DFT functional parameterization [20].

In the present work we calculate the work functions within the recently developed quasiparticle self-consistent GW (QSGW) approach [21–23] that does not depend on initial DFT functional parameterization. It has been shown that QSGW improves agreement with experiment (as compared to both DFT and usual perturbative non-self-consistent GW approaches)

for a number of properties calculated for different classes of materials, including alkali metals, semiconductors, wide band gap insulators, transitional metals, transition metal oxides, magnetic insulators, rare earth compounds, etc [21–25]. These results suggest that QSGW method could be successfully applied to calculate work functions of a broad range of materials and surfaces. To the best of our knowledge, so far QSGW method was not applied to the problem of work function. Thus, the aim of this paper is to study the accuracy of the QSGW method for calculation of the work functions. In this paper we report results for Al(111) and Al(100) surfaces. The work function of Al(111) and Al(100) surfaces have been a subject of many previous theoretical and experimental studies [4–20] and could serve as a benchmark for estimation of the accuracy of applied method.

II. METHOD AND COMPUTATIONAL DETAILS

QSGW is a method to determine nonlocal (but static and Hermitian) optimum one-particle Hamiltonian H^0 in a self-consistent way [21–23]. First, starting with some trial Hamiltonian H^0 (usually, the LDA Hamiltonian is used as the first-iteration H^0) we calculate the self-energy $\Sigma(\omega)$ in a GW approximation. Then we define the static self-energy in the basis of the eigenfunctions $\psi_{\mathbf{k}n}(\mathbf{r})$ of the Hamiltonian H^0 as follows [21–23]

$$\Sigma^{\mathbf{k}}_{nn'} = Re\langle\psi_{\mathbf{k}n}|[\Sigma(\varepsilon_{\mathbf{k}n}) + \Sigma(\varepsilon_{\mathbf{k}n'})]/2|\psi_{\mathbf{k}n'}\rangle \ , \tag{1}$$

where $\mathbf{k}$ is the wave vector, n is the band index, $\varepsilon_{\mathbf{k}n}$ denote eigenvalues of H^0, and Re means to take the Hermitian part. Next, we construct updated next-iteration H^0 by using this $\Sigma^{\mathbf{k}}_{nn'}$ instead of the usual LDA exchange-correlation potential

$$H^0 = -\frac{\nabla^2}{2m} + V^{ext} + V^H + \sum_{\mathbf{k}nn'} |\psi_{\mathbf{k}n}\rangle \ \Sigma^{\mathbf{k}}_{nn'} \langle\psi_{\mathbf{k}n'}| \ , \tag{2}$$

where V^{ext} is the external (nuclei) potential and V^H is the Hartree potential. This procedure is iterated until the self-consistency is achieved; the $\Sigma^{\mathbf{k}}_{nn'}$ generated by H^0 is identical (within some small tolerance) to the $\Sigma^{\mathbf{k}}_{nn'}$ that enters into H^0. It has been shown [22] that such procedure minimizes, although in an approximate way, the difference between the full non-local, non-static and non-Hermitean GW Hamiltonian $H(\omega) = -\frac{\nabla^2}{2m} + V^{ext} + V^H + \Sigma(\omega)$ and Hamiltonian H^0 (that is why it is called 'optimum'). Note that $H(\omega)$ is a functional of the

H^0 because both V^H and $\Sigma(\omega)$ calculated in the GW approximation depend on eigenfunctions generated by H^0, so described above iteration procedure self-consistently determines both $H(\omega)$ and corresponding optimum H^0.

In present work we used experimental lattice constant of Al at zero temperature, 4.025 Å [26]. The Al(111) and Al(100) surfaces have been modeled by a (1×1) surface unit cell in xy-directions and a periodic combination of N_A Al layers and N_V vacuum layers in z-direction. The vacuum layer has the same width as the Al layer with so-called floating basis orbitals [27] placed instead of the atomic muffin-tin orbitals. N_A ranged from 4 to 12 and N_V ranged from 6 to 10 have been used to analyze the convergence of the results with respect to these parameters. The work function, Φ, is defined as the difference between the electrostatic potential at a point far from the surface and the Fermi energy; $\Phi = V_{es}(\infty) - \varepsilon_F$. In our calculations $V_{es}(\infty)$ was estimated as electrostatic potential in the middle of the vacuum slab. We find that that N_V=6 is sufficient to determine the work function within the 0.005 eV accuracy. Both relaxed and unrelaxed internal atomic coordinates have been utilized to model the Al(111) surface for $N_A \geq 6$. In particular, the experimental values of 1.7% and 0.5% [28] for expansion of the first and second surface Al(111) layers have been used in relaxed case. For Al(100) only unrelaxed coordinated have been used in accordance to the experimental reports of the 0% change in Al interlayer spacing [29, 30].

We use the QSGW method, which is presently implemented as an extension of the all-electron full-potential linear muffin-tin orbital (LMTO) program suite. The diagram of the self-consistency cycle that includes the LMTO and GW parts of the code are shown on the Figure 2 of Ref. [23]. The description of the basis sets and other details of the LMTO and QSGW implementations could be found in Refs. [23] and [27].

The integration over the surface Brillouin zone (BZ) in the LMTO part of the code has been performed with (22×22) and (24×24) Monkhorst-Pack meshes [31] ($\mathbf{k}^{LMTO}$-mesh). The GW self-energy has been calculated with (6×6), (8×8), and (10×10) meshes in the surface BZ ($\mathbf{k}^{GW}$-mesh). The GW part of the code (where the self-energy is calculated given the eigenfunctions and eigenvalues of the H^0 are generated by the LMTO part) is much more computationally demanding as compared to the LMTO part of the code. In practice it is computationally prohibitive to calculate the self-energy on the same fine $\mathbf{k}^{LMTO}$-mesh that is needed for the LMTO part. Thus, rather sophisticated procedure that includes several transformations of the self-energy $\Sigma^{\mathbf{k}}_{nn'}$ between different basis sets have been developed to

interpolate the self-energy calculated by the GW part of the program on a coarse $\mathbf{k}^{GW}$-mesh to finer $\mathbf{k}^{LMTO}$-mesh used by the LMTO part of the program.[23]

Also it has been found that matrix elements of the self-energy between states with high energy often cannot be interpolated with sufficient accuracy from the $\mathbf{k}^{GW}$-mesh to the $\mathbf{k}^{LMTO}$-mesh[23]. The latter is in part due to the long range of the LMTO basis set (e.g. the smallest eigenvalue of the overlap matrix can be of the order of 10^{-10}). In order to overcome this $\mathbf{k}$-interpolation problem, the high-energy part ($\varepsilon^{LDA}_{\mathbf{k}\tilde{n}}, \varepsilon^{LDA}_{\mathbf{k}\tilde{m}} > E_{xccut}$) of the difference between the self-energy and LDA exchange-correlation potential,

$$\triangle V^{xc}_{\tilde{n}\tilde{m}} = \Sigma_{\tilde{n}\tilde{m}} - V^{xc,LDA}_{\tilde{n}\tilde{m}} \tag{3}$$

has been substituted by a diagonal matrix with diagonal matrix elements given by linear function of the LDA energy, $\triangle V^{xc}_{\tilde{n}\tilde{n}} = a + b \times \varepsilon^{LDA}_{\mathbf{k}\tilde{n}}$. Here "$\sim$" over the subscript signifies that the function is represented in the basis of eigenfunctions $\psi^{LDA}_{\mathbf{k}\tilde{n}}$ of the LDA Hamiltonian (the LDA basis) with eigenvalues $\varepsilon^{LDA}_{\mathbf{k}\tilde{n}}$. The energy cutoff parameter E_{xccut} is typically of the order of 2-3 Ry. The constants a and b are fitted from calculated $\triangle V^{xc}_{\tilde{n}\tilde{n}}$ at lower energies. The results for the calculated quasiparticle (QP) energies usually weakly dependent on the cutoff parameter E_{xccut} or constants a and b. More details on the interpolation procedure and the method used to control its accuracy for bulk calculations could be found in Ref. [23], section II, subsection G.

In the LDA basis the optimum Hamiltonian $H^0(\mathbf{k})$ (2) has form

$$H^0_{\tilde{n}\tilde{m}}(\mathbf{k}) \equiv \langle \psi^{LDA}_{\mathbf{k}\tilde{n}} | H^0 | \psi^{LDA}_{\mathbf{k}\tilde{m}} \rangle = \varepsilon^{LDA}_{\mathbf{k}\tilde{n}} \delta_{\tilde{n}\tilde{m}} + \triangle V^{xc}_{\tilde{n}\tilde{m}}(\mathbf{k}) \ . \tag{4}$$

After described above modification of the matrix $\triangle V^{xc}_{\tilde{n}\tilde{m}}$, the Hamiltonian $H^0_{\tilde{n}\tilde{m}}(\mathbf{k})$ in a form of Eq.(4) is used in LMTO part of the program to obtain the QP wave fictions (in the LDA basis) and energies.

The outlined above $\mathbf{k}$-interpolation procedure has well controllable errors in the case of bulk materials. In these work we found that the QSGW method requires additional modification if the system has extended regions with small electronic density, e.g. the metal/vacuum interface system. Specifically, we find that the interpolation errors for the matrix elements $\triangle V^{xc}_{\tilde{n}\tilde{m}}(\mathbf{k})$ between occupied states [i.e. states with energies $\varepsilon^{LDA}_{\mathbf{k}\tilde{m}} \leq \varepsilon_F$ that are spatially concentrated in the metal region] and "vacuum" states [i.e. states with energies $\varepsilon^{LDA}_{\mathbf{k}\tilde{n}} \sim \varepsilon_F + \Phi$ that are extended to the whole volume of the system] lead to

(slightly) unproper mixing of these states. (Here ε_F is the Fermi energy and Φ is the work function.) As a result, after diagonalization of the Hamiltonian (4), the QP occupied states have some small tails that unphysically slow decay as a function of distance from the metal surface into the vacuum region. These tails manifest themselves as unphysical deviations of the decay rate of the electron density deep in vacuum region from the exponential behavior.

In order to overcome this problem we suggest to use the method similar to that employed in bulk materials. Specifically, we put all non-diagonal matrix elements of $\triangle V^{xc}_{\tilde{n}\tilde{m}}(\mathbf{k})$ equal to zero if energies $\varepsilon^{LDA}_{\mathbf{k}\tilde{n}}$ and $\varepsilon^{LDA}_{\mathbf{k}\tilde{m}}$ satisfy following conditions:

$$\begin{aligned} &\triangle V^{xc}_{\tilde{n}\tilde{m}}(\mathbf{k}) = \triangle V^{xc}_{\tilde{m}\tilde{n}}(\mathbf{k}) = 0 \quad \text{if} \\ &\varepsilon^{LDA}_{\mathbf{k}\tilde{n}} - \varepsilon^{LDA}_{\mathbf{k}\tilde{m}} > E_c \quad \text{and} \quad \varepsilon^{LDA}_{\mathbf{k}\tilde{n}} > \varepsilon_F \ . \end{aligned} \tag{5}$$

Here E_c is new cutoff parameter. The idea of the method is to allow the occupied states $\tilde{m}$ to be mixed only with unoccupied states $\tilde{n}$ with energy less then $\varepsilon_F + E_c$, that will prevent them from mixing with extended vacuum states if $E_c < \Phi$ [at least in the first order of the perturbation theory, if consider $\triangle V^{xc}_{\tilde{n}\tilde{m}}(\mathbf{k})$ in Eq. (4) as a perturbation to the LDA Hamiltonian]. In the limit $E_c \to \infty$ there is no modification of the matrix $\triangle V^{xc}_{\tilde{n}\tilde{m}}(\mathbf{k})$ and the method reduces to the standard QSGW approach. In the opposite limit, $E_c \to 0$, the method becomes an "unoccupied states eigenvalue-only" self-consistent GW method when unoccupied QP wave functions are always equal to the LDA wave functions and only QP energies are modified due to the diagonal matrix elements $\triangle V^{xc}_{\tilde{n}\tilde{n}}(\mathbf{k})$. Thus, parameter $0 < E_c < \infty$ smoothly interpolates between these two methods. Note that second condition in (5) always allows the *occupied* states to be mixed between themselves.

The method of truncating the matrix elements (5) works only for limited number of the metal/vacuum interface systems. It does not work for metals whose *bulk* electronic structure is strongly affected by truncating the non-diagonal matrix elements $\triangle V^{xc}_{\tilde{m}\tilde{n}}(\mathbf{k})$ as specified by Eq. (5) with cutoff $E_c \sim \Phi$. Fortunately, for bulk Al the "unoccupied states eigenvalue-only" self-consistent GW is a good approximation to the full QSGW. This is a consequence of the fact that Al is a simple *sp* electron system and the LDA wave functions of bulk Al are already good enough; typical overlap between the LDA and QP wave functions is of the order of 99% or more.

III. RESULTS AND DISCUSSION

Figure 1 shows the density of states (DOS) of the bulk Al calculated in LDA, full QSGW (that corresponds to the limit $E_c \to \infty$), modified QSGW as specified by Eq. (5) with small cutoff parameter $E_c = 0.1$ eV, and the standard "eigenvalue-only" self-consistent GW where all non-diagonal elements of the GW addition to the LDA Hamiltonian are neglected $\triangle V^{xc}_{\tilde{n}\tilde{m}}(\mathbf{k}) = \triangle V^{xc}_{\tilde{n}\tilde{n}}(\mathbf{k})\delta_{\tilde{n}\tilde{m}}$, so the QP wave functions are always equal to the LDA ones. It can be seen that all three modifications of the GW method produce very similar DOS, different from the LDA result. The "eigenvalue-only" DOS is very close to the full QSGW DOS with some small deviations in the energy range from $\varepsilon_F - 1$ eV to $\varepsilon_F + 3$ eV. More importantly, the DOS obtained in the full QSGW (solid line) and DOS obtained by modified QSGW with small cutoff $E_c = 0.1$ eV (dotted line) are almost indistinguishable on the figure. This means that the truncation (5) of the matrix elements $\triangle V^{xc}_{\tilde{n}\tilde{m}}(\mathbf{k})$ with *arbitrary* cutoff parameter $E_c \geq 0.1$ eV practically does not change the bulk Al electronic structure.

Now we turn to the Al/vacuum interface systems. Figure 2 shows the averaged over the xy plane electron density (note the logarithmic scale) as function of the distance form the center of the vacuum slab, z, for Al(111) and Al(100) systems with five different values of the E_c parameter. The calculations have been performed for 4 Al and 8 vacuum layers ($N_A = 4$ and $N_V = 8$). We see that for both systems the density exponentially decreases away from the metal surface (as it should be) independent on the E_c parameter for $E_c \leq 4.08$ eV (three curves with $E_c = 1.36$, 2.72, and 4.08 eV are non-distinguishable on the figure). But for E_c above 4.08 eV the density begins to deviate from normal exponential behavior; the electronic density near the the center of the vacuum slab sharply increases by two orders of magnitude for $E_c = 6.8$ eV as compare to results for smaller values of $E_c \leq 4.08$ eV. For Al(111) the density calculated with $E_c = 6.8$ eV even increases, at some z, when the distance from the metal increases. We believe that such unphysical behavior of density in vacuum region at large E_c is a consequence of the $\mathbf{k}$-interpolation errors for the matrix elements $\triangle V^{xc}_{\tilde{m}\tilde{n}}(\mathbf{k})$ between occupied states with $\varepsilon^{LDA}_{\mathbf{k}\tilde{m}} \leq \varepsilon_F$ and "vacuum" states with $\varepsilon^{LDA}_{\mathbf{k}\tilde{n}} > \varepsilon_F + \Phi$.

On the other hand these errors are not large on an absolute scale; they are seen only at small values of density, 4-5 orders of magnitude smaller then the density in metal region. The calculated QP energies also are not strongly affected by these errors. The QP energy bands calculated with parameters $E_c = 2.72$ eV and 6.80 eV (not shown) almost coincide

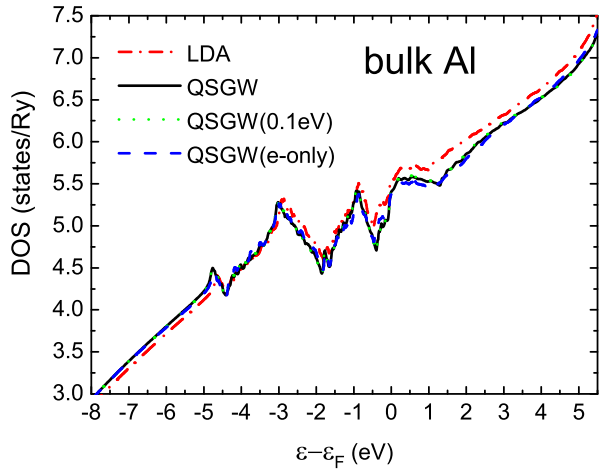

Faleev et al Fig1

FIG. 1: (Color online) Density of states (DOS) of the bulk Al calculated in LDA (dot-dashed line), full QSGW (solid line), modified QSGW with cutoff parameter $E_c = 0.1$ eV (dotted line), and the standard "eigenvalue only" self-consistent GW (dashed line). The DOS curves of the full QSGW and modified QSGW with $E_c = 0.1$ eV are non-distinguishable on the figure.

with each other for states with energies less then $\varepsilon_F + 2$ eV and begin to deviate slowly for higher energies (i.e. increasing E_c from 2.72 eV to 6.8 eV results in up-shift of the QP bands with energy above $\varepsilon_F + 4$ eV by a value ranged from 0.0 to 0.2 eV, depending on particular band). Nevertheless in order to obtain the work function with 0.1 eV accuracy or better, these errors should be eliminated by using an appropriate value of the E_c parameter.

As could be concluded from Figs. 1 and 2, there is a range of E_c parameter $0 \leq E_c \leq 4.08$ eV where the **k**-interpolation errors could be neglected for Al interfaces while the bulk Al electronic structure still coincide with the full QSGW electronic structure. Such fortunate

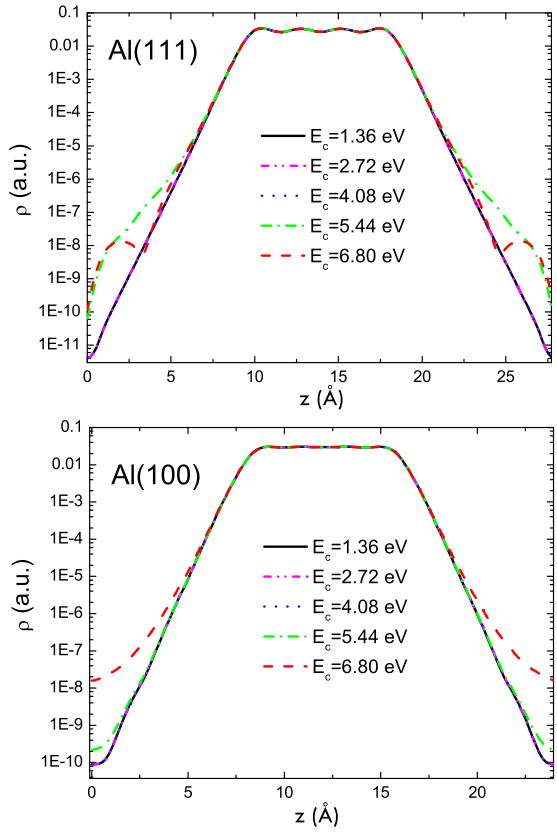

Faleev et al Fig 2

FIG. 2: (Color online) The averaged over the xy plane electron density (in atomic units, note logarithmic scale) as function of the distance form the center of the vacuum slab, z, (in Å) for Al(111)/vacuum (top panel) and Al(100)/vacuum (bottom panel) interfaces calculated by modified QSGW method with five different values of the E_c parameter. The number of Al and vacuum layers are $N_A = 4$ and $N_V = 8$. For both, Al(111) and Al(100) interfaces the density curves with three smallest values of E_c are non-distinguishable on the figure.

situation is not universal. For example, we checked that for Fe/vacuum or Cu/vacuum interfaces there is no such range of E_c parameter; for these metals E_c should be above 1 Ry in order for the electronic structure of bulk metal to be close to that of the full QSGW, while the interpolation errors for the metal/vacuum system with such $E_c \geq 1$ Ry are non-negligible. The difference with Al is that for Fe and Cu the LDA wave functions are not a good approximation to the QSGW wave functions. The development of an universal method

based on the QSGW scheme that could be applied to calculation of the work function of *all* metals will be a subject of future study.

Figure 3 shows the work function, Φ, calculated for Al(111) and Al(100) surfaces with $N_A = 4$ and $N_V = 8$ as function of the cutoff parameter E_c. It is seen that the calculated work function is independent of E_c up to $E_c \sim 4$ eV for Al(111) and $E_c \sim 5$ eV for Al(100) and changes rapidly after these thresholds. The work function dependence on E_c shown on Figure 3 agrees well with what we would expect; the calculated work function starts to change from a flat line due to increasing role of the $\mathbf{k}$-interpolation errors as E_c approaches Φ, approximately 4.2 eV for Al(111) and somewhat larger for Al(100). The independence of calculated work function from E_c (for $E_c < 4$ eV) provides additional evidence that the method (5) is suitable to describe the Al/vacuum interfaces. In all calculations presented below the E_c parameter is fixed and equals to $E_c = 2.72$ eV.

Figure 4 shows the variation of the Φ as function of the number of Al layers, $N_A \leq 12$, for Al(111) (top panel) and Al(100) (bottom panel) surfaces, calculated with LDA and QSGW with following parameters: $E_c = 2.72$ eV, $N_V = 6$, (22×22) $\mathbf{k}^{LMTO}$-mesh, and (6×6) $\mathbf{k}^{GW}$-mesh in the surface BZ. For the LDA calculations the Barth-Hedin [32] DFT functional has been used. We see that Φ oscillates when the film thickness increases. These oscillations are well known [4] and could be attributed to the quantum-size effects (QSE). The positions of the local maximums of the LDA Φ at $N_A = 5$, 8, and 11 for the Al(111) surface and the minimum at $N_A = 7$ for the Al(100) surface agree well with previous DFT calculations [4]. The QSGW work function also shows the QSE oscillations, similar to that of the LDA. We estimate the uncertainty in our calculated at $N_A = 12$ values of the work function due to the QSE as ± 0.02 eV, that is larger then uncertainties due to other parameters of the method (i.e. uncertainty related to the number of $\mathbf{k}$ points in the $\mathbf{k}^{GW}$-mesh).

The results of our calculations as well as results of many previous studies are shown in Table I in comparison to the experimental data. It is seen that the fluctuations of calculated values for the DFT work functions could reach 1 eV or more. The work functions calculated by GGA method are about 0.2 eV smaller then average value of the LDA work functions. As we noted in introduction, the large range of calculated values for the DFT work functions suggests that beyond DFT method is required that does not depend on the choice of the DFT functional.

Our values of the QSGW work functions are 4.17 eV for Al(111) relaxed surface, 4.19 eV

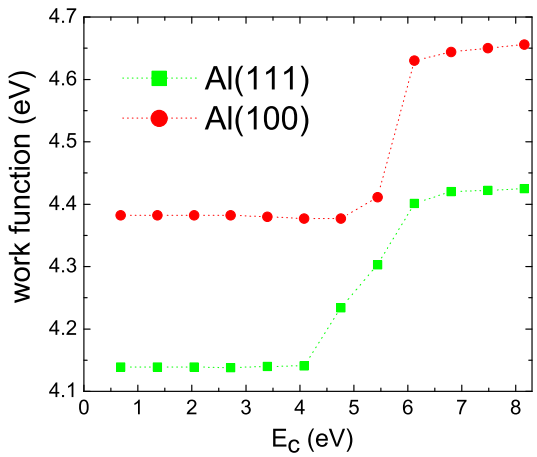

Faleev et al Fig 3

FIG. 3: (Color online) The work function calculated for Al(111) and Al(100) surfaces with $N_A = 4$ and $N_V = 8$ as function of the cutoff parameter E_c.

for Al(111) unrelaxed surface and 4.36 eV for Al(100) unrelaxed surface. We checked that these values do not depend on the LDA functional used for the first-iteration H^0 Hamiltonian and also for the LDA basis that define the QP Hamiltonian H^0 (4). Specifically, we employed the Barth-Hedin [32] and Ceperley-Alder [33] LDA functionals and obtained identical QSGW results. The small effect of the surface relaxation on the Al(111) work function (reduction by 0.02 eV relative to unrelaxed case) is similar to results of previous works (see, e.g. Ref. 4). Our LDA work functions obtained with the Ceperley-Alder parameterization are 0.10 eV smaller compare to that of the Barth-Hedin LDA parameterization.

Table I shows that our QSGW work functions differ by 0.07 eV and 0.05 eV from the experimental photoelectric measurements carried out in ultrahigh vacuum conditions [15]

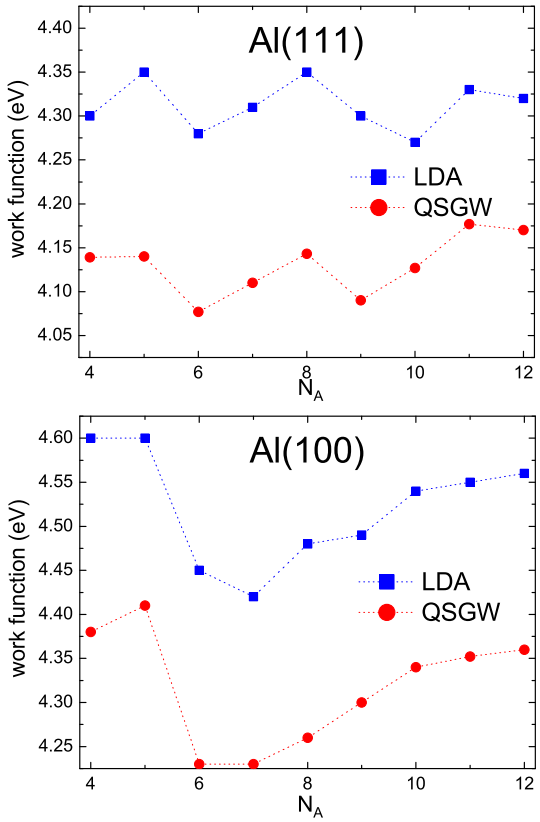

Faleev et al Fig 4

FIG. 4: (Color online) The work function of Al(111) (top panel) and Al(100) (bottom panel) surfaces calculated with LDA (squares) and QSGW (circles) as function of number of the Al layers, N_A.

for Al(111) and Al(100), correspondingly. This is an excellent agreement; both differences are less then 0.1 eV and of the order of the sum of theoretical and experimental error bars. Moreover, the difference between QSGW fork functions $\Phi(100) - \Phi(111) = 0.19$ eV is in excellent agreement with the experimental data [15] $\Phi(100) - \Phi(111) = 0.17$ eV. An earlier experiment [34] reports 0.21 eV smaller value for Al(100) work function compare to that of Ref. [15]. Grepstad et al.[15] suggested that this discrepancy could be due to higher impurity concentration, in particular oxygen, in earlier experiment.

TABLE I: A comparison of the QSGW Al work functions (given in eV) with previous calculations and experimental result

	Al(111)		Al(100)	
QSGW	4.17[a]		4.36[a]	
V_{xc}(GW)	4.82[20]		4.59[20]	
GGA	4.06[4]	4.06[5]	4.24[4]	4.25[5]
GGA			4.27[16]	
LDA	4.32[b]	4.22[c]	4.56[b]	4.46[c]
LDA	4.23[5]	4.73[6]	4.42[5]	4.42[17]
LDA	3.70[7]	4.59[8]	3.36[17]	4.48[17]
LDA	4.09[9]	4.31[10]	4.44[17]	4.39[17]
LDA	4.54[11]	4.32[12]	4.82[17]	4.53[18]
LDA	4.49[13]	4.7[14]	4.50[13]	4.51[19]
Exp.	4.24± 0.02[15]		4.41± 0.03[15]	
Exp.	4.26± 0.03[34]		4.20± 0.03[34]	

[a]Present work, QSGW

[b]Present work, Barth-Hedin LDA functional

[c]Present work, Ceperley-Alder LDA functional

IV. SUMMARY

We applied QSGW method to calculate the work functions of Al(111) and Al(100) surfaces. Obtained results are in excellent agreement with the experiment with errors of 0.07 eV and 0.05 eV for (111) and (100) surfaces correspondingly. Calculated values of the work functions do not depend on the DFT functional used for the initial Hamiltonian H^0. The results suggest that QSGW method could be used for reliable and accurate calculation of the work functions with accuracy of the order of 0.1 eV or better.

We found that modification of the original QSGW method [21–23] is required in order to apply the method to the metal/vacuum surface. In particular, special care should be taken to control the errors originated form **k**-interpolation of the self-energy matrix that, if unchecked, could result in unproper mixing of the occupied and unoccupied states. In some

simple cases, such as Al, where LDA wave functions are already a good approximation to the QP wave functions, simple truncation of corresponding matrix elements [see Eq. (4)] could be enough to control these errors. For more difficult cases, where QP and LDA wave functions are significantly different, another method to control the **k**-interpolation errors should be developed. Thus, additional research is needed for development of an *universal* method for calculation of the work function and other surface-related properties of materials within QSGW method.

V. ACKNOWLEDGEMENT

We thank Mark van Schilfgaarde for helpful discussions. This work was supported by the Science of Extreme Environments LDRD Investment Area at Sandia National Laboratories. Sandia is a multiprogram laboratory operated by Sandia Corporation, a Lockheed Martin Company, for the United States Department of Energy under contract DE-AC04-94-AL85000. O.M. and S.F. acknowledge the CNMS User support by Oak Ridge National Laboratory Division of Scientific User facilities, Office of Basic Energy Sciences, U.S. Department of Energy.

---

[1] D. R. Jennison, P. A. Schultz, D. B. King, and K. R. Zavadil, Surface Science **549**, 115 (2004).

[2] P. Hohenberg and W. Kohn, Phys. Rev. **136**, B864 (1964).

[3] W. Kohn and L. J. Sham, Phys. Rev. **140**, A1133 (1965).

[4] J. L. F. Da Silva, Phys. Rev. B **71**, 195416 (2005).

[5] C. J. Fall, N. Binggeli, and A. Baldereschi, Phys. Rev. Lett. **88**, 156802 (2002).

[6] D.-S. Wang, A. J. Freeman, H. Krakauer, and M. Posternak, Phys. Rev. B **23**, 1685 (1981).

[7] I. P. Batra, S. Ciraci, G. P. Srivastava, J. S. Nelson, and C. Y. Fong, Phys. Rev B **34**, 8246 (1986).

[8] J. C. Boettger, Phys. Rev B **53**, 13133 (1996).

[9] A. Kiejna and B. I. Lundqvist, Phys. Rev. B **23**, 1685 (2001).

[10] P. J. Feibelman and D. R. Hamann, Phys. Rev. B **29**, 6463 (1984).

[11] H. L. Skriver and N. M Rosengaard, Phys. Rev B **46**, 7157 (1992).

[12] K. M. Ho and K. P. Bohen, Phys. Rev B **32**, 3446 (1985).

[13] W. Hummel and H. Bross, Phys. Rev. B **58**, 1620 (1998)

[14] H. Krakauer, M. Posternak, A. J. Freeman, and D. D. Koelling, Phys. Rev. B **23**, 3859 (1981).

[15] J. K. Grepstad, P. O. Garland, and B. J. Slagsvold, Surf. Sci. **57**, 348 (1976).

[16] S. J. Sferco, P. Blaha, and K. Schwarz, Phys. Rev. B **76**, 075428 (2007).

[17] G. A. Benesh and D. Gebreselasie, Phys. Rev. B **54**, 5940 (1996).

[18] E. Wimmer, M. Weinert, A. J. Freeman, and H. Krakauer, Phys. Rev. B **24**, 2292 (1981)

[19] K.-P. Bohnen and K.-M. Ho, Surf, Sci. **207**, 105 (1988).

[20] M. Heinrichsmeier, A. Fleszar, W. Hanke, and A. G. Ehuiluz, Phys. Rev. B **57**, 14974 (1998)

[21] S. V. Faleev, M. van Schilfgaarde, and T. Kotani, Phys. Rev. Lett. **93**, 126406 (2004).

[22] M. van Schilfgaarde, T. Kotani, and S. V. Faleev, Phys. Rev. Lett. **96**, 226402 (2006).

[23] T. Kotani, M. van Schilfgaarde, and S. V. Faleev, Phys. Rev. B **76**, 165106 (2007).

[24] M. Shishkin, M. Marsman, and G. Kresse, Phys. Rev. Lett. **99**, 246403 (2007).

[25] F. Bruneval, N. Vast, L. Reining, M. Izquierdo, F. Sirotti, and N. Barrett, Phys. Rev. Lett. **97**, 267601 (2006).

[26] R. W. G. Wyckoff, *Crystal Structures*, 2nd ed. (Interscience, New York, 1963).

[27] M. van Schilfgaarde, T. Kotani, and S. V. Faleev, Phys. Rev. B **74**, 245125 (2006).

[28] J. R. Noonan and H. L. Davis, J. Vac. Sci. Technol. A **8**, 2671 (1990).

[29] D. W. Jespen, P. M. Marcus, and F. Jona, Phys. Rev. B **5**, 3933 (1972).

[30] F. Jona, D. Sondericker, and P. M. Marcus, J. Phys. C **13** L155 (1980).

[31] H. J. Monkhorst and J. D. Pack, Phys. Rev. B **13**, 5188 (1976).

[32] U. Von Barth and L. Hedin, J. Phys. C **5**, 1629 (1972)

[33] D. M. Ceperley and B. J. Alder, Phys. Rev. Lett. **45**, 566 (1980)

[34] R. M. Eastment and C. H. B. Mee, J. Phys. F: Met. Phys. **3**, 1738 (1973)

Distribution list:

09536 Technical Library 0899 (electronic copy)

Sandia National Laboratories